DEUTSCHES ELEKTRONEN-SYNCHROTRON
in der HELMHOLTZ-GEMEINSCHAFT

DESY-THESIS-2002-046
December 2002

Bulk and Surface Electronic Structure of Gallium Nitride and Zinc Selenide

by

L. Plucinski

ISSN 1435-8085

NOTKESTRASSE 85 - 22607 HAMBURG

Bulk and Surface Electronic Structure of Gallium Nitride and Zinc Selenide

Dissertation
zur Erlangung des Doktorgrades
des Fachbereichs Physik
der Universität Hamburg

vorgelegt von

Lukasz Plucinski

aus Warschau

Hamburg 2002

Gutachter der Dissertation:	Prof. Dr. R. L. Johnson
	Prof. Dr. H. Heyszenau
Gutachter der Disputation:	Prof. Dr. R. L. Johnson
	Prof. Dr. B. Sonntag
Datum der Disputation:	8.11.2002
Vorsitzender des Prüfungsausschusses:	Dr. D. Rüter
Vorsitzender des Promotionsausschusses und Dekan des Fachbereichs Physik:	Prof. Dr. F.-W. Büßer

Kurzfassung

In dieser Arbeit wurden experimentelle und theoretische Untersuchungen der elektronischen Oberflächen- und Substratstruktur an zwei bedeutenden Klassen von Halbleitern durchgeführt: Es wurde die III-V Verbindung GaN mit einer hexagonalen Wurtzitstruktur und die II-VI Verbindung ZnSe, welche in Zinkblendestruktur vorliegt, untersucht. Diese Materialien sind aktuell von großem Interesse, da ihre optischen Bandlücken im blau-grünen Spektralbereich liegen und ihre Oberflächeneigenschaften sind von großer Bedeutung für das Design licht-emittierender photonischer Elemente.

Als experimentelle Technik wurde hauptsächlich winkelaufgelöste Photoemission unter Verwendung von Synchrotronstrahlung verwendet. Die Messungen wurden am Hamburger Synchrotronstrahlungslabor (HASYLAB) am Deutschen Elektronen-Synchrotron (DESY) in Hamburg durchgeführt. Die theoretischen Untersuchungen wurden mit Hilfe von *ab initio* Dichtefunktionaltheorie (*density functional theory*) Berechnungen im Rahmen der lokale Dichte (*local density*) oder verallgemeinerter Gradient (*generalized-gradient*) Näherung für die Austausch-Korrelations Funktionale durchgeführt.

Für den Transport der Proben von der Probenwachstumsanlage in Würzburg zum Experiment in Hamburg wurde eine Transferkammer entwickelt. Winkelaufgelöste Photoelektronen Spektroskopie wurde intensiv zur Abbildung der Bandstruktur eingesetzt. Unter Annahme des einfachen freier Elektronen-Endzustand Modelles wurden mehrere Richtungen der Substrat Brillouinzone hoher Symmetrie auf die gleiche Oberflächenorientierung abgebildet. Neben der Abbildung der elektronische Bandstruktur von Oberflächen mit Standardtechniken wurde zusätzlich die chemische Zusammensetzung der Oberflächen mit winkelintegrierter Rumpfelektronen Photoemission bestimmt.

Die theoretischen Untersuchungen dienten nicht nur zur Verifizierung der Photoemissionsmessungen – sie bildeten vielmehr die Planungsgrundlage für die durchgeführten Experimente, indem versucht wurde, die zu messenden Strukturen vorherzusagen. Es wurde die detailierte elektronische Struktur der ZnSe(001)-c(2×2) Oberflächenrekonstruktion berechnet, welche die stabilste Rekonstruktion der ZnSe(001)-Oberfläche darstellt. Die durchgeführten Berechnungen stimmen gut mit den Messungen überein und sagen vorher, daß alle Oberflächenstrukturen innerhalb der obersten zwei Lagen der Rekonstruktion liegen.

Es wurden GaN-Proben zweier Orientierungen untersucht: Dünne Filme mit (0001)- und Einkristalle mit $(000\bar{1})$-Orientierung. Die Übereinstimmung zwischen Theorie und Experiment ist gut bezüglich der Substrateigenschaften, aber nicht alle Oberflächenstrukturen werden durch die Berechnungen erklärt. Als Erklärungsansatz wird vorgeschlagen, daß die GaN-Oberfläche aus kleinen Domänen verschiedener Rekonstruktionen besteht.

Abstract

Experimental and theoretical investigations of the surface and bulk electronic structure of two important classes of semiconductors are reported: the III-V compound GaN with a hexagonal *wurtzite* crystal lattice and II-VI compound ZnSe with the *zinc-blende* crystal lattice. These materials are of current interest because their fundamental optical gaps lie in the blue-green spectral region and their surface properties are of great importance in light-emitting photonic devices.

The main experimental technique used was angle-resolved photoemission with synchrotron radiation performed at the Hamburger Synchrotronstrahlungslabor (HASYLAB) at the Deutsches Elektronen-Synchrotron (DESY) in Hamburg. The theoretical calculations used *ab initio* density-functional theory with the local-density, or generalized-gradient approximations, for the exchange-correlation functional.

An experimental system for transferring samples directly from the growth chamber in Würzburg to the experiment in Hamburg was developed. Extended use of angle-resolved photoelectron spectroscopy as a band-mapping technique was applied. By assuming the simple free-electron final state model several high-symmetry directions of the bulk Brillouin zone were mapped on the same surface orientation. The electronic band structures of surfaces were mapped using standard techniques, and in addition the chemical composition of the surfaces were determined using angle-integrated core-level photoemission.

The theoretical work served not only as a verification of the photoemission measurements, but was rather a driving force for planning the experiments by predicting the features to be measured. The surface electronic structure was calculated in detail for the ZnSe(001)-c(2×2) which is the most stable reconstruction on the ZnSe(001) face. The calculations give very good agreement with the measurements and the theory predicts that all the surface features to lie within the two uppermost layers of the reconstructed surface.

Two differently oriented types of GaN samples were investigated: thin films with (0001) and single crystals with $(000\bar{1})$ orientations. There is a good agreement in case of a bulk specimen but not all the surface features are explained by the theoretical calculations. As an explanation it is proposed that the surfaces of GaN contain small domains with different reconstructions.

Table of Contents

Chapter 1

Introduction

The electronic structure of semiconductor surfaces and interfaces plays a crucial role in modern technology. Gallium nitride (GaN) and zinc selenide (ZnSe) are important materials for manufacturing solid-state light-emitting devices in the blue-green spectral region. While commercially available devices already exist (based mainly on GaN), many of the physical properties of GaN and ZnSe are not well understood.

GaN is one of the most extensively studied semiconductors over the last decade. Its wide band gap of 3.4 eV and material properties predestinates it for producing long-lifetime laser diodes and light emitting devices [1] with the main technological challenge being the production of devices with a low number of defects and impurities. The high pressure growth technique [2] allows to grow bulk crystals of GaN from a solution of nitrogen in liquid gallium, however, the so grown crystals suffer from a high level of oxygen impurities ($\approx 10^{19}/cm^3$) and Ga vacancies ($\approx 10^{18}/cm^3$) which make them very good conductors even when undoped. The thin film samples are produced by vapor-phase techniques or molecular beam epitaxy (MBE) under ultra-high vacuum (UHV) and the main problem here is to match the lattice constant of the substrate to the GaN.

The typical application of ZnSe in the past was use in infra-red and laser optics and in fact the first blue-green solid-state laser diodes were based on ZnSe [3, 4]. Recently there has been a revival of II-VI compounds due to the technological progress in preparing (001) surfaces by MBE and the characterization of their surface constitution is of fundamental interest since some studies revealed that different alloys of II-IV compounds may become an alternative to GaN based devices [5].

Photoelectron spectroscopy is the main tool for investigations of the electronic structure of semiconductor surfaces [6]. The advantage of photoemission experiment is that one sees a fraction of the photoelectrons escaping without any scattering. In this thesis GaN and ZnSe were studied mainly by means of *angle-resolved* photoelectron spectroscopy. This technique allows direct determination of the energy and momentum of electrons in solids, thus energy versus momentum dispersions can be determined.

Density functional theory (DFT) allows the electronic properties of semiconductors and their surfaces to be predicted. In this thesis theoretical results for ZnSe(001)-c(2×2) are presented and compared to the angle-resolved photoelectron spectroscopy measurements.

The thesis is organized as follows:

- The theoretical background concerning density functional theory and angle-resolved photoemission is given in Chapter 2.
- Experimental techniques and the experimental setup are explained in Chapter 3.
- Chapters 4 and 5 are dedicated to the results on GaN and ZnSe respectively.

Chapter 2

Theoretical basis

In this work we deal with bulk semiconductors and their surfaces. GaN has a wurtzite and ZnSe a zinc-blende crystal structure. In both cases differences between bulk and surface properties are observed. In this chapter the theoretical aspects of electronic structure in solids and the photoemission process is presented.

2.1 Valence band electronic structure

Information about the electronic structure is crucial for the interpretation of photoelectron spectroscopy measurements. Any problem concerning the electronic structure of matter can in principle be solved using Schrödinger's time-dependent equation. In most cases, however, we may focus on the time-independent Schrödinger's equation

$$H_{tot}\Psi(\mathbf{X},\mathbf{x}) = E\Psi(\mathbf{X},\mathbf{x}), \tag{2.1}$$

where $H_{tot} = T_e + T_L + V_{int}$ is the total Hamiltonian which represents the kinetic energy of the electrons T_e and nuclei T_L as well as Coulomb and spin electron-electron and electron-nucleus interactions V_{int}; $\mathbf{X}$ and $\mathbf{x}$ are spin-space coordinates of the nuclei and electrons respectively. Because it is a many-body problem it is not possible to solve this problem exactly.

Historical remarks

In this remarks I follow the survey articles on electron theory of solids in *Solid State Physics* and *Reviews of Modern Physics*, especially by Reitz [7], Ziman [8], Dimmock [9], and Payne *et al.* [10].

The origin of approximate methods for handling many electron problems lies in the early attempts to set up self-consistent fields for atomic systems, particularly in the work of Hartree which followed soon after the introduction of wave mechanics [11]. Slater [12] and Fock [13] independently showed that the Hartree equations could be derived by means of the variational principle. They were able to go further, however; using the determinantal form of wave function introduced by Slater [14] they derived a better set of one-electron equations, namely, the Fock equations. The theory of the covalent bonds, developed by Heitler and London in 1927 [15] showed that a one-electron formulation in which each electron is localized on one of the atoms is capable of predicting the correct order of magnitude for molecular binding energies.

The following year saw the development of the molecular orbital schemes of Hund [16] and Mulliken [17], and, finally, the Bloch theorem [18]. Bloch showed that symmetry of the crystal problem is such that the space part of the crystal orbital may be written as

$$\psi_{nk}(r) = e^{ikr} u_{nk}(r), \tag{2.2}$$

where $u_{nk}(r)$ is a function with the translational periodicity of the lattice; thus the solution in one unit cell of the crystal specifies the complete orbital. Bloch also gave a prescription for setting up the detailed form of the crystal orbital; the method is known as either linear combination of atomic orbitals (LCAO) or the tight binding method.

Perhaps the most interesting feature of the Bloch scheme is that not all electron energies are allowed in the crystal, but rather the energy regions are separated in bands. The band picture was developed and extended by many investigators during the period 1928 - 1932. In 1933 Wigner and Seitz [19, 20] showed how quantitative solutions of the Bloch type could be obtained for the alkali metals. Their method was based on a division of the crystal lattice into space-filling polyhedra, or cells, each of which containing and being centered on one atom in the metal. Improvements in the cellular method were made by Slater [21] and Bardeen [22]. The cellular method has been continually improved, and, today, provides the best developed technique for computing wave functions in metals. One of the principal assumptions of the cellular method is that the potential is nearly spherically symmetric in each unit cell, a condition which, unfortunately is not met in many solids.

An entirely different approach to the problem was provided by the orthogonal plane wave (OPW) method developed by Herring [23, 24] in 1940 in which plane waves orthogonal to all of the ion-core functions are used. By definition, any expansion in terms of these waves will always converge to a valence level. The most severe limitation of the conventional OPW method is faced with materials where the states in the valence band have the same 'angular momentum' symmetries as the core functions to which they are orthogonal.

Another procedure is Slater's augmented plane-wave method (APW) [25] in which a plane wave outside a spherical cell is joined smoothly to atomic-like wavefunctions inside the cell; these augmented waves then form a set for expansion of the wave function. The APW method was developed in order to circumvent several difficulties inherent in the earlier cellular method.

In the method of Korringa [26] Kohn and Rostoker [27] one employs the method of Green's functions in a variation-iteration scheme. The potential is adjusted to zero in the regions between spheres, and the solution within the spheres is expanded in terms of radial wave functions and spherical harmonics. Again, the radial wave functions are chosen so that they satisfy the radial wave equation for a given energy. So far the procedure is identical to the APW method. At this point, however, in the APW method the coefficients in the expansion within the spheres are determined by the requirement that the wave function matches a plane wave function on the surface of the spheres. The solution of the entire problem is then expanded in terms of these augmented plane waves [9].

Throughout this period people were trying to replace the wave function by an electron probability density. As the result of these efforts a new very powerful method of handling many electron systems was developed; density functional theory.

2.1.1 Density functional theory

There have been a number of excellent treatments of the density functional theory e.g. [10, 28–32]. In describing the main points of the DFT I will mainly follow that of Koch and Holthausen [28].

Early beginning

As already mentioned Slater and Fock independently showed that the Hartree equations could be derived using the variational princinple [12, 13]. Using the determinantal form of wave function Φ_{SD} (in short hand-notation, where only the diagonal elements are given) [28]

$$\Phi_{SD} = \frac{1}{\sqrt{N!}} \det |\chi_1(\mathbf{x}_1)\, \chi_2(\mathbf{x}_2) \ldots \chi_3(\mathbf{x}_3)|, \qquad (2.3)$$

where $\chi_i(\mathbf{x}_i)$ are *spin-orbitals* introduced by Slater [14], they derived a better set of one-electron equations, known as the Hartree-Fock equations

$$\hat{f}\chi_i = \varepsilon_i \chi_i \qquad i = 1, 2, \ldots, N, \qquad (2.4)$$

where ε_i have a physical interpretation as the orbital energies. The *Fock operator* $\hat{f}$ is defined as

$$\hat{f} = -\frac{1}{2}\nabla_i^2 - \sum_A^M \frac{Z_A}{r_{iA}} + V_{HF}(i), \qquad (2.5)$$

where M is the number of nuclei,

$$V_{HF}(\mathbf{x}_i) = \sum_j^N [\hat{J}_j(\mathbf{x}_i) - \hat{K}_j(\mathbf{x}_i)] \qquad (2.6)$$

is the Hartee-Fock potential and

$$\hat{J}_j(\mathbf{x}_1) = \int |\chi_j(\mathbf{x}_2)|^2 \, \frac{1}{r_{12}} \, d\mathbf{x}_2 \qquad (2.7)$$

is the Coulomb operator which represents the potential that an electron at position $\mathbf{x}_1$ experiences due to the average charge distribution of another electron in spin-orbital state χ_j. The second term in (2.6) is the exchange contribution to the Hartree-Fock potential, it has no physical meaning and can only be defined through its effect when operating on a spin-orbital

$$\hat{K}_j(\mathbf{x}_1)\chi_i(\mathbf{x}_1) = \int \chi_j^*(\mathbf{x}_2) \, \frac{1}{r_{12}} \, \chi_i(\mathbf{x}_2) \, d\mathbf{x}_2 \, \chi_j(\mathbf{x}_1). \qquad (2.8)$$

The Slater determinant is the exact wave function of N non-interacting particles moving in the field of effective potential V_{HF}. Because the Fock operator $\hat{f}$ depends through the Hartree-Fock potential on the spinorbitals, i.e. on the very solutions of the eigenvalue problem that needs to be solved, we have a pseudo-eigenvalue problem that needs to be worked out iteratively. The technique is called a *self-consistent field* (SCF) procedure since the orbitals are derived from their own effective potential.

Hohenberg-Kohn approach

The wave function Ψ itself is not observable. According to the Born interpretation a physical interpretation can only be associated with the square of the wave function in that $|\Psi(\mathbf{x}_1, \mathbf{x}_2, ..., \mathbf{x}_N)|^2 \, d\mathbf{x}_1 d\mathbf{x}_2 ... \, d\mathbf{x}_N$ represents the probability that electrons $1, 2, \ldots, N$ are found simultaneously in volume elements, so

$$\rho(\mathbf{r}_1) = N \int \ldots \int |\Psi(\mathbf{x}_1, \mathbf{x}_2, \ldots, \mathbf{x}_N)|^2 \, ds_1 d\mathbf{x}_2 \ldots \mathbf{x}_N \tag{2.9}$$

is the probability density of finding any of the N electrons within the volume element $d\mathbf{r}_1$ but with arbitrary spin[1] while the other $N-1$ electrons have arbitrary positions and spin in the state represented by Ψ. The quantity $\rho(\mathbf{r})$, called the electron density, is a function of three coordinates and is observable, while Ψ is a function of $4N$ coordinates and is not observable.

The first attempt to use electron density rather than the wave function for obtaining information about atomic and molecular systems are almost as old as quantum mechanics itself and date back to the early work of Thomas [33] and Fermi [34]. In their approach they take into account only the kinetic energy in terms of a fictitious model system of constant electron density, while treating the nuclear-electron and electron-electron contributions in a completely classical way. In the present context, their approach is of only historical interest.

Density functional theory was born in 1964 when a landmark paper by Hohenberg and Kohn [35] appeared in the Physical Review. The theorems in this report represent the major theoretical pillars on which all contemporary density functional theory is erected. The first theorem states, that: 'The external potential $V_{ext}(\mathbf{r})$ is (to within a constant) a unique functional of $\rho(\mathbf{r})$ since, in turn $V_{ext}(\mathbf{r})$ fixes $\hat{H}$ we see that the full many-particle ground state is a unique functional of $\rho(\mathbf{r})$'. Pictorially

$$\rho_0 \Rightarrow \{N, Z_A, R_A\} \Rightarrow \hat{H} \Rightarrow \Psi_0 \Rightarrow E_0. \tag{2.10}$$

The second Hohenberg-Kohn theorem provides the energy variational principle. It reads that for a trial density $\tilde{\rho}(\mathbf{r})$ such that $\tilde{\rho}(\mathbf{r}) \geq 0$ and $\int \tilde{\rho}(\mathbf{r}) d(\mathbf{r}) = N$ the ground state energy equals

$$E_0 \leq E[\tilde{\rho}] = T[\tilde{\rho}] + N_{Ne}[\tilde{\rho}] + E_{ee}[\tilde{\rho}]. \tag{2.11}$$

---

[1] The integral in (2.9) runs over the spin coordinates of all electrons and over all but one of the spatial variables.

Any trial density $\tilde{\rho}(\mathbf{r})$ defines its own Hamiltonian $\hat{H}$ and hence its own wave function $\tilde{\Psi}$. This wave function can now be taken as the trial wave function for the Hamiltonian generated from the true external potential V_{ext}. Thus we arrive at

$$\langle\tilde{\Psi}|\hat{H}|\tilde{\Psi}\rangle = T[\tilde{\rho}] + V_{ee}[\tilde{\rho}] + \int \tilde{\rho}(\mathbf{r})\, V_{ext}\, d\mathbf{r} = E[\tilde{\rho}] \geq E_0[\rho_0] = \langle\Psi_0|\hat{H}|\Psi_0\rangle. \quad (2.12)$$

It should be noted that the difference between the expectation value and the true ground state energy of any given Hamiltonian is due to the lack of completeness in the basis set.

Hohenberg theorems tell us that a unique mapping between the ground state density $\rho_0(\mathbf{r})$ and the ground state energy E_0 exists in principle. However, they do not provide any guidance at all on how the functionals that deliver the ground state energy should be constructed. The *Levy constrained-search* scheme [28, 36, 37], even though being very elegant in appearance and strong in formal power, is only of theoretical value and offers no solutions to practical considerations.

An avenue for how the Hohenberg-Kohn theorems can be applied in practice was suggested by Kohn-Sham in 1965 [38].

Kohn-Sham approach

The Slater determinant Ψ_{SD} can be looked upon as the exact wave function of a fictitious system of N non-interacting electrons ('uncharged fermions') moving in the effective potential V_{HF}. In such a case it will be possible to set up a non-interacting reference system, with a Hamiltonian in which an effective, local potential $V_S(\mathbf{r})$ was introduced

$$\hat{H}_S = -\frac{1}{2}\sum_i^N \nabla_i^2 + \sum_i^N V_S(\mathbf{r}_i). \quad (2.13)$$

Its ground state wave function is represented by a Slater determinant whose spin-orbitals φ are determined by the Kohn-Sham equation

$$\hat{f}^{KS}\varphi_i = \varepsilon_i\varphi_i, \quad (2.14)$$

where the one electron Kohn-Sham operator $\hat{f}^{KS}$ is defined by

$$\hat{f}^{KS} = -\frac{1}{2}\nabla^2 + V_S(\mathbf{r}), \quad (2.15)$$

where $V_S(\mathbf{r})$ represents an effective potential such that the density resulting from the summation of the moduli of the squared orbitals $\{\varphi_i\}$ exactly equals the ground state density of our real target system of interacting electrons

$$\rho_S(\mathbf{r}) = \sum_i^N \sum_S |\varphi_i(\mathbf{r}, s)|^2 = \rho_0(\mathbf{r}). \tag{2.16}$$

By choosing the effective potential $V_S(\mathbf{r})$ we connect an artificial system to the one we are interested in

$$V_S(\mathbf{r}_1) \equiv V_{eff}(\mathbf{r}_1) = \int \frac{\rho(\mathbf{r}_2)}{r_{12}} d\mathbf{r}_2 + V_{XC}(\mathbf{r}_1) - \sum_A^M \frac{Z_A}{r_{1A}}. \tag{2.17}$$

The only unknown term is the V_{XC} which includes the non-classical portion of the electron-electron interaction along with the correction for the self-interaction and the component of the kinetic energy not covered by the non-interacting reference system. The energy which represents V_{XC} is known as the *exchange-correlation* energy E_{XC}.

The quest for $E_{XC}(\rho)$

The quest for $E_{XC}(\rho)$ is based on the adiabatic connection, which provides the link between the non-classical potential energy of the exchange and correlation and the E_{XC} functional of the Kohn-Sham scheme, with special emphasis on the corresponding *hole* function [39–43]. The concept of the local density approximation which represents the bedrock of almost all current functionals is based on the uniform electron gas. More sophisticated generalized gradient approximation (GGA) and the nowadays popular hybrid functionals are developed mainly for applications in quantum chemistry. All searching for better functionals relies largely on physical or mathematical intuition and has a strong 'trial and error' component. There are, however, a few physical constraints which a reasonable functional has to fulfill, in particular sum rules have to be valid for the exact exchange-correlation holes. The exchange-correlation energy results from the integral over the exchange-correlation potential and in principle the correct energy could be obtained even from an erroneous potential if a fortuitous error cancellation appears.

In terms of *adiabatic connection* exchange-correlation energy of the Kohn-Sham scheme can be expressed through the coupling-strength integrated exchange-correlation hole $\bar{h}_{XC}$

$$E_{XC} = \frac{1}{2} \iint \frac{\rho(\mathbf{r})\bar{h}_{XC}(\mathbf{r}_1; \mathbf{r}_2)}{r_{12}} d\mathbf{r}_1 d\mathbf{r}_2, \tag{2.18}$$

where $\bar{h}_{XC}(\mathbf{r}_1;\mathbf{r}_2) \equiv \int_0^1 h^{\lambda}_{XC}(\mathbf{r}_1;\mathbf{r}_2)d\lambda$, λ is the coupling strength parameter, $h_{XC}(\mathbf{r}_1,\mathbf{r}_2)$ is the exchange-correlation hole and is defined as the difference between correlation $\Omega(\mathbf{r}_1,\mathbf{r}_2)$ and the uncorrelated probability $\rho(\mathbf{r}_2)$ of finding an electron at $\mathbf{r}_2$

$$h_{XC}(\mathbf{r}_1,\mathbf{r}_2) = \frac{\rho_2(\mathbf{r}_1,\mathbf{r}_2)}{\rho(\mathbf{r}_1)} - \rho(\mathbf{r}_2). \tag{2.19}$$

Correlation probability is defined as $\Omega(\mathbf{r}_1,\mathbf{r}_2) = \rho_2(\mathbf{r}_1,\mathbf{r}_2)/\rho(\mathbf{r}_1)$, where $\rho_2(\mathbf{r}_1,\mathbf{r}_2)$ is a spinless pair density that contains information about the probability of finding not one but a pair of two electrons simultaneously within two volume elements $d\mathbf{r}_1$ and $d\mathbf{r}_2$, while the remaining $N-2$ electrons have arbitrary positions and spins

$$\begin{aligned} \rho(\mathbf{r}_1,\mathbf{r}_2) = N(N-1)\int \dots \int |\Psi(\mathbf{x}_1,\mathbf{x}_2,\dots,\mathbf{x}_N)|^2 \\ \times\, ds_1, ds_2, d\mathbf{x}_3, \mathbf{x}_4 \dots d\mathbf{x}_N. \end{aligned} \tag{2.20}$$

The pair density represents diagonal elements of the spinless 'reduced density matrix for two electrons' defined as

$$\begin{aligned} \gamma_2(\mathbf{r}_1,\mathbf{r}_2;\mathbf{r}'_1,\mathbf{r}'_2) = \int \dots \int \Psi(\mathbf{x}_1,\mathbf{x}_2 \dots \mathbf{x}_N)\ \Psi^*(\mathbf{x}'_1,\mathbf{x}'_2 \dots \mathbf{x}'_N) \\ \times\, ds_1, ds_2, d\mathbf{x}_3, \mathbf{x}_4 \dots d\mathbf{x}_N. \end{aligned} \tag{2.21}$$

Exchange correlation hole integrates to -1 (contains the charge of one electron)

$$\int h_{XC}(\mathbf{r}_1,\mathbf{r}_2)d\mathbf{r}_2 = -1. \tag{2.22}$$

It can be split into a Fermi hole (representing the Pauli principle) and a Coulomb hole (representing Coulomb interaction). In the Hartree-Fock approach a Fermi hole is accounted by a single Slater determinant, whereas the Coulomb hole is neglected, so the exchange energy is accounted for in the Hartree-Fock approach. A Fermi hole like exchange-correlation hole integrates to -1, while a Coulomb hole integrates to zero.

Local density and local spin-density approximations

'I believe that formal density-functional theory would have been of very little interest if there had not been a simple and very practical approximation for E_{XC}, the local-density approximation (LDA), which has yielded surprisingly accurate results...' - W. Kohn[2]. Central to this model is the assumption that we can write E_{XC} in the

---

[2] NATO ASI Series, vol. 337.

following form

$$E_{XC}^{LDA}[\rho] = \int \rho(\mathbf{r})\varepsilon_{XC}(\rho(\mathbf{r}))dr, \tag{2.23}$$

where $\varepsilon_{XC}(\rho(\mathbf{r}))$ is the exchange-correlation energy per particle for a uniform electron gas of density $\rho(\mathbf{r})$. This energy is weighted with the probability $\rho(\mathbf{r})$ that there is in fact an electron at this point in space. $\varepsilon_{XC}(\rho(\mathbf{r}))$ can be split into exchange $\varepsilon_X(\rho(\mathbf{r}))$ and correlation $\varepsilon_C(\rho(\mathbf{r}))$ contributions such that $\varepsilon_{XC}(\rho(\mathbf{r})) = \varepsilon_X(\rho(\mathbf{r})) + \varepsilon_C(\rho(\mathbf{r}))$. Expression for ε_X was originally derived by Bloch and Dirac in the late 1920's

$$\varepsilon_X = -\frac{3}{4}\sqrt[3]{\frac{3}{\rho(\mathbf{r})\pi}} \tag{2.24}$$

Accurate values of $\varepsilon_C(\rho)$ are available, thanks to the quantum Monte Carlo calculations of Ceperley and Alder [44]. These values have been interpolated to provide an analytic form for $\varepsilon_C(\rho)$ [45, 46]. There are expressions obtained on the basis of numerical calculations, like Perdew and Wang [46] or Perdew and Zunger [47] both parameterizing Ceperley and Alder results. If we extend the LDA to the unrestricted case, we arrive at the local spin-density approximation.

The gradient expansion approximation and generalized gradient approximation

In gradient expansion approximarion (GEA) we expect to obtain a better approximation of the exchange correlation functional by taking the gradient of the local density within the Taylor expansion. Unfortunately GEA does not lead to the improved accuracy but frequently performs worse than the simple LDA. The reason is that the exchange correlation hole associated with such functional has lost many of the properties which made the LDA hole physically meaningful.

This problem was solved by straight-forward enforcing the restrictions valid for true holes also for the hole of the beyond LDA functionals. E.g. if there are parts in the GEA exchange holes which violate the requirements of being negative everywhere, just set them to zero. Functionals that include the gradient of the charge density and where the hole constraints have been restored in the above manner are known as generalized gradient approximations (GGA) [48–51]. These functionals are the workhorses of the current density functional theory. In practice E_{XC}^{GGA}, is usually split into its exchange E_X^{GGA} and correlation E_C^{GGA} contributions: $E_{XC}^{GGA} = E_X^{GGA} + E_C^{GGA}$. Approximations for the two terms are sought individually.

2.1.2 Pseudopotential

In this subsection I will follow the review article of Chelikowsky [52].

Mathematically and numerically a plane wave basis formalism is one of the simplest and most natural formalism to implement for crystals. However, expanding the core wave functions or the core oscillatory region of the valence wave functions into plane waves is extremely inefficient. Therefore plane-wave basis sets are practically always used in conjunction with the pseudopotential approximation. This combination of pseudopotentials and plane waves has become one of the most popular methods for electronic structure calculations [53].

The pseudopotential model treats matter as a sea of valence electrons mowing in a background of ions cores. The cores are composed of nuclei and inert electrons. The notion of replacing each atomic potential by a weak pseudopotential has been justified by an appeal to scattering theory. Historically it was arrived at in the study of the core orthogonality condition that dominates the OPW representation. Hellmann [54] argued that the effects of this condition could be simulated by a repulsive potential.

Despite this long history, the pseudopotential principle only came into general use with the demonstration by Philips and Kleinmann [55] and independently by Bassani and Celli [56], of the connection between this repulsive term and the OPW formalism [8, 57].

Within this model many of the complexities of all-electron calculation are avoided, for example it allows the electronic wave function to be expanded using a much smaller number of plane-wave basis states. In developing the pseudopotential initially a radial pseudo-wave-function is derived from the all-electron valence level with angular momentum l such that: (1) the pseudo-wave-function and the all-electron wave-function correspond to the same eigenvalue and logarithmic derivatives of their radial component (and thus the respective potentials) agree beyond a chosen core cutoff radius r_{cl}; (2) the radial pseudo-wave-function has the same amplitude as the all electron wave-function beyond the core cut-off radius and is norm conserving, i.e. two wave functions generate the same charge densities; (3) the pseudo-wave-function contains no radial nodes.

Constructing a pseudo-wave function that fulfils these requirements can be accomplished using many different schemes (e.g. [53, 58–63]). Most modern pseudopotentials are not fitted to experimental data but, are based on density functional theory. Within this theory the many body problem is mapped on to a one-electron Hamiltonian. The effects of exchange and correlation interaction are subsumed into a one-electron potential that depends only on the charge density. Without this procedure most electronic structure methods would not be feasible for systems of more than a few atoms.

The root of this method dates back to the early work of Fermi, e.g. the Thomas-Fermi screening model of the atom [33, 34, 52]. This mapping of the many-body problem to a one body problem often incorporates an additional approximation - LDA or GGA. LDA allows one to construct self-consistent field pseudopotentials for condensed matter systems. The chief limitation of these approximations is that they are appropriate only for the ground state structure and cannot be used to describe excited states without other approximations. As such one uses LDA to determine structural energies, compressibilities, elastic constants, vibrational modes, and so on, but not energy band gaps from the eigenvalue spectra. With respect to band gaps and electronic excitations, it is possible to consider these by implementing linear response theory on top of the standard LDA calculations. At present GGA significantly improves enthalpy terms and cohesive energies, but does not always improve structural properties when compared to experiment [52].

In 1980, Kerker [64] proposed a straightforward method for constructing local density pseudopotentials that retained the norm conserving criterion. He suggested that the pseudowave function have the following form

$$\begin{aligned} \phi_p(r) &= r^{l+1}\exp(p(r)) \quad for \quad r < r_c \\ \phi_p(r) &= \psi_{AE}(r) \quad for \quad r > r_c \end{aligned} \tag{2.25}$$

where $p(r) = -a_0 r^4 - a_1 r^3 - a_2 r^2 - a_3$. In the polynomial expansion the term linear in r is not present to avoid a singularity of the screened pseudopotential at $r = 0$. It should be noted that Kerker's pseudopotential has a discontinuity in its third derivative at the origin and at the cut-off radius.

Other local density pseudopotentials include those proposed by Hamann, Schlüter, and Chiang [60] Bachelet, Haman, and Schlüter [59] and Greenside and Schlüter [61]. These pseudopotentials were constructed from different perspective. The all electron potential was calculated from for the free atom. This potential was multiplied by a smooth, short range cut-off function which removes the strongly attractive and singular part of the potential. The cut-off function is adjusted numerically to yield eigenvalues equal to the all electron wave functions outside the core region.

The pseudocharge within the core is constrained to be equal to the all electron value [52].

There is some flexibility in constructing pseudopotentials. While all local density pseudopotentials impose the condition that $\phi_p(r) = \psi_{AE}(r)$ for $r > r_{cl}$, the construction for $r < r_{cl}$ is not unique. This attribute can be exploited to optimize the convergence of the pseudopotentials for the basis of interest.

An outstanding issue that remains unresolved is the best criterion to use in constructing an optimal pseudopotential. An optimal pseudopotential is one that minimizes the number of basis functions required to achieve the desired goal; it yields a converged total energy yet does not sacrifice transferability, i.e. its ability to accurately describe the valence electrons in different atomic, molecular, and solid-state environments. Transferability depends critically on the choice of the core cutoff radii, the linearization of core-valence exchange-correlation, the frozen-core approximation underlying the pseudopotential's construction and the transformation of the semilocal into the fully separable form of the pseudopotential. These issues have been carefully discussed, e.g. Fuchs and Scheffler [65], Troullier and Martins [53], Chelikowsky [52].

The easiest approach to increase the pseudopotential transferability is to simply decrease the cutoff radius r_{cl} used to generate the pseudopotential and pseudo wave-functions, thereby reducing the difference between the all-electron and pseudopotential results. However, there are practical limits on how far we can decrease r_{cl}, for example r_{cl} must be larger than the outermost node of the all-electron wave function if we insist on having nodeless pseudo wave-functions [53].

One straightforward approach to optimizing a pseudopotential is to build additional constraints into the polynomial given in Eq. (2.25), for example suppose we write

$$p(r) = c_0 + \sum_{n=1}^{N} c_n r^n \tag{2.26}$$

In Kerker's scheme, $N = 4$. If we extend the expansion, we may impose additional constraints. Troullier and Martins [53] generalized Kerker's method by simply increasing the order n of the polynomial $p(r)$. They write Eq. (2.26) as

$$p(r) = c_0 + \sum_{n=1}^{6} c_{2n} r^{2n}. \tag{2.27}$$

The additional coefficients give us the variational freedom needed for investigating smoothness properties for a parametrized family of pseudopotentials. These potentials tend to be quite smooth and converge very rapidly in reciprocal space.

Nonlocality in the pseudopotential is often treated in Fourier space, but it may also be expressed in real space. The interactions between valence electrons and pseudo-ionic cores may be separated into a local potential and a Kleinman and Bylander [66] form of nonlocal pseudopotential in real space [52].

2.1.3 The *fhi98md* DFT-LDA code

The construction of pseudopotentials with the *fhi98md* package

The package *fhi98md* [67] has following features for creating pseudopotentials:

- density functional calculation of the all-electron atom in a reference (ground) state, within a scalar-relativistic framework and a chosen approximation for exchange-correlation. For the correlation part LDA representations given by Perdew and Wang and by Perdew and Zunger [47], both parameterizations of Ceperley and Alder's exact results for the uniform electron gas, may be used. Code includes the GGA functionals by Perdew and Wang [49], by Perdew, Burke, and Ernzernhof [50], and Becke's formula for for the exchange part [43] combined with Perdew's formula for correlation [49]. Substituting for the latter the formula of Lee, Yang, and Parr [68] provides the so-called BLYP GGA.
- construction of the pseudo-valence orbitals and screened pseudopotential components, observing the norm-conserving constraints using either the Hamman's [58] or Troullier and Martins' [53] scheme.
- removal of the electrostatic and exchange-correlation components due to the valence electrons from the screened pseudopotential, optionally taking nonlinear core-valence effects into account.
- assessment of the pseudopotential's transferability by a transformation to fully separable Kleinman-Bylander [66] form and the exclusion of unphysical 'ghost states'.

Applications of the package in this work

Most of the DFT-LDA calculations for this thesis were performed using the *fhi98md* program suite [67]. The programs perform accurate *ab initio* electronic structure calculations without introducing undue approximations. The package also permits

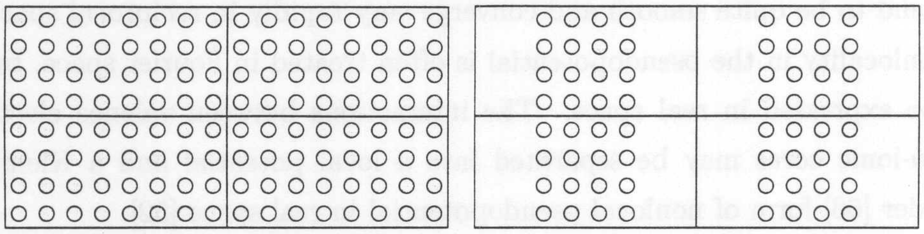

(a) bulk (b) surface

Figure 2.1: Schematic example of super-cell geometry in the simulation of the bulk and surface.

structure optimization method based on damped Newton ion dynamics[3]. Typically one calculates a band structure in three steps: in step one the structure is optimized, in step two very exact electron density calculation using a special k-point mesh is performed and in step three one calculates the band structure for the chosen high symmetry directions in the Brillouin zone. In the present version no spin effects are included in the program package.

The atomic geometries are given in periodic super-cell scheme. This simplification is useful especially for calculations of bulk properties, where the super-cell should be defined as a lattice primitive cell which is typically very small. The larger the size of the super-cell the longer the computation time, and the larger the memory requirements[4]. Fig. 2.1 shows how one creates a surface in the super-cell scheme. The resulting *slabs* are separated by the regions of vacuum. In this case the larger the slab and vacuum region the better the approximation. To provide some orientation the slab should not be smaller than 5 atomic layers, however, it may depend on the system and computational goal. Some groups [69] were using only 10 Å of vacuum region and this may be given as some limit. Adding an additional layer and vacuum region of 5 Å does not affect the computational time much even on state-of-the-art desktop computers and typically it may be better to use the biggest possible super-cells rather than save time, but the optimal slab will depend on the

---

[3] It should be noted that *ab initio* molecular dynamics within the Born-Oppenheimer approximation is also implemented but not used in this thesis.

[4] The current program version running on a Linux PC with 2 GB RAM is capable of making calculation on the slab of approximately $5 \times 5 \times 100$ Å containing 30 atoms of Zn and 30 of Se with the cut-off of 15 Ry, when the $3d$ are not explicitly included in Zn pseudopotential. For larger parameters memory allocation errors appear.

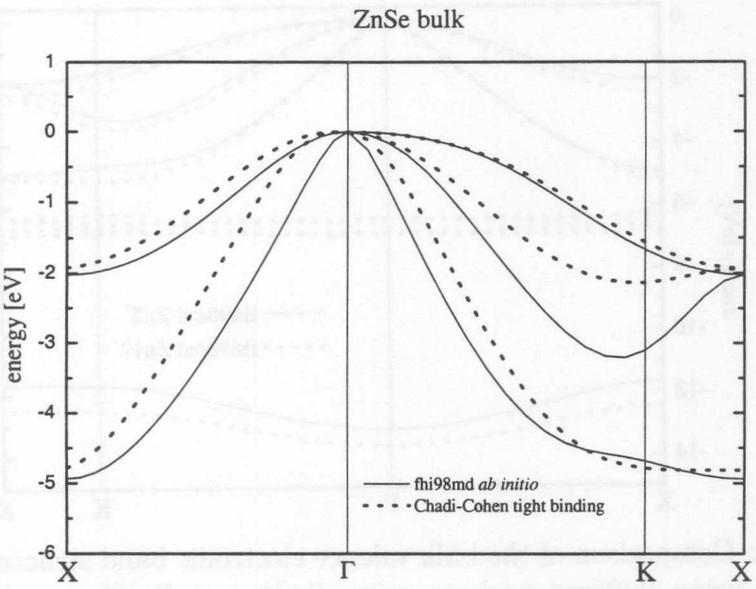

Figure 2.2: Comparison of the bulk valence electronic band structures calculated using tight binding [70] and DFT-LDA methods. Zero of the energy scale indicated valence band maximum.

system studied.

2.1.4 Results obtained using different methods

In Fig. 2.2 calculations using tight binding and DFT-LDA methods are presented[5]. The biggest difference between the two structures is observed around the K Brillouin zone point. This is a consequence of using only nearest-neighbor interactions in the tight-binding code [70]. It should be noted that the character of the band dispersion depends mainly on the crystal structure and is similar for all materials having the same structure (e.g. zinc-blende GaAs, ZnSe, CdTe and many others). The method of Chadi-Cohen [70] is not parameter-free and during the calculations one changes several parameters to obtain the best agreement e.g. with experimental results.

Pseudopotentials represent only a pseudo-atom with valence electrons only in contrast to all-electron atom. The choice of pseudopotential is not unique with respect to the number of electrons that are included in the pseudo-atom. Zinc has 12 electrons in the valence band: $[Ar]3d^{10}4s^2$. When creating the pseudopotential

---

[5] The Chadi-Cohen tight binding code based on [70] is available in the web under http://www.wag.caltech.edu/home/rpm/projects/tight-binding/. The code was written by Richard P. Muller and is distributed as freeware under the GNU license.

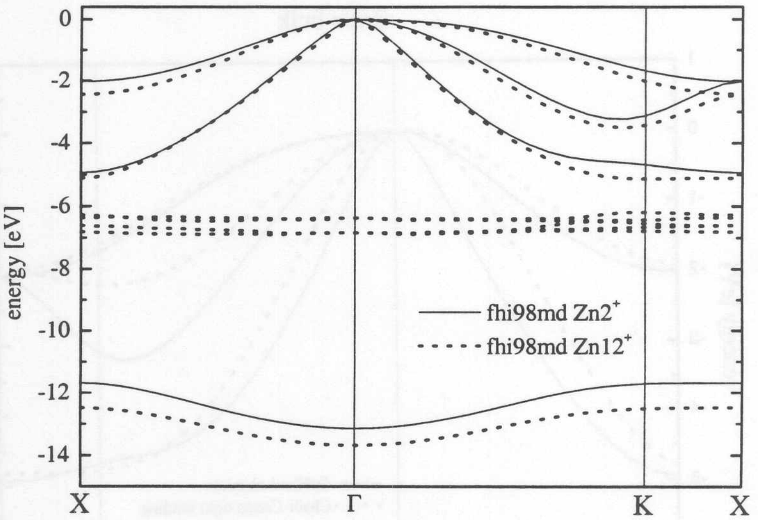

Figure 2.3: Comparison of the bulk valence electronic band structures of ZnSe calculated using fhi98md package using Zn^{2+} and Zn^{12+} pseudopotentials. Zero of the energy scale indicates valence band maximum.

one has to choose between Zn^{2+} that includes only the two 4*s* electrons and the full Zn^{12+} that includes all the valence band electrons[6]. For the case of zinc selenide the choice of Zn^{2+} is generally valid since the neglected 3*d* levels are quite well localized and only slightly interact with *s* and *p* states. The use of Zn^{2+} speeds up the calculation and reduces the memory allocation needed. A comparison of the structures obtained using the two zinc pseudopotentials is shown in Fig. 2.3. The band dispersions are very similar and validate the use of Zn^{2+}. Of course the zinc 3*d* electrons are not present in the Zn^{2+} calculation but these *shallow* core levels show only a very small dispersion and are typically not a subject of a valence band structure study.

Moreover the result for Zn^{12+} is not optimized and shows wrong position for the 3*d* levels that should lie about 2 eV deeper, at around −9 eV energy. This is a common result [73, 74] which can be corrected e.g. by using sophisticated 'broken symmetry' band structure approach [75] or SIRC-PP methods [76]. On the other hand optimized Zn^{2+} and Se^{6+} pseudopotentials were used that were carefully tested [77]. One can see that the complete valence band structure of ZnSe can be divided into a deep *s*-like band at around −12 eV, the so called *antisymmetric* [78]

---

[6] The nomenclature of the pseudopotentials after Gundel *et al.* [71].

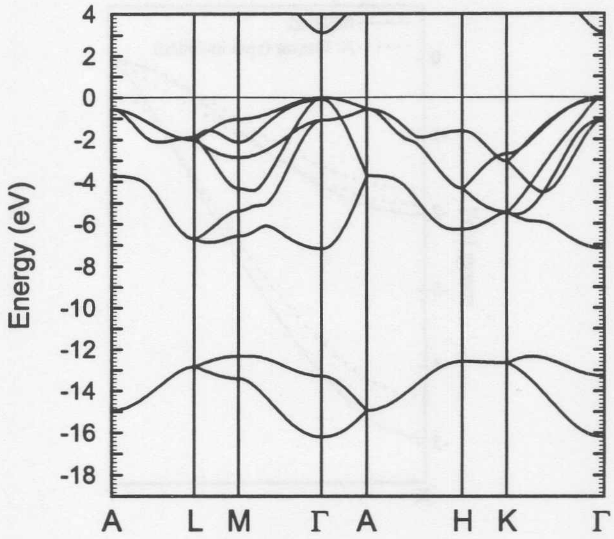

Figure 2.4: Bulk band structure of GaN calculated by Strasser *et al.* [72].

band gap[7] between −12 and −5 eV with the *shallow* 3*d* core lying within and the upper part of the valence band between around −5 and 0 eV. Over this band there is a fundamental optical gap. A similar situation is found in the case of the GaN band structure presented in Fig. 2.4, calculated with the LCAO extended-Hückel-theory [79] by Strasser *et al.* [72]. The calculation was performed with a set of 4*s* and 4*p* atomic orbitals for gallium and 2*s* and 2*p* atomic orbitals for nitrogen taking into account the coupling up to fourth nearest neighbor atoms[8]. The lowest band in the picture for −16 to −12 eV originate from N 2*s* states. The valence band for −7 to 0 eV contains a mix of all atomic levels, however, close to the VBM almost only N 2*p* levels account for the density of states [72, 80].

Another important issue when calculating a band structure is the spin-orbit interaction. It is mainly apparent near the Γ point in the Brillouin zone and can be observed by state-of-the-art experimental methods. The calculations of Andrzej Fleszar (published by Dröge *et al.* [81]) include spin-orbit interactions. The comparison presented in Fig 2.5 shows the splitting of 0.43 eV at Γ point compared to the *fhi98md* result. These results are further discussed in the experimental part of

---

[7] This band gap is a result of the ionicity (charge transfer between Zn and Se) of the crystal and it is not present in simple fcc materials like Si or Ge.

[8] The Ga 3*d* levels are not taken into account and therefore not present in the band structure plot. From experiments and other calculations it is known that they create a flat band at around −17 eV.

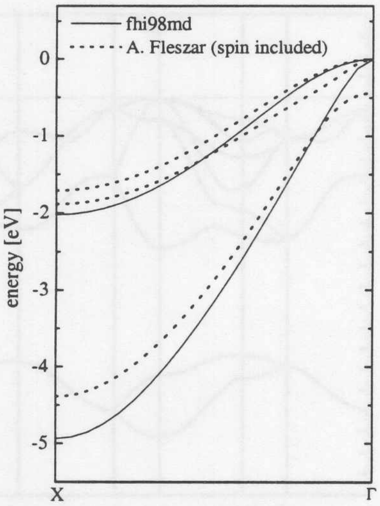

Figure 2.5: Comparison of the bulk valence electronic band structures for ZnSe calculated using fhi98md package and by A. Fleszar using his code. The code of A.F. includes spin effects and therefore the splitting of the bands at Γ due to spin-orbit interaction is observed.

the thesis.

2.2 Surface - geometry and electronic structure

2.2.1 General statements

The termination of a bulk crystal surface to create a surface modifies both its geometry and electronic properties. The lattice tries to minimize the potential energy step on the surface by *relaxation* i.e. rearrangement of the atomic positions. Such a rearrangement occurs at all surfaces and typically extend over the first 3 - 5 atomic layers. For deeper layers the displacements are negligible. Often it is energetically more preferable if the arrangement of the atoms near the surface has a periodicity different than the ideally terminated bulk crystal. This process is called *reconstruction* of the surface. Separation of relaxation and reconstruction is sometimes artificial, however, from a practical point of view relaxation of the surface can be performed with the computer code by minimizing the total energy of the system. Reconstruction on experimentally prepared surfaces can be easily inspected using electron diffraction techniques.

Typically in these 3 - 5 relaxed and sometimes reconstructed surface layers new,

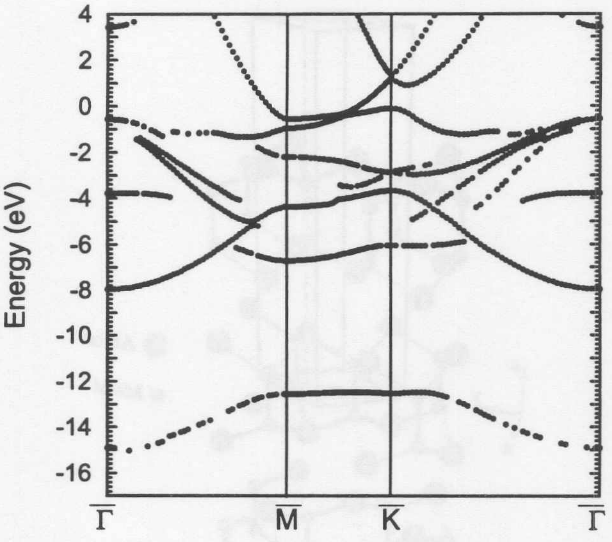

Figure 2.6: Surface electronic structure of GaN(000$\bar{1}$) calculated by T. Strasser *et al.* [72]. Shaded areas represent projected bulk band structure.

two-dimensionally localized, *surface* electronic bands are created. These bands are called surface *states* if they lie within the gap of the bulk band structure projected on the surface or surface *resonances* is they lie in the projected band structure. An example of the surface band structure is presented in Fig. 2.6, these results are discussed in the Chapter 4.

Historically the surface states were first described by Tamm [82] for the case of tightly bound electrons in the surface region and Shockley [83] for the case of nearly-free-electrons in the presence of ideal surface. They are often called *Shockley* and *Tamm states* respectively. There is no real physical distinction between the different terms [84].

It is necessary to note that there are materials whose surfaces are in general passive and practically neither reconstruct nor relax. These are so called *layered crystals* where the *sandwiches* of strongly bonded atomic layers are separated by few angstroms and the bonding between the layers is mainly of van der Waals type. Fig. 2.7 shows the crystal structure of β-GaSe[9] and it is easy to see highly separated *sandwiches*, from this picture it is easy to imagine why the surface of this material

---

[9] There are three politypes of GaSe: β-GaSe, ϵ-GaSe and γ-GaSe. For the information about the politypes check Ref. [85] and for the most recent theoretical study of GaSe electronic srtucture check Ref. [86].

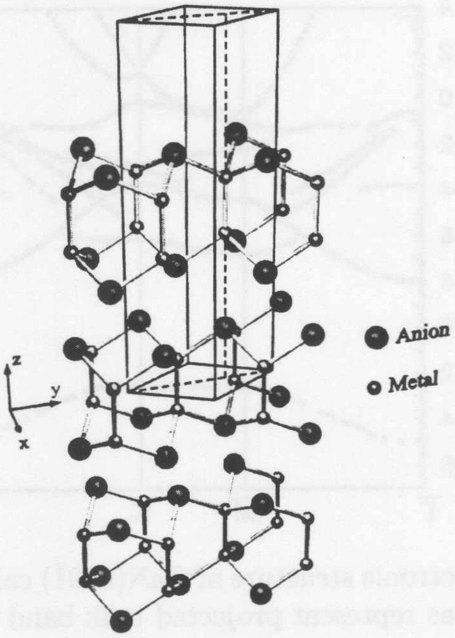

Figure 2.7: Crystal structure of the layered compound (in this case β-GaSe). The hexagonal lattice cell is 15.94 Å long in z-direction. The lattice constant in xy-plane is $a_0 = 3.755$ Å.

is stable and passive[10].

2.2.2 Calculations with the *fhi98md* code

Using *fhi98md* one can relax the positions of the surface atoms, calculate detailed charge densities and the band structure of the surface. The necessary steps are explained below.

The program *fhi98md* works with periodic super-cells and therefore to create a surface one has to create a super-cell long in one direction and only partially filled with atoms i.e. a significant part of the super-cell should be empty. Periodical multiplication of the super-cells creates *slabs* that have surface on both sides and are separated by the vacuum regions.

In the creation of the slab surface one should use available experimental and theoretical data concerning the relevant atomic positions. If no input data is available for the system to be investigated bulk positions could be used as a starting point.

---

[10] There is *always* some relaxation in the surface region and indeed it takes place also in case of GaSe but its effect is practically negligible in case of band structure.

The slab should be constructed in such way that one super-cell contains one surface lattice cell.

The next step is to perform the relaxation of the atomic positions; *fhi98md* finds the equilibrium geometry within the damped Newton scheme. One can choose which atoms are allowed to move and relaxation of the first three atomic layers is typical, viz published literature [87–89]. The atomic positions should be optimized until the force on each atom is minimized. A typical maximum force per atom in the relaxed system should not be higher than 0.5 eV/Å, however, in some cases such good optimization is not necessary.

After the atomic positions are optimized one performs an exact total energy minimization with respect to the spatial charge density. The k-point sampling in the Brillouin zone and the energy cutoff should be optimized to obtain the best computational speed with the desired accuracy. In the next step this spatial charge density is used to calculate the band structure at selected points in the Brillouin zone. For surface structures only the projection of the coordinates on the surface plane matters. This calculation yields as many bands as the number of electrons in the super-cell. The last step is to identify the bands that are localized in the surface region. For that one has to analyze the charge densities for every electron and every k-point[11]. Such a calculated surface band structure is usually plotted together with the projected bulk band structure which should be calculated in addition for the bulk material.

---

[11] Typical super-cell for exact surface structure calculation may contain more than one hundred electrons so it means that in case of 20 k points one has to inspect more than 2000 charge densities.

2.3 Photoemission theory

The theory of photoemission has always been a theory of angle-resolved photoemission since angular effects have to be calculated before integrating over the angles to describe traditional angle-integrated data [90]. The first theoretical calculations dedicated to the angular dependence of the photocurrent were performed within the three-step-model formalism in 1970 by Mahan [91] and Schaich and Ashcroft [92]. They were motivated by the fact that the experimental developments had reached the point where it was possible to measure the unscattered electrons from the solid crystal and therefore direct mapping of the electronic bands with the k-resolution. Later a lot of work was made to include quantum formalism (e.g. [93]) and today's state-of-the-art methods calculate the photocurrent within a proper, quantum-dynamical, one-step model [94].

2.3.1 Mean free path

The mean free path of the electrons inside the bulk material depends on the kinetic energy of the electrons. In the frame of this work the electron energies up to E_{kin} = 40 eV are of interest[12] and the mean free path at such energies is typically of the order of 10 Å (equals 2-3 lattice constants of the typical semiconductor single crystal sample). The schematic explanation of how the mean free path effects the photoemission process is presented in Fig. 2.8. Vacuum-ultraviolet (VUV) photons impinging on the surface may penetrate up to around 1000 Å inside the bulk material. However, only the electrons that interact with photons in the first few layers under the surface can leave the sample without being scattered[13]. This is the reason why photoemission is a highly surface sensitive technique. The goal of an angle-resolved photoemission experiment is to reconstruct the initial momentum of the electrons inside the crystal and scattered electrons are useless for this purpose. In Fig 2.9 one can see a typical normal emission photoemission spectrum taken at E_{ph} = 25 eV which can be separated into three regions. The peak around electron energy E_{kin} = 13.5 eV is related to the zinc $3d$ shallow-core levels[14] and between 16.5 and

---

[12] This is related to the photon energies E_{ph} = 10 - 40 eV used in the experiments presented here.

[13] In this thesis will be considered neither two photon processes nor electrons scattered inside the sample. Such processes are important at higher photon beam intensities than available here.

[14] Note that the Se core levels cannot be reached at this photon energy. Zn $3d$ states are shallow-core levels very often called *semicore* levels since they lie within the valence band (see Fig. 2.3)

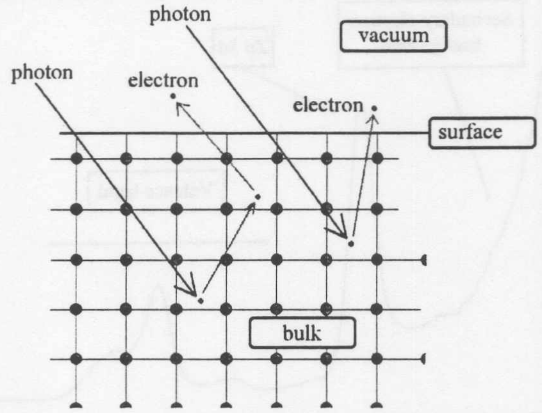

Figure 2.8: The picture shows the schematic view of the surface of a semiconductor. The two cases of photoemission processes are shown: electron that interacts with a photon can either be scattered before leaving the sample or it can leave without scattering. Only unscattered electrons carry the information about their initial state and are important for angle-resolved photoemission measurements.

23 eV the valence band of interest appears. The part for the lowest electron kinetic energy is a scattering tail (also called the secondary electron tail). This low-energy electron background is produced mainly by electron-electron scattering inside the sample as indicated in Fig. 2.8[15].

2.3.2 Phenomenological three-step and quantum-dynamical one-step photoemission models

The detailed theoretical description of the photoemission process and experimental examples are presented in numerous books and papers e.g. Cardona and Ley [96], Hüfner [97], Himpsel [90], Yu and Cardona [98]. Here only a brief outline of the three-step-model and the scattering approach to photoemission will be given.

The three-step model is a phenomenological approach for the interpretation of the photoemission process developed by Berglund and Spicer [99,100]. It breaks the photoemission process into three steps: (1) photoexcitation of the photoelectron inside the solid, (2) transport to the surface and (3) escape of the electron into

---

and are not as well localized as typical core levels. However, in this thesis the dispersion of Zn 3*d* states is not investigated and their influence on the valence band is neglected.

[15] Electrons can interact either via pair creation or plasmon creation [95].

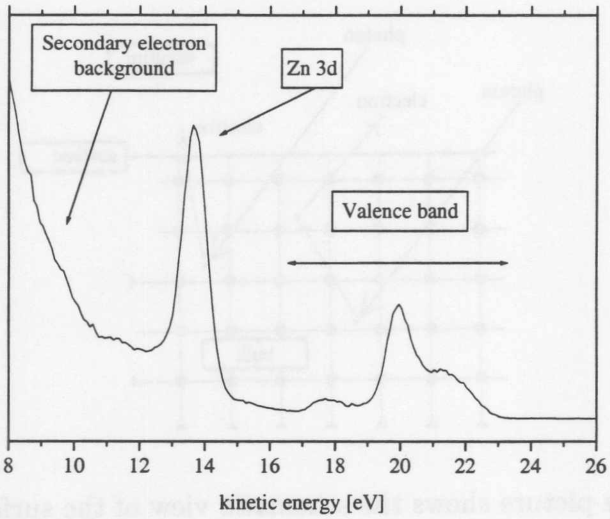

Figure 2.9: The graph shows the typical EDC from ZnSe(001) surface. Incident photon energy was $\hbar\omega = 25$ eV.

vacuum. One should distinguish between the three wave-vectors that characterize the electron[16]:

- $\mathbf{k}_i$ is the initial wave-vector of the electron before photoexcitation.
- $\mathbf{k}_f$ is the final wave-vector of the electron inside the bulk after photoexcitation.
- $\mathbf{K}$ characterizes the momentum of the emitted photoelectron in vacuum[17].

In step (1) the momentum of the photon can be neglected

$$\mathbf{k}_f = \mathbf{k}_i + \mathbf{k}_{ph} \approx \mathbf{k}_i. \tag{2.28}$$

While neglecting the photon momentum is permissible in the VUV range of photon energies the main inaccuracy of step (1), and the whole model, is due to considering bulk final state as a photoemission final state. In step (2) one calculates the fraction of the electrons that reach the surface unscattered. Mean free path explained in the previous subsection plays the dominant role here. Only electrons that reach the surface with sufficient kinetic energy can overcome the potential barrier in step (3). The step-like surface potential leaves $k_{f\|}$ conserved (except for a surface reciprocal lattice vector $\mathbf{G}_{surf}$) as is schematically shown in Fig. 2.10 and influences only the $k_{f\perp}$ component of the electron momentum.

---

[16] We follow here the notation from [101] and [102].

[17] $\mathbf{K} = \mathbf{p}/\hbar$, where $\mathbf{p}$ is the momentum of the emitted electron in vacuum.

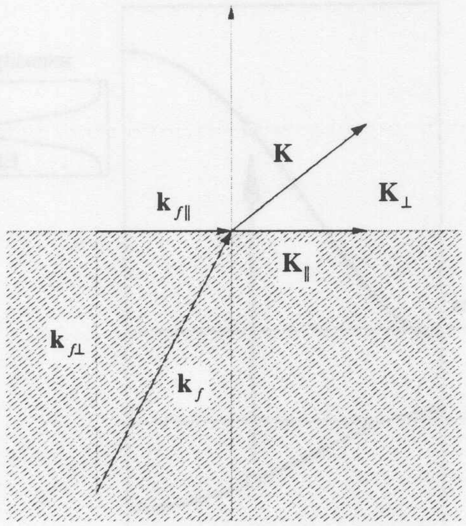

Figure 2.10: The component of the wave vector parallel to the surface $\mathbf{k}_{f||} = \mathbf{K}_{||}$ is conserved upon transmission of the electron through the surface.

The expression for the photocurrent can be written in the form [102]

$$\begin{aligned} I(E,\hbar\omega) &\propto \sum_{f,i} |M_{fi}|^2\, \delta(\mathbf{k}_f - \mathbf{k}_i - \mathbf{G})\, \delta(E_f - \hbar\omega - E_i) \\ &\quad \times \delta(\mathbf{K}_{||} - \mathbf{k}_{f||} - \mathbf{G}_{surf})\, \delta(E_{kin} - E_f) \end{aligned} \tag{2.29}$$

where processes taking place in step (2) are neglected because they do not influence the energies of the emitted electrons but only intensities. The factor

$$|M_{fi}|^2\, \delta(\mathbf{k}_f - \mathbf{k}_i + \mathbf{G}) = |\langle f, \mathbf{k}_f | \mathbf{A}\cdot\mathbf{p} | i, \mathbf{k}_i\rangle|^2, \tag{2.30}$$

where $\mathbf{A}\cdot\mathbf{p}$ is the interaction Hamiltonian within the dipole approximation, represents the photoemission step (1), and the Kronecker δ function implies direct transitions within the reduced Brillouin zone. The second δ function in (2.29) is the energy conservation rule inside the crystal and last two are momentum and energy conservation rules at the solid-vacuum interface.

The one-step model is a proper quantum dynamical approach to the photoemission process. The method of calculating the photocurrent was developed at Kiel university in the group of Prof. W. Schattke [103, 104]. The photocurrent may be calculated via [94]

$$\begin{aligned} I &\propto \sum_{i,j} \langle \Phi^*_{LEED}(E_f, k_{||}) | \mathbf{A}_0 \cdot \mathbf{p} | \Psi_i \rangle \\ &\quad \times G_{i,j}(E_f - \hbar\omega, k_{||}) \langle \Psi_j | \mathbf{p}\cdot\mathbf{A}_0 | \Phi^*_{LEED}(E_f, k_{||}) \rangle \end{aligned} \tag{2.31}$$

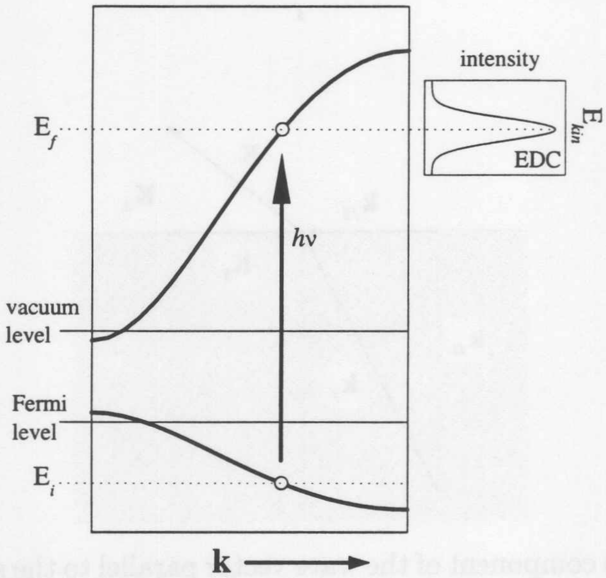

Figure 2.11: Photoemission experiment in EDC mode as viewed in momentum space.

where $G_{i,j}$ is the half space Green function of the valence states in the LCAO basis (i, j) and the dipole approximation is made for the Hamiltonian. The inverse low-energy electron diffraction (LEED) function Φ^*_{LEED} is chosen as a final state[18]. Combining this approach with angle-resolved experiments allows a more realistic interpretation of the bulk and surface electronic structure. One can extend this model beyond the dipole approximation and include many-body effects. In this work extensive use of the one-step results by Thomas Strasser for GaN [72] will be made.

2.3.3 Free-electron final state model

The goal is to identify the initial $\mathbf{k}_i$ wave vector knowing the kinetic energy E_{kin} and the angle ϑ (with respect to the surface normal) of the photo-emitted electron. If the final state inside the crystal (as shown e.g. in Fig. 2.11) is assumed to be a free-electron parabola the situation can be simplified within the three-step model. It is important to remember that the crystal can provide the reciprocal lattice vector

---

[18] LEED is explained in the next next chapter of the thesis.

$\mathbf{G}$ allowing direct transitions in the reduced zone scheme

$$E(\mathbf{k}) = \frac{\hbar^2}{2m}|\mathbf{k}_f|^2 = \frac{\hbar^2}{2m}|\mathbf{k}_i + \mathbf{G}|^2 \tag{2.32}$$

In the framework of three-step model the $\mathbf{K}_{||} = \mathbf{k}_{f||} + \mathbf{G}_{surf}$ vector is conserved (third Kronecker's δ in Eq. (2.29)) and therefore it can be calculated as[19]

$$\begin{aligned} \mathbf{k}_{i||} &= \mathbf{k}_{f||} - \mathbf{G}_{||} = \mathbf{K}_{||} - \mathbf{G}_{surf} - \mathbf{G}_{||} \\ \mathbf{k}_{i||} &= \sqrt{\frac{2m}{\hbar}E_{kin}}\sin\vartheta - \mathbf{G}_{surf} - \mathbf{G}_{||} \end{aligned} \tag{2.33}$$

The similar formula can also be written for $k_\perp$, however, here the situation is bit more complicated because the step potential at the surface must be included. This results in refraction on the surface that is characterized by an inner potential V_0, such that $E_{kin} = E_f - V_0$, which can be evaluated experimentally (see section 3.4). In case of $\mathbf{G}_{surf} = \mathbf{G}_{||} = 0$ the formula has the form[20]

$$\mathbf{k}_{i\perp} = \sqrt{\frac{2m}{\hbar}(E_{kin}\cos^2\vartheta + V_0)} + G_\perp. \tag{2.34}$$

For the electrons with the vacuum momentum perpendicular to the surface one can use this formula [101]

$$\mathbf{k}_{i\perp} = \sqrt{\frac{2m}{\hbar}(E_{kin} + V_0) + |\mathbf{G}_{surf}|^2} + G_\perp. \tag{2.35}$$

In all typical cases the ensemble of $\mathbf{G}_{||}$ is a subset of $\mathbf{G}_{surf}$ and therefore in practice $\mathbf{G}_{||}$ is always included in $\mathbf{G}_{surf}$ and that's why it doesn't appear in Eq. (2.35). This allows to use $G_\perp$ independently in this equation[21].

Primary and secondary cone processes

The *primary cone* process takes place when $\mathbf{G}_{||} = 0$, $\mathbf{G}_{surf} = 0$ and this is the typical application of the free-electron final state model.

---

[19] Note that $\mathbf{G}_{surf}$ and $\mathbf{G}_{||}$ maybe different e.g. for a reconstructed surface.

[20] Note that $\mathbf{G} = \mathbf{G}_{||} + G_\perp$, where we don't write $G_\perp$ as a vector since it has a defined direction. $\mathbf{G}_{||}$ is noted as a vector but restricted to a two-dimensional surface. One should also note that in the case of $\mathbf{G}_{||} = 0$ we have $\mathbf{G} = G_\perp$.

[21] This fact can be misleading and therefore one should always remember that vectors $\mathbf{G}_{||}$ and $G_\perp$ are *not* independent in the case of off-normal experiment. $\mathbf{G}_{||}$ can be considered as independent when surface states or resonances are investigated since they have undefined $G_\perp$ but when bulk bands are investigated one has to use $\mathbf{G} = \mathbf{G}_{||} + G_\perp$ to determine the position of the features within the 3D Brillouin zone. This is the reason why the measurements at constant photon energy do not in general allow to map the bulk band structure over the significant portion of the Brillouin zone even in the frame of the simplest free-electron final state model, but are sufficient to map the surface band structure.

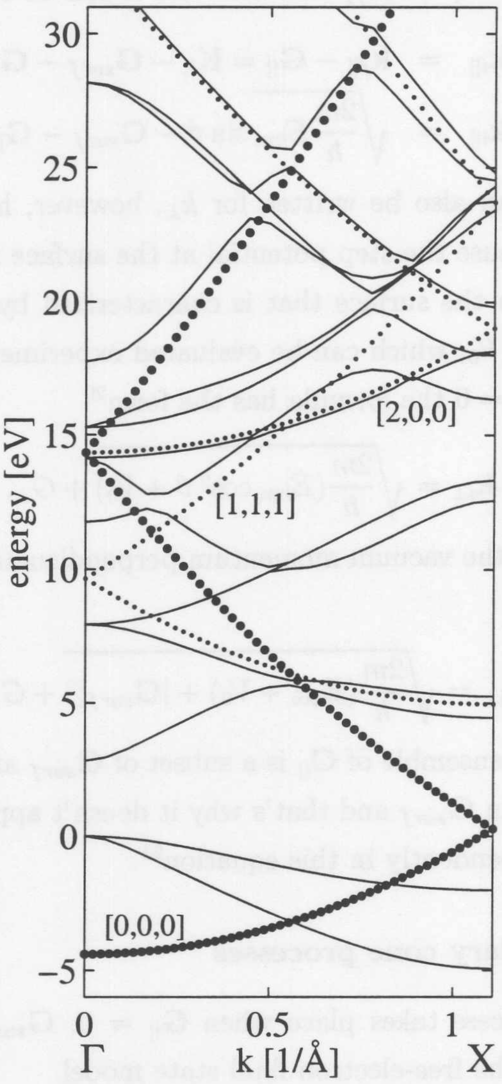

Figure 2.12: The final bands for the ZnSe(001) surface. Solid lines show the band calculated with the *fhi98md* code. The band gap was corrected to its experimental value of 2.82 eV. Thick dots show the primary cone parabola and small dots show secondary cone parabolas for this final energy region.

The *secondary cone* process takes place when the $G_{||} \neq 0$. Typically secondary cone processes have lower probabilities in comparison to the primary cone emissions. An analysis of the photoemission spectra with the use of secondary cone emissions can be found in many published papers e.g. [105, 106]. Secondary cone emissions can often lead to the misinterpretation of the spectra since they could create flat bands similar to surface states or resonances [107].

The primary and secondary cone final state parabolas can be easily visualized as shown in Fig. 2.12. Here the empirical parameter $V_0 = 11.2$ eV (that was the best fit between the experiment and the primary cone model - see Sec. 3.4) was used to shift the energies of the free-electron bands and one can see how it corresponds to the calculated final states.

Surface umklapp scattering

Surface *umklapp* process takes place when $\mathbf{G}_{surf} \neq 0$. Surface umklapp scattering is therefore similar to the secondary cone process, but here not the bulk crystal but a surface provides the reciprocal lattice vector. Since the surface reconstruction can have a different periodicity to the bulk material it can lead to different effects than secondary cone process. One has to also point out that even on an unreconstructed surface the result of umklapp scattering can be different to secondary cone process[22]. There is a wide literature on the observation of surface umklapp scattering in angle-resolved photoemission [106, 108–111]. A typical effect is that short reciprocal vectors of the reconstructed surface lead to less directional character of the emitted primary-cone electrons [112].

Advantages and disadvantages of the model

The free-electron final state model is frequently used to evaluate initial **k** vectors from angle-resolved photoemission data. The results on simple metals (e.g. Cu [97, 113]) and some semiconductors (e.g. GaAs [114]) are in very good agreement with the theory. There are experimental methods to determine the photoemission final states (Inverse Photoelectron Spectroscopy, Very Low Energy Electron Diffraction [115–117]), however, typically they provide rather small corrections to the band dispersions. Also theoretically calculated photoemission curves [72, 118]

---

[22] E.g. on zinc-blende (001) surface neither $\mathbf{G} = (2, 2, 0)$ nor $\mathbf{G} = (1, 1, 1)$ is not equal in length to the $\mathbf{G}_{surf} = (1, 1)$ and $(1, 1, 0)$ is not a reciprocal lattice vector.

are not always able to reproduce the experimental results exactly. I think there are some simple physical reasons for this situation. In the most simplified view one should note that a free-electron is the real final state of the photoemission experiment because the electrons photoemitted from the sample (and later collected in the channeltron) are free electrons. In this context we have the example of a mixed model: the real final state of the electrons is employed as the final state (inside the *periodic* crystal) in the three-step model.

Referring to Fig. 2.12 it is necessary to mention that not all of the final states can take part in the photoemission process in photoemission step (1). There are symmetry *selection rules* that determine which final band contributes significantly to the photoemission signal. A detailed description of selection rules is given e.g. by Hüfner [97] but from simplified point of view one can say that the calculated bands that are closer to the free-electron ones will take part in the photoemission process. Himpsel [119] pointed out using the example of Si published in [120][23] that it is surprising to see that a complex array of calculated upper bands behaves effectively like a parabolic band for generating the photoemission spectra. In yet another sentence he writes that the physics behind such a simplified situation is that the electron in the upper band has a high enough kinetic energy to feel only a weak, average influence of the crystal potential. This leads to a slightly different interpretation of the free-electron model; it works best when the crystal potential is weak such that the bulk band structure can be described by nearly free-electron approach. In this interpretation the transition to the free-electron band occurs inside the crystal. After excitation the electron is transported to the surface and the surface barrier is simply represented by a constant V_0. It is clear that for high kinetic energy of electrons the model works better because then the crystal potential plays a less significant role.

Typically for photon energies below 20 eV there are some intense features that cannot be explained within the free-electron model. In the case of semiconductors the significant band bending (and therefore departure from the free-electron shape) in the region of the fundamental gap may be responsible for that. Sometimes (also in this work) the use of the calculated final states or photoemission spectra can be very helpful to interpret such features.

---

[23] Those experiments were carried out at the same experimental synchrotron radiation beamline as the present work.

Chapter 3

Experimental techniques and apparatus

In this thesis new experimental results on the occupied electronic structure of wide band-gap semiconductors are presented. In this chapter the various experimental techniques used to characterize the samples are introduced.

3.1 Sample preparation

To perform a successful photoemission experiment in the VUV photon energy range it is necessary to prepare a sample with an atomically clean surface. Only electrons which leave the solid without any scattering events carry direct information about the electronic structure. The electron mean free path is in order of a few atomic layers for the case of the kinetic energies that are considered in this thesis as explained in subsection 2.3.1. If any contamination is present on the surface it will automatically reduce the number of electrons that carry the information about the electronic structure of the sample. To avoid surface contamination all the measurement must be performed under ultra-high vacuum (UHV) conditions[1].

There are several sample preparation techniques. In the case of semiconductors all the preparation must be carried out under UHV.

---

[1] 'Ultra-high vacuum' refers to total pressures below about $5 \cdot 10^{-9}$ mbar and the residual atmosphere should be free of reactive gases. The typical operational pressures in this work were below $5 \cdot 10^{-10}$ mbar. For a prolonged measurements (e.g. more than 24h without cleaning) it is preferred to maintain the base pressure in the 10^{-11} mbar range, however, it depends on the reactivity of the measured surface.

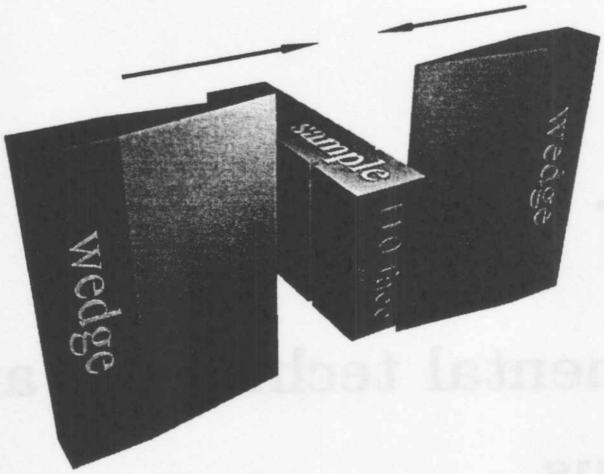

Figure 3.1: Schematic view of the cleaving tool that is used at Winkelemi experimental station at HASYLAB. A single crystal (in this case zinc-blende structure) should be prepared in appropriate way. Special notches made in the sample could help performing a successful cleave.

3.1.1 Cleaving

Cleaving in UHV is one of the best sample preparation techniques for photoemission. It is based on the fact that a single crystal material can be easily cleaved along selected crystallographic directions. A successful cleave produces a macroscopically flat surface that is atomically clean and immediately ready for performing measurements.

Cleaving can be realized in several ways. A wedge or knife-edge mechanism can be used to produce a crack along the desired orientation. Alternatively the tape or a metal post can be glued on the top of the sample and by knocking it off the sample is cleaved. This method works well for layered crystals.

Cleaving does not work with polycrystals and it usually produces unsatisfactory results when used on low quality crystals. Typically for a given material only one of the high symmetry crystallographic planes can be obtained by cleaving. In the case of the zinc-blende II-VI semiconductors only (110) direction can be prepared by cleaving.

3.1.2 Annealing

High temperature treatment is frequently needed in surface science experiments. Temperatures up to 500 – 600 °C are usually sufficient when heating compound semiconductors.

The most common heaters are tantalum or tungsten wire filaments. Such filament is usually placed under the sample to avoid contamination from the wire. One could improve this method and make it more local by applying additional high voltage between the bottom of the sample and the filament. Such a method is called e-beam heating because heat is produced mainly by the incident electron beam produced from the filament. Locally temperatures over 1000 °C can be easily achieved. Also resistive heaters clamped to the bottom of the sample are very often used.

Temperature measurements can be carried out using a thermocouple located close to the sample or with a pyrometer from the outside of the vacuum chamber through a suitable viewport.

By applying annealing only it is usually not possible to obtain surfaces of sufficient cleanness for photoemission experiments. However, in special cases it may be adequate. For example the samples grown by molecular beam epitaxy (MBE) can be capped under UHV after the growth process is finished. The cap should be a thick layer of an element which is easy to remove by heating. Ideally the cap should be one of the elements of the sample itself.

3.1.3 Sputtering

Usually even annealing to a very high temperature does not remove all the contamination from the surface. This is mainly because some of the contaminants can create very strong bonds to the surface atoms or diffuse a few layers into the sample. To remove such atoms one usually combines noble gas ion sputtering with annealing. Ion gas bombardment is realized with a special ion gun. The question of what ion bombardment really does to the surface is a complex topic; however, the simple interpretation is that due to momentum transfer it causes successive removal of surface layers. After sputtering the surface may become disordered and some hours of annealing is necessary for recrystallization.

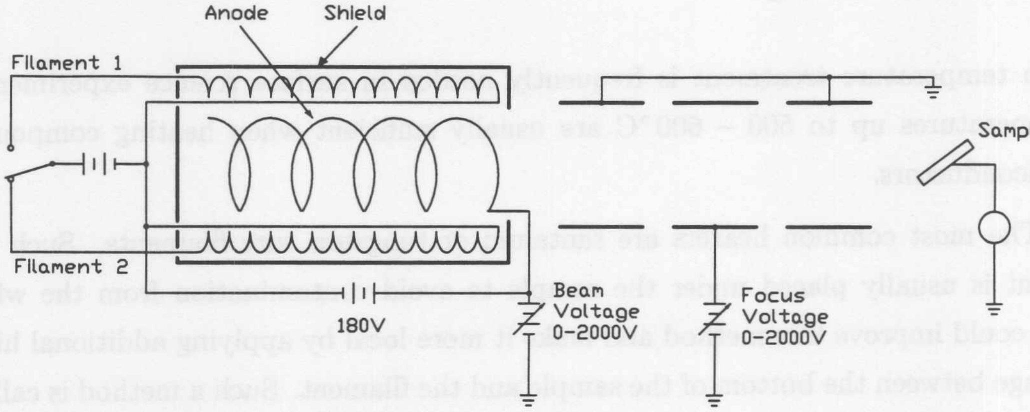

Figure 3.2: Scheme of the sputter gun used at the Winkelemi experimental station at HASYLAB (PHI model 04-161). Electrons that flow from the filament to the anode ionize the noble gas (usually Ar). The ions are accelerated towards the sample and a system of lenses is used for better focusing.

3.1.4 Cleaning procedures for different samples

It should be noted that the effort required to prepare a clean surface adequate for a photoemission study[2] in the VUV region depends very much on the material to be studied. There is a huge number of factors that determines why sometimes the preparation process may be rather fast for some materials and sometimes it may require a very time-consuming process of trying different recipes to develop the best preparation procedure that can take several weeks. Very often the readers of publications in the experimental surface science are not aware of the efforts put into the preparation of the surface. I would like to shortly compile my experience about the materials I prepared on the course of this thesis starting with the easiest one and provide some practical details that are typically not mentioned in papers published in international journals:

- **GaSe**: This is the easiest surface for preparation. The crystals are elastic platelets of about 1×1 cm^2 and few millimeters thick. The biggest problem is to stick them to the sample holder. We used a special low-vapor pressure silver epoxy to ensure electrical contact between the sample and sample holder. After gluing the ordinary commercial *"Scotch"* tape is pressed on the face of the sample. The sample is placed in the load-lock of the vacuum system and pumped until the pressure is in the 10^{-9} mbar range (it takes typically several hours). After that the sample

---

[2] Photoemission is explained in detail in the next subsections.

is transferred to the preparation chambers where it is cleaved - the Scotch tape is stripped off under UHV. Some of the layers stick to the tape and the rest of the sample has a clean surface. Since the surface of GaSe is practically passive, the UHV requirements are not very strict and the pressures of $1 \cdot 10^{-9}$ mbar allow measurements for a few days. Layered compounds are therefore predestinated for the research under UHV and very detailed and sophisticated measurements can be performed e.g. as described in the doctoral thesis of Kai Roßnagel [102].

- **InAs, ZnSe, ZnTe** (110)-face: These surfaces on materials with zinc-blende crystal structure are prepared by mechanical cleaving as shown in Fig. 3.1. Here very often the resulting surface is not perfect, but has steps and roughness. In such a situation the cleave must be repeated. The sample must be specially prepared (cut along the proper crystallographic direction) to allow a successful cleave. (110) surfaces of zinc-blende crystals are not as passive as these of layered crystals and therefore one should maintain the pressures below $5 \cdot 10^{-10}$ mbar on the course of measurements. Most of the (110) surfaces of the important semiconductors were measured in great details about 10 - 20 years ago and nowadays they serve as well-defined substrates for the more sophisticated studies on adsorbates [121] and interfaces.

- **ZnSe** (001)-face: Here a special care must be taken before the actual preparation in the experimental chambers. The (001) face is highly reactive and therefore the sample should never leave UHV conditions. Typically samples are grown in specialized systems at different location than they are measured and therefore a special UHV transfer system should be developed. Well-defined surfaces are prepared by annealing at the appropriate temperature to produce the desired reconstruction[3]. Sometimes it is additionally necessary to slightly sputter the sample especially if the vacuum conditions during the transfers were not adequate. In the best case after all the efforts with UHV transfer a sample can be ready for measurements 24 hours after loading to the experimental chambers.

- **GaN** (0001)-faces: These are the most difficult surfaces to prepare. Often the same preparation procedure leads to a surface that gives slightly different results in photoemission. Subsequent cycles of sputtering and annealing wear-out the sample with the danger of destroying thin-film samples. The main reason for these problems is that the samples are typically grown under high pressures and then exposed to

---

[3] The details about the preparation of the ZnSe(001) surface are given in the experimental part of this thesis.

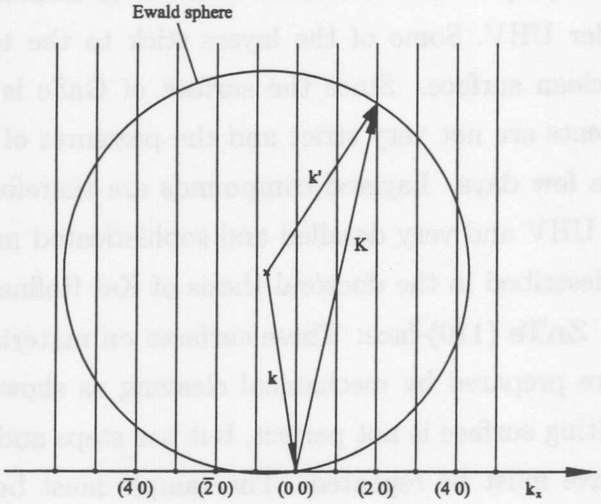

Figure 3.3: Ewald construction for the case of elastic electron scattering at a $2D$ surface. The surface reciprocal lattice points are plotted along k_x. A reflection is observed when the Laue condition (3.2) is fulfilled.

air so the surfaces are always oxidized[4].

3.2 Low energy electron diffraction

Low energy electron diffraction (LEED) is the most popular technique for evaluating the cleanness and crystallographic quality of freshly prepared surfaces.

3.2.1 Theory

It is intuitive to treat LEED as scattering. The diffraction pattern on a fluorescent screen is created by elastically backscattered electrons. The general Laue condition for elastic scattering tells us that the difference **K** between wave vectors of the incoming and scattered waves **k** and **k**′

$$\mathbf{K} = \mathbf{k}' - \mathbf{k} \tag{3.1}$$

is a vector of the reciprocal lattice. For the case of surface scattering with the additional assumption that only the topmost layer takes part in scattering the parallel component of the scattering vector is equal to the $2D$ surface reciprocal lattice

---

[4] This is true for the samples measured in this thesis. However, GaN can be grown also by MBE and in this case the UHV conditions could be maintained at all stages.

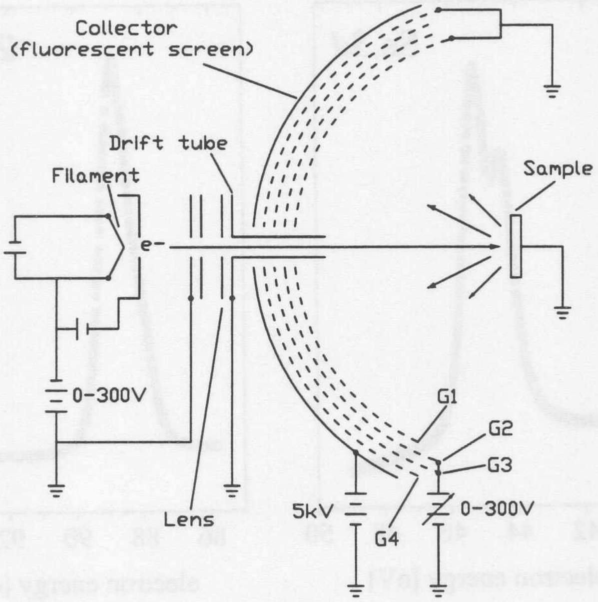

Figure 3.4: Scheme of the four-grid LEED system used at the Winkelemi experimental station at HASYLAB.

vector $\mathbf{G}_{surf}$

$$\mathbf{K}_{\|} = \mathbf{k'}_{\|} - \mathbf{k}_{\|} = \mathbf{G}_{surf} \tag{3.2}$$

Angle values for which the Bragg spots appear can be found from the Ewald sphere construction shown in Fig. 3.3.

3.2.2 LEED setup

LEED experimental setup is presented in Fig. 3.4. It consists of an electron gun with focusing lenses and display-type hemispherical electron detector with 4 grids. Electrons are emitted from a filament cathode and are accelerated towards the sample through the focusing lenses and a grounded drift tube. The energy of the incident electrons is usually varied between 30 and 200 eV. Electrons in this energy range have a very short mean free path inside the crystal which makes the experiment very surface sensitive. Grid G1 and sample are grounded to establish a field-free space between the sample and display system [84]. The backscattered electrons contain inelastic and elastic parts. The inelastic electrons have lower energy and can be

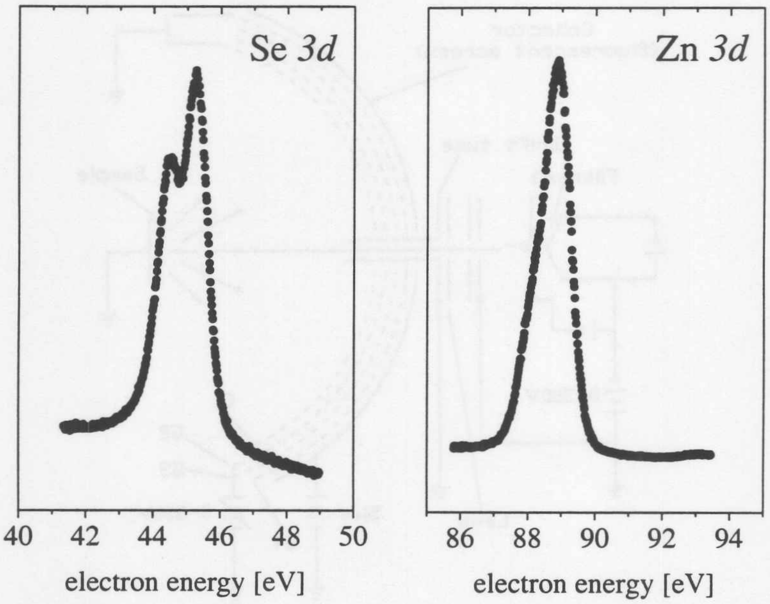

Figure 3.5: The angle-integrated spectra of from ZnSe(001) surface taken at E_{ph} = 100 eV. The ordinate values are in arbitrary units. No background is subtracted.

suppressed by the G2 and G3 voltage[5]. The elastic part passes all 4 grids and is accelerated towards the screen. The fluorescent screen is at a high potential of 5 kV with respect to the grounded G4 because only high energy electrons can create visible spots on the fluorescent screen.

3.3 Core-level photoemission

As already mentioned in section 2.3 the photoemission spectrum contains information about the valence band, core levels and a scattered electron tail. In the investigation of molecules and solids one is usually interested in the change in binding energy between two different chemical forms of the same atom. This energy difference is called the chemical shift[6]. Measurements of chemical shifts can provide the information about the reconstruction or impurities on the surface since VUV photoemission is a surface sensitive technique.

In Fig. 2.9 one can see a sharp peak related to the emission from the Zn 3d

---

[5] In general only 3 grids are necessary for a LEED experiment. However, 4 grid system allow to use such LEED apparatus as a retarding grid analyzer for example for Auger electron spectroscopy.

[6] Note that the shift may be due to the different chemical bonding of the bulk surface atoms.

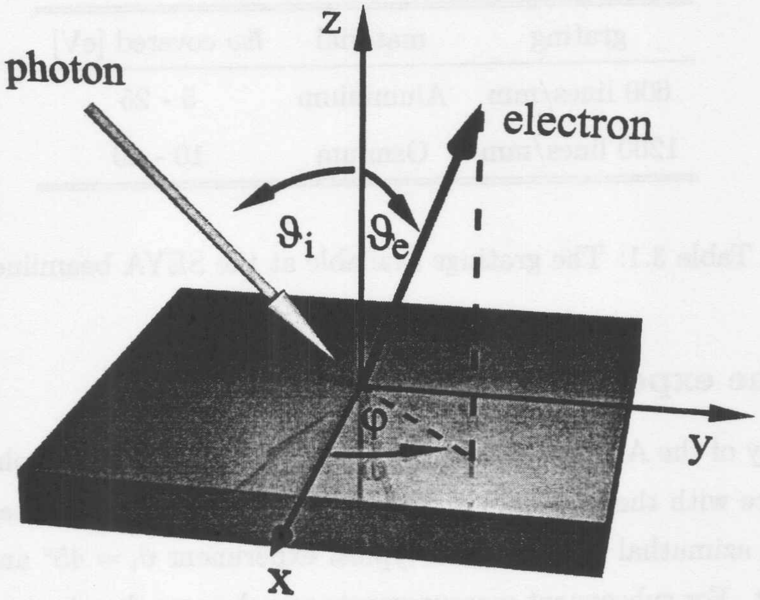

Figure 3.6: Geometry of the typical angle-resolved experiment and with the various relevant angles indicated.

semicore states. The binding energies of Se $3d_{3/2}$ and $3d_{5/2}$ core levels are 55.5 and 54.6 eV respectively (the splitting is due to spin-orbit coupling). To reach those levels in photoemission one has to use photon energies higher than 60 - 70 eV. In Fig. 3.5 an angle-integrated photoemission measurements of both Zn and Se 3d levels at E_{ph} = 100 eV are presented. The spectra were collected at beamline E1 at HASYLAB equipped with the Flipper monochromator and cylindrical-mirror angle-integrating electron energy analyser [122].

3.4 Angle-resolved photoemission

Angle-resolved photoemission (ARPES) is the most powerful technique for mapping the dispersion of the occupied electronic states of semiconductors. To obtain k-resolution in reciprocal space one has to perform photoemission measurements with angular resolution. In the ideal case a spectrometer with good angular resolution is combined with a tunable light source that enables mapping the band structure in the whole Brillouin zone.

grating	material	$\hbar\omega$ covered [eV]
600 lines/mm	Aluminium	5 - 25
1200 lines/mm	Osmium	10 - 40

Table 3.1: The gratings available at the SEYA beamline.

3.4.1 The experimental setup

The geometry of the ARPES experiment is shown in Fig. 3.6. The photon impinges on the surface with the incidence angle ϑ_i and the electron is emitted at the polar angle ϑ_e and azimuthal angle φ. In a typical experiment $\vartheta_i = 45°$ and $\varphi = 90°$ are kept constant. For subsequent measurements one changes the photon energy (when using tunable light source) and polar angle ϑ_e. Typically normal emission ($\vartheta_e = 0°$) spectra are measured first for all accessible photon energies. These measurements can usually give a reference of how to proceed with the subsequent angle resolved scans. Azimuthal angle φ is changed when one is interested in polarization effects. Changing the photon incident angle ϑ_i may result in increased/decreased surface sensitivity.

3.4.2 Apparatus at Winkelemi

The main experimental results discussed in this thesis were measured at the F.2.2 beamline at HASYLAB. This beamline is equipped with a 1m SEYA-NAMIOKA monochromator covering the photon energy range 4 - 40 eV with two gratings [123, 124]. The monochromator is a modified UHV version of the Minuteman model 310 SN. The dispersion plane of the instrument is turned 90° with respect to the standard orientation in order to enhance the linear polarization of the beam and to match the source (4×1.6 mm^2) to the entrance slit (16×0.1 mm^2). The instrument mechanically covers wavelength range from central image (zero order) to 6000 Å with a 600 lines/mm grating installed. A grating exchange mechanism that allows gratings to be changed under UHV gives the possibility to extend the photon energy range of the instrument by using gratings with different blaze angles and coatings (see Table 3.1).

The slit widths of the entrance and exit slit are continuously adjustable from

device	application
	Analyzer chamber
ADES 400 spectrometer	main angle-resolved electron-energy spectrometer
LEED system	inspection of the surface quality, sample orientiation
	Preparation chamber
MBE cell	evaporation of adsorbates on the surface
Quartz balance	thickness monitor
Cleaving tool	preparation of the clean surfaces
Ar-ion gun	surface preparation/cleaning
CMA spectrometer with integrated electron-gun	Auger electron spectroscopy
	Load-lock system
Magazine	storage of up to 4 samples under UHV
Baby-chamber	transfer of the samples under UHV from Würzburg to Hamburg

Table 3.2: The equipment of the SEYA F.2.2 beamline at HASYLAB.

10 μm to 1 mm. A stepping motor is connected to the sine drive of the gratings by a threaded rod that moves a precision ball screw at the end of the feedthrough arm of the grating holder. The linear displacement of the sine drive which is proportional to the wavelength is measured using an optical encoder. Surface contamination of the mirrors and gratings can be avoided by maintaining UHV conditions, free of hydrocarbons, in the main beam pipe system, the mirror chambers and the monochromator. Pressures below $1 \cdot 10^{-9}$ mbar are kept in the monochromator and the beampipe and down to $3 \cdot 10^{-11}$ mbar in the spectrometer chamber.

The photoelectron spectrometer is a Vacuum Generators ADES 400 model in which the energy analyzer can be rotated independently in both angles around the specimen. The electron analyzer is a 150° spherical sector analyzer with a 50 mm mean radius. The distance to the sample is 23 mm, a typical angular resolution is below 2°. Depending on the pass energy which can be selected between 2 and 200 eV the resolution varies between $\Delta E = 0.04$ eV and 4.0 eV. Analyzer chamber is additionaly equipped with a LEED system allowing determination of the crystallographic directions of the sample. It is also possible to use a He-resonance lamp, however, it is not installed at present.

There is a separate preparation chamber at the beamline and a special UHV transfer system between the chambers. The preparation chamber is equipped with a MBE cell for thin films evaporation, quartz oscillator for the thickness monitoring, Ar-ion gun and cylindrical mirror (double-pass) electron energy analyzer with an integrated electron gun for an Auger-electron measurements. Manipulators of both chambers allow to anneal the samples up to temperatures of 500°C by passing current through the heating wire close to the sample. Higher temperatures can be available in special cases, e.g. by passing current through the sample or by e-beam heating.

Recently we have developed a special transfer system allowing for the transport of samples from Würzburg to Hamburg under UHV conditions. Our standard sample holder was adapted to the inlay used at the MBE system at Würzburg and a special *baby* chamber equipped with the ion pump that can be powered using a battery was built.

Chapter 4

Electronic structure of GaN(0001) and (000$\bar{1}$) surfaces

Gallium nitride has aroused considerable interest over the past decade due to the progress in crystal growth which opened up the possibility for its use in optoelectronic applications. The goal was to fabricate high performance blue laser diodes. There were enormous efforts put to characterize its physical properties aiming in designing the blue laser diodes for massive industrial production. The physical properties and mechanical strength of GaN make it more attractive than other wide band-gap semiconductors since it prevents the damage of the light emitting device allowing longer life-times. However, the surface and interface structure of the GaN is still not understood in details.

Two different forms of GaN samples with the wurtzite crystal structure are available: single crystals grown under high pressure and thin films grown using either metal-organic chemical-vapour deposition (MOCVD), metal-organic vapor-phase epitaxy (MOVPE) or molecular beam epitaxy (MBE) techniques.

The band structures of GaN calculated using different methods are presented in Figs. 2.4 and 4.1(a). The schematic view of wurtzite crystal lattice and corresponding Brillouin zone are presented in Figs. 4.1(b) and 4.2. The DFT-GGA calculation presented in Fig. 4.1 reproduces the results published by Vogel *et al.* [76] with high accuracy. At the Γ point for the band $\boxed{4}$ Vogel *et al.* reports −7.1 eV whereas our result is −6.9 eV so the difference is 0.2 eV. The calculations from [72] presented in Fig. 2.4 are based on external parameter sets. The parameter set used was adjusted to the *ab initio* calculations of Vogel *et al.* [76].

The large ionicity of GaN results in the antisymmetric gap of more than 5 eV.

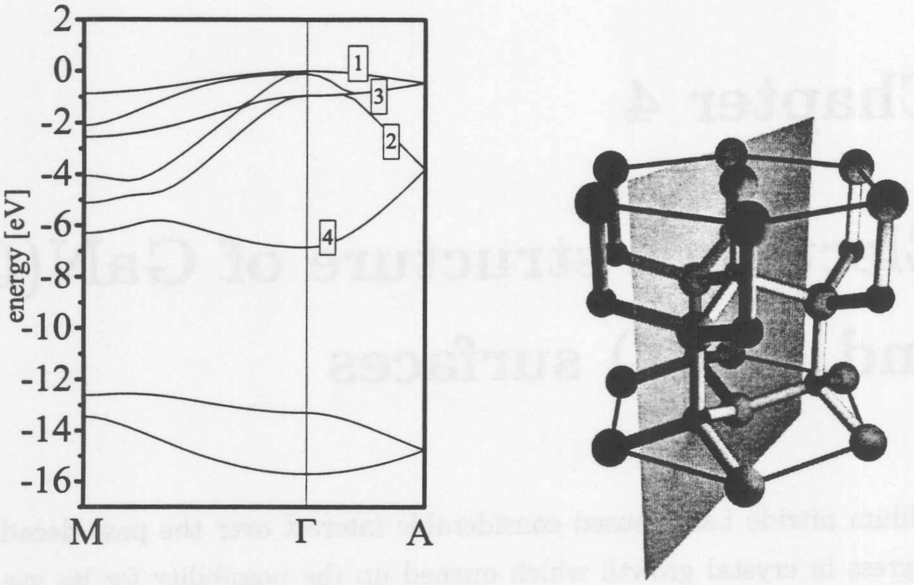

(a) (b)

Figure 4.1: (a) Band structure for bulk GaN calculated with the *fhi98md* code. No 3*d* electrons were included in the Ga pseudopotential but the Becke-Perdew [43, 49] exchange-correlation functional was used. The *k*-resolved charge densities of the bands labeled $\boxed{1}$, $\boxed{2}$, $\boxed{3}$ and $\boxed{4}$ are shown in Fig. 4.3 (b) wurtzite crystal lattice with the plane indicated that was used to create charge densities shown in Fig. 4.3.

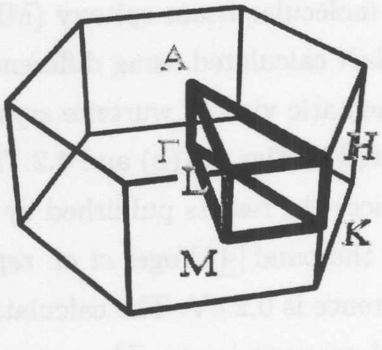

Figure 4.2: Brillouin zone for crystals with wurtzite structure.

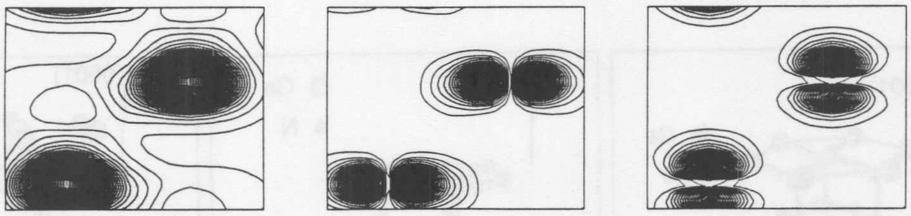

(a) Total density (b) Γ band $\boxed{1}$ (c) Γ band $\boxed{3}$

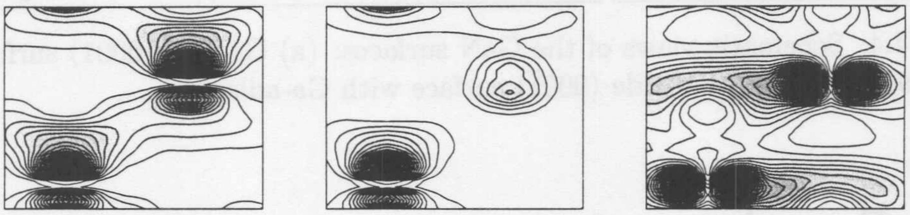

(d) Γ band $\boxed{4}$ (e) A band $\boxed{2}$ (f) M band $\boxed{4}$

Figure 4.3: Contour plots for bulk wurtzite GaN. Partial densities at different BZ critical points for different valence bands are presented. The plane used and the nomenclature of the bands is shown in Fig. 4.1. The darker shade of gray corresponds to higher intensity, each subfigure has been normalized separately.

Charge densities calculated using *fhi98md* code presented in Fig 4.3 indicate charge transfer to the nitrogen atoms.

The surfaces perpendicular to the *c*-axis of the hexagonal lattice of the wurtzite crystals are polar. For GaN the notation is (0001) for Ga-side and $(000\bar{1})$ for N-side. Schematic views of the two surfaces are presented in Fig. 4.4 (a) and (b). After first STM experiments performed on GaN $(000\bar{1})$ surfaces Smith *et al.* [125] proposed the Ga-adlayer model for this N-polar surface. The schematics of this model is presented in Fig. 4.4(c). STM revealed a variety of different reconstructions on (0001) and $(000\bar{1})$ surfaces. Here the comparative results on single crystal samples and thin films grown by MOVPE are presented [126]. The goal of this work was to analyze the surface electronic structure of the two polar surfaces and verify the theoretical models proposed by Smith *et al.* [125, 127].

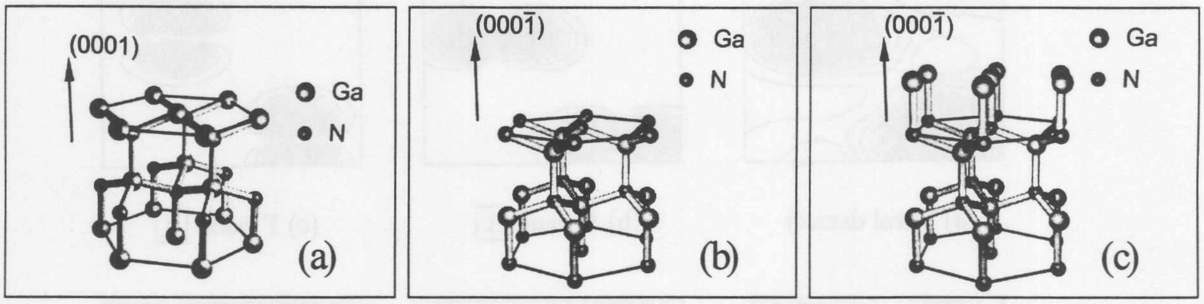

Figure 4.4: Schematic views of the GaN surfaces: (a) Ga-side (0001) surface, (b) N-side (000$\bar{1}$) surface and (c) N-side (000$\bar{1}$) surface with Ga-adlayer.

4.1 Experimental

The single crystal GaN samples were made at the High Pressure Research Center UNIPRESS in Warsaw, Poland [2]. They are very thin platelets (around 0.2 mm thick, 4 × 4 mm^2 area) and the pre-prepared surface (electrochemically polished) normal to the large face is along the [000$\bar{1}$] crystallographic direction. Single crystal GaN samples made under high pressure from pure gallium solution are highly conducting with electron concentrations of 3 - 6 × 10^{19} cm^{-3} and mobilities of 30 - 90 $\mathrm{cm}^2/\mathrm{Vs}$ [128].

The thin film sample was 2 μm GaN layer grown on a (0001)-oriented sapphire substrate using an atmospheric pressure MOVPE growth process at Bremen University, Germany [129]. It was nominally undoped but had n-type carrier concentrations of 2 × 10^{17} cm^{-3} and a mobility of 200 $\mathrm{cm}^2/\mathrm{Vs}$ at room temperature. The surface normal was along [0001] direction. The most likely defects in this sample were threading dislocations due to the difference between lattice constants of sapphire and GaN.

Exactly the same cleaning procedure was used for both types of samples: prolonged outgassing at 450 - 500°C, then Ar^+ ion sputtering at 0.5 kV, 25 mA for 30 min followed by annealing. This procedure applied to the single crystal samples has been shown [128] to produce a clean but Ga-*rich* (000$\bar{1}$) surface. Fig. 4.5 shows the Ga 3*d* level and valence band at different stages of surface preparation. The contribution to the Ga 3*d* from metallic Ga slowly diminishes with prolonged annealing,

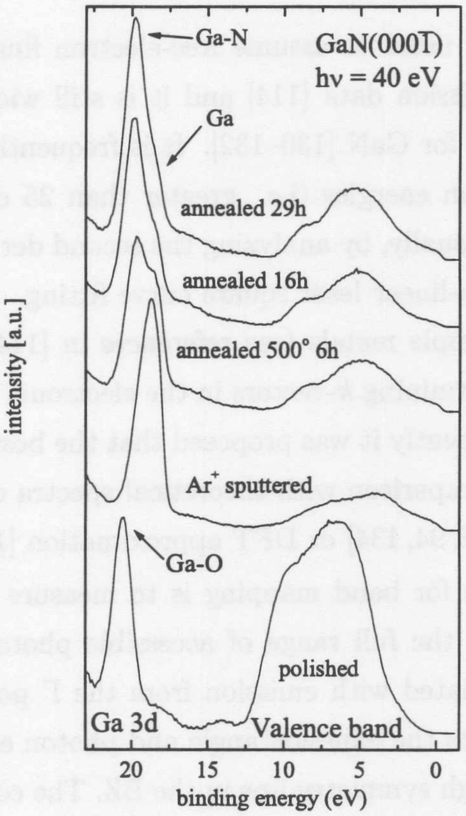

Figure 4.5: The angle-integrated photoemission spectra from a GaN single crystal (000$\bar{1}$) surface. The relative intensities in the Ga 3*d* level reveal chemical shifts due to oxygen, pure Ga and GaN (figure courtesy of B.J. Kowalski).

however, it is still present even after 29 hours of annealing[1].

After the cleaning procedure LEED revealed a 1×1 pattern with extremely sharp reflections. No surface reconstruction and no charging effects were apparent despite the fact that the samples were nominally undoped. The excellent LEED patterns proved that the crystallinity of the samples was very good and that they were adequate for band structure measurements. All measurements were carried out in room temperature.

---

[1] Note that even after very long annealing the fresh Ga-*rich* surface may be easily recovered with the help of sputtering.

4.2 Results

In the past it has been usual to assume free-electron final states when analyzing angle-resolved photoemission data [114] and it is still widely used in determining Brillouin zone k vectors for GaN [130–132]. It is frequently stated that this is justifiable for higher photon energies (i.e. greater than 25 eV) [114, 131, 133]. Peak positions are assigned visually, by analyzing the second derivative of the photoemission spectrum or by non-linear least square curve fitting. Although this procedure is very successful for simple metals (see references in [114]) it very often leads to significant errors in determining k-vectors in the electronic band structure of binary semiconductors [94]. Recently it was proposed that the best way to analyze photoemission spectra is by comparison with theoretical spectra obtained within one-step photoemission model [72, 94, 134] or DFT approximation [118].

The usual procedure for band mapping is to measure normal emission energy distribution curves over the full range of accessible photon energies. From these data the shoulder associated with emission from the Γ point can be located. For subsequent measurements the emission angle and photon energy are then varied so as to map the desired high symmetry line in the BZ. The correct sample orientation is determined from the LEED pattern.

4.2.1 Normal emission

Figure 4.6 shows a series of normal emission EDCs for single crystal and thin film samples recorded for photon energies 13 - 25 eV. Each curve was fitted with a set of Gaussians. Solid lines indicate the positions of the peaks which match the theoretical band structure calculation, however, there are more features in the spectra in certain regions. Transitions to different final states make the fitting procedure uncertain so we did not consider such features when constructing the band structure. For photon energies below 17 eV Ga MVV Auger transitions are visible. We found the $k_\perp$ values corresponding to the identified features with the help of the calculated final bands shown in Fig. 4.7. Only two final bands were used: a and c. In Fig. 4.8 circles indicate transition to the a final band and + symbols to the c final band. Squares and × symbols denote different non-dispersing features.

We located the Γ point for the valence band maximum at 16 eV photon energy. This fits very well with the theoretical calculation, however, we find that the width

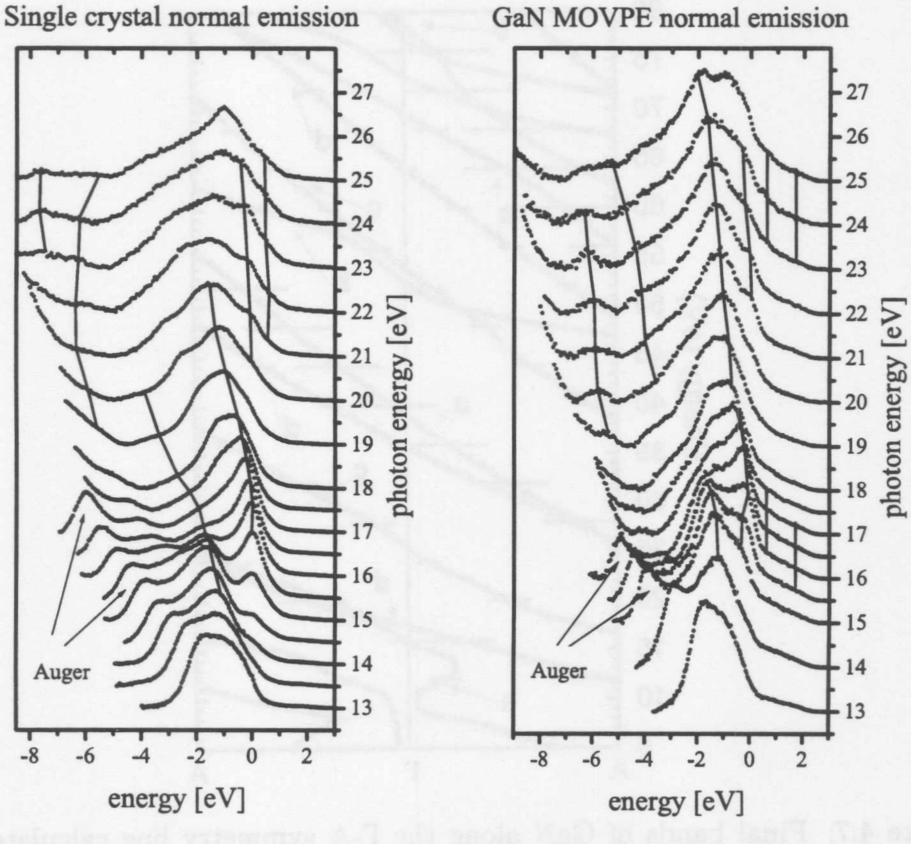

Figure 4.6: Representative sets of normal emission EDCs for single crystal and thin film GaN. Binding energies are refered to the VBM.

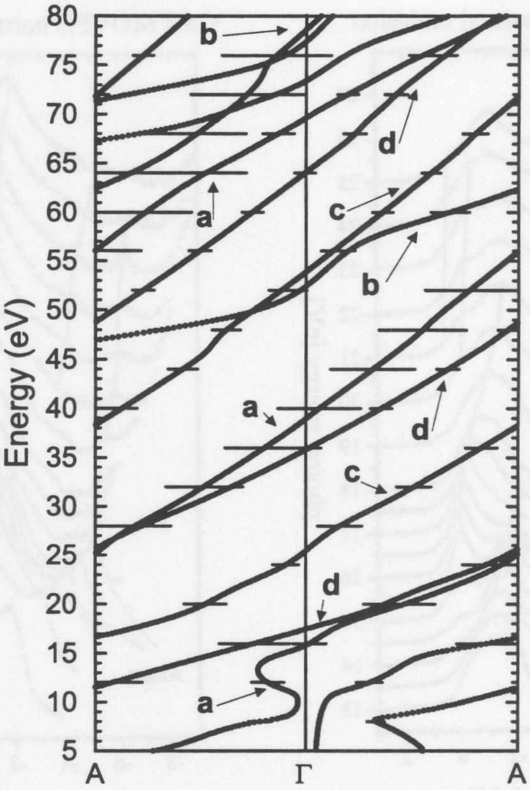

Figure 4.7: Final bands of GaN along the Γ-A symmetry line calculated by Strasser *et al.* [72]. Horizontal bars identify the bands which contribute to the photoemission process and stress their significance.

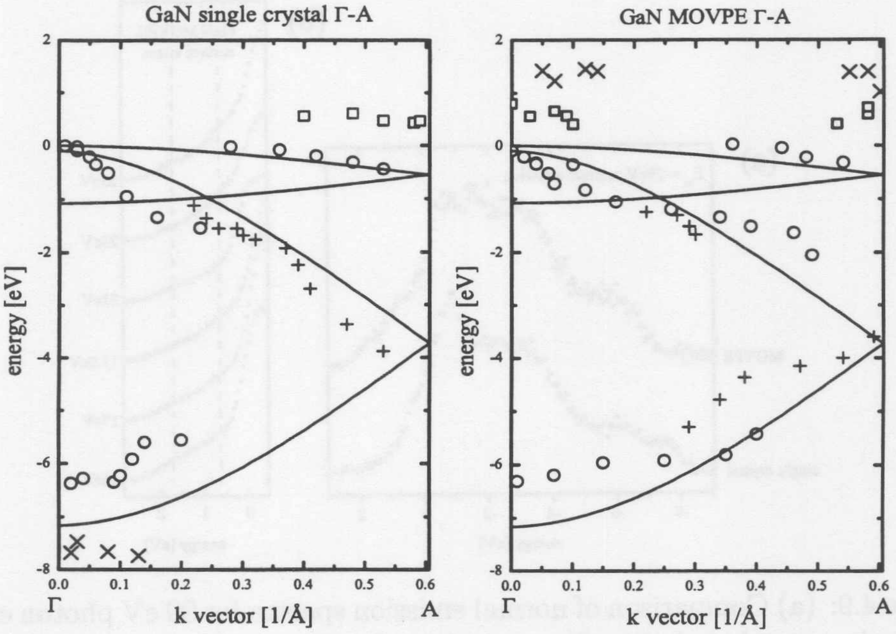

Figure 4.8: Band structure of GaN in the Γ-A direction. Solid lines show the calculated band structure from [72].

of the valence band is around 0.5 eV narrower than calculated by Strasser *et al.* [72]. Both samples show the same bulk features and the energy differences are less than 0.5 eV. The clear shoulder at the top of the valence band for $\hbar\omega = 15$ - 17 eV provides a reference point and for convenience we denote this energy as the VBM and reference the energy scale to this point. The more usual procedure would be to extrapolate the leading edge of the spectra, however, in the presence of surface states within the fundamental gap this method is unreliable.

We find one surface state in the band gap for the single crystal and two for the thin film sample. The features indicated with squares in Fig. 4.8 are the same for both samples and are located approximately 0.5 eV above the VBM. The feature indicated by × is observed only in thin films and is located approximately 1.5 eV above the top of the valence band[2]. For a single crystal sample we have also identified a non-dispersive feature at approximately -7.5 eV energy. This feature was observed by Dhesi *et. al.* [130] at -8 eV binding energy where it was interpreted as a probable indirect transition from the bottom of the valence band (density-of-states effect),

---

[2] k vectors for the squares and × symbols arise from excitation to the a final state - it should be noted that $k_\perp$ is undefined for a surface state; points above VBM in Fig. 4.8 for the thin film sample were found using a Gaussian fit - they are marked by vertical lines in Fig. 4.6 for clarity

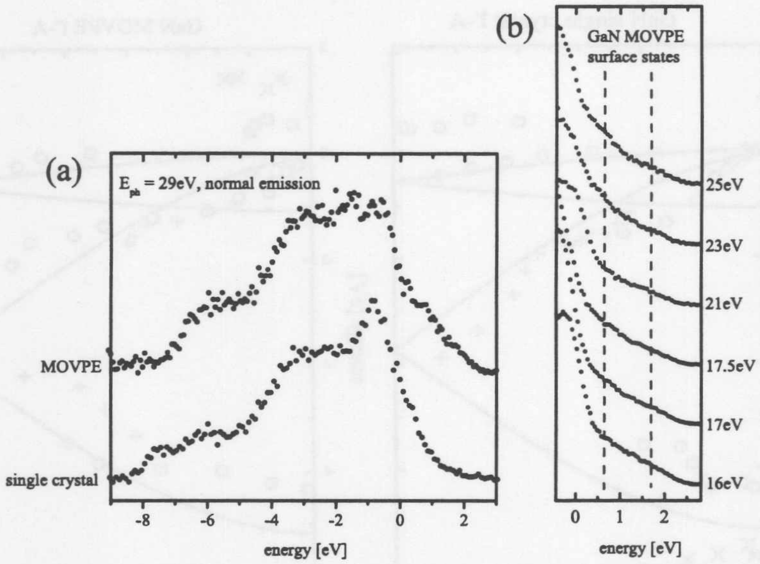

Figure 4.9: (a) Comparison of normal emission spectra for 29 eV photon energy for single crystal and thin film samples. (b) Magnified region showing the double peak surface structure above the VBM for thin film sample at selected photon energies.

however, our explanation for this feature is emission from Ga 4*s* surface state [72]. For our data this cannot be a transition from the bottom of the valence band because the valence band is too narrow.

In Fig. 4.9(a) normal emission spectra for both samples for the higher photon energy of 29 eV are presented. It is immediately apparent that both spectra have similar bulk features but there are significant differences in the surface features. As in the 13 - 25 eV photon energy range we find that for the MOVPE sample the surface feature at the bottom of the valence band is missing. Since for the (000$\bar{1}$) surface this peak arises from Ga 4s orbitals from the first atomic layer [72] it confirms the Ga-adlayer model for the single crystal sample. However, further off-normal emission results presented in the Subsection 4.2.2 do not fully agree with the Ga-adlayer model.

The MOVPE thin film sample has a much higher photocurrent above the top of the valence band. A magnified view of these regions for selected photon energies is presented in Fig. 4.9(b). The lack of the surface state at the valence band bottom and the two surface peaks above the VBM indicate that the MOVPE sample has a different, as yet undetermined Ga-termination[3]. The termination may be similar to the discommensuration-fluid phase proposed in Refs. [127, 135] for the room temperature Ga-rich GaN (0001) surface.

4.2.2 Off-normal emission

In Fig. 4.10 off-normal emission data for thin film sample is presented. A significant photocurrent over the VBM for all angles suggest a metallic nature of this surface. This is similar to the angle-resolved photoemission results of Maruyama *et al.* [136][4] on similar surface but with higher photon energies. The result presented here partly agree with the latest theoretical results from Prof. Pollman's group [69, 137] since they predict similar width of the surface band within the fundamental gap for the Ga-adlayer (0001) surface. However, they predict only one surface band in the gap and from our measurements we can see two or more bands there. It should be noted that the calculations presented in reference [69] consider only one Ga-adlayer on (0001) surface whereas Northrup *et al.* [135] predicted a more complex bilayer termination based on STM results.

In Fig. 4.11 a series of off-normal EDCs along the Γ-M direction from the GaN single crystal sample is presented. The band structure presented in Fig. 4.12 was created using free-electron parabola final states with an inner potential $V_0 = 10$ eV in agreement with the work of Dhesi *et al.* [130]. The experimental points indicating bulk states are also plotted in Fig. 4.13 to show their location in the bulk Brillouin zone[5]. Most of the points are located very close to the high symmetry Γ-M line because the emission angles and photon energies were carefully selected. However, for some points a deviation as large as 0.1 Å^{-1} in $k_\perp$ is found.

Two surface states have been found in the Γ-M data for the single crystal sample and are indicated in Fig. 4.12 by crossed squares and circles. The theoretical band structure by Strasser *et al.* [72] for the Ga-rich surface presented in Fig. 2.6 does not reproduce any of the experimental surface bands. The uppermost band fits very well to the calculation of Wang *et al.* [69], but for the clean relaxed (000$\bar{1}$) surface (not Ga-rich). The feature at around −7.5 eV energy cannot be seen in Refs. [69, 72, 137]

---

[3] Note that the paper of Strasser *et al.* [72] gives no information about the (0001) surface.

[4] Maruyama *et al.* [136] did not discuss this feature in detail, however, it is apparent on the published experimental spectra.

[5] The free-electron final state scheme allows to locate every feature from the given EDC within the three dimensional Brilloin zone. However, in real-world final state is not always close to the free-electron and in general such assignment may not be possible.

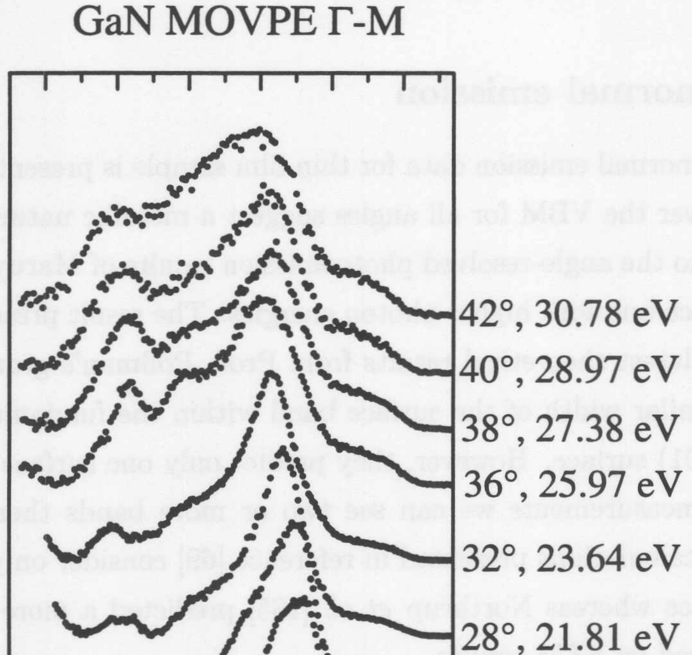

Figure 4.10: Off normal emission data for MOVPE sample along Γ-M direction in Brillouin zone.

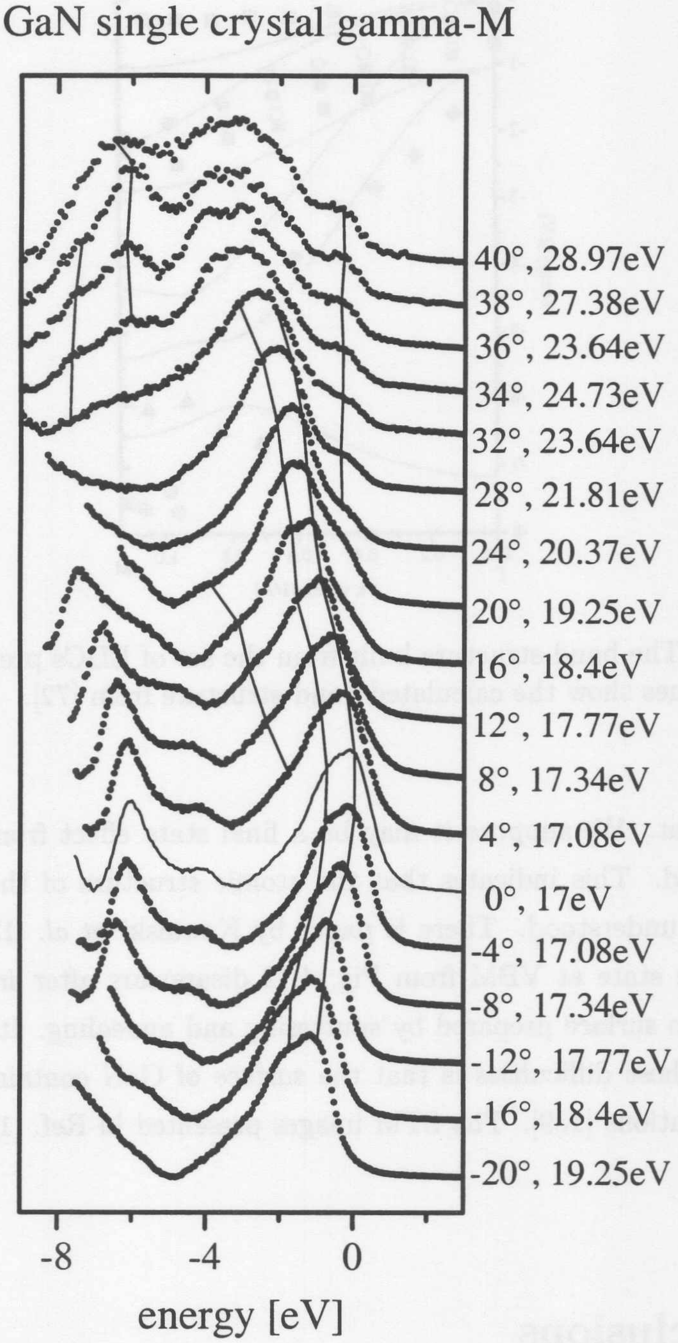

Figure 4.11: Off normal EDCs along the Γ-M direction for single crystal sample. Guide lines indicate the points taken into account for building the band structure. Energy scale refers to VBM.

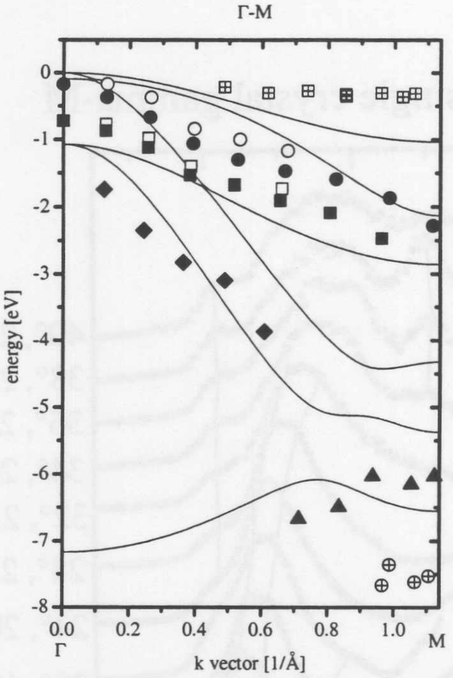

Figure 4.12: The band structure built from the set of EDCs presented in Fig. 4.11. Solid lines show the calculated band structure from [72].

near the M point. We suppose it may be a final state effect from the bottom of the valence band. This indicates that the atomic structure of the (000$\bar{1}$) surface is still not well understood. There is paper by Kowalski *et al.* [138] which shows that the surface state at VBM from Fig. 4.12 disappears after *in-situ* deposition of the Ga on the surface prepared by sputtering and annealing. It is possible that the reason for these difficulties is that the surface of GaN contains domains with different terminations [139]. The STM images presented in Ref. [125] support this point of view.

4.3 Conclusions

The two different polar surfaces of GaN were investigated using angle-resolved photoemission with synchrotron radiation and new surface features were found. The results confirm the opinion that the surface of the GaN is currently not yet understood in detail. There is no clear correspondence between the calculated and

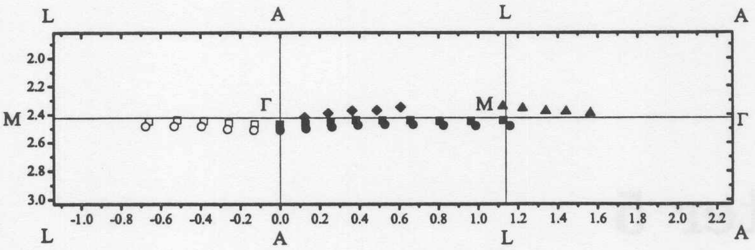

Figure 4.13: The position of points from Fig. 4.12 in the bulk Brillouin zone. The corresponding symbols are used to indicate the respective bands.

measured surface band structures. Since the bulk structure is reproduced reasonably well, it is obvious that the surfaces investigated so far are far from the ideal. In the case of the single crystal sample this comes from the surface roughness. The surfaces are prepared by mechanical-chemical polishing, however, the imperfections are also a big problem for homoepitaxy[6]. The high level of dislocations in GaN samples may also contributed. As pointed out by Dhesi *et al.* [130], if the defects associated with the dislocation centers were recombination centers it is very unlikely that GaN-based devices would function. Since they do, it implies that such centers are passive. The additional random scattering at the surface is probably the reason why the bulk features appear rather broad in the spectra.

The interesting double surface feature observed above the VBM for the thin film sample would probably be very difficult to reproduce theoretically. Since such a structure was also observed in [136] it looks as if the surface on Ga-polar (0001) face is metallic with very likely a double- or triple-layer termination in a discommensuration-fluid phase that would be difficult to simulate using e.g. DFT methods. However, one should probably start with some simpler model to determine origin of these peaks.

---

[6] On the website http://www.consult.topgan.fr.pl/pr_index.htm one can find more details on this subject.

Chapter 5

Electronic and geometrical properties of ZnSe(001)

This chapter is dedicated to bulk ZnSe and the ZnSe(001) surface. Extensive theoretical *ab initio* studies of the geometry and the electronic structure are presented and verified by photoemission measurements. In the first section the sample preparation techniques are presented and the necessity of transferring of the samples under UHV directly from the growth chamber is stressed. The following two sections are dedicated to the bulk and c(2×2) reconstructed surface respectively. The limitations of the free-electron final state model in case of ZnSe(001) are described in the section concerning the bulk. The electronic bands are also analyzed in detail with the help of *ab initio* calculations. In the surface section calculations on the surface electronic structure of ZnSe(001)-c(2×2) are presented and verified by the angle-resolved photoemission measurements.

5.1 Sample preparation

The ZnSe(001) thin film samples were grown on GaAs substrates using MBE at Würzburg University. There is a complex system of MBE chambers at the Institut für Experimentalphysik in Würzburg where II-IV materials of the highest quality can be grown.

We measured several thin film samples with thicknesses of 50 - 100 nm. All samples were pseudomorphically strained with respect to the GaAs lattice constant since the critical thickness for this system is around 150 nm [140]. A lattice constant

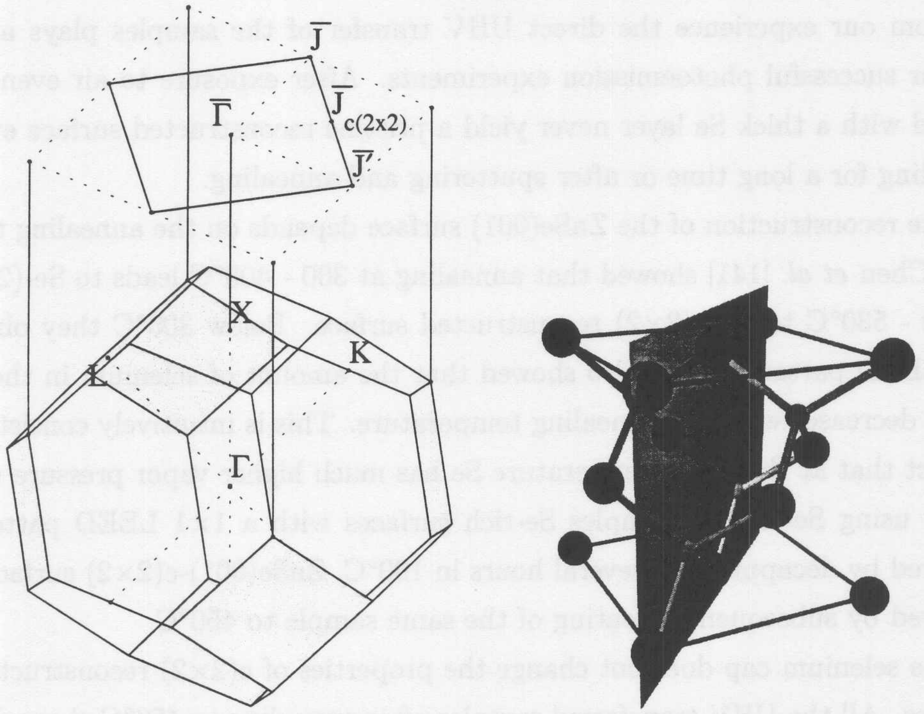

Figure 5.1: Left: the BZ for the fcc lattice and the surface BZ for the c(2×2) reconstruction on the (001) surface. The high symmetry directions are indicated and the nomenclature of the c(2×2) surface BZ high symmetry points is such that $\bar{\mathrm{J}}$ and $\bar{\mathrm{J}}'$ use 1×1 surface BZ nomenclature and $\bar{\mathrm{J}}_{c(2\times2)}$ uses c(2×2) surface BZ nomenclature. Right: zinc-blende crystal lattice; the shaded plane shown is used to create a charge densities in Fig. 5.3.

mismatch of 0.27% between GaAs and ZnSe should have little effect on the shape of the band structure and unrelaxed samples have the advantage that the number of dislocations is reduced.

Freshly prepared samples with and without Se passivation were transferred under ultra-high vacuum conditions directly from the MBE machine in Würzburg to the photoemission beamline in Hamburg. The pressure was below $5 \cdot 10^{-9}$ mbar at all times to avoid the possibility of surface contamination.

From our experience the direct UHV transfer of the samples plays a decisive role for successful photoemission experiments. After exposure to air even samples capped with a thick Se layer never yield a pristine reconstructed surface even after annealing for a long time or after sputtering and annealing.

The reconstruction of the ZnSe(001) surface depends on the annealing temperature. Chen *et al.* [141] showed that annealing at 300 - 400°C leads to Se-(2×1) and at 400 - 530°C to Zn-c(2×2) reconstructed surface. Below 300°C they observed a 1×1 LEED pattern. They also showed that the amount of selenium in the surface region decreases with the annealing temperature. This is intuitively consistent with the fact that at the same temperature Se has much higher vapor pressure than Zn.

By using Se-capped samples Se-rich surfaces with a 1×1 LEED pattern were prepared by decapping for several hours in 100°C. ZnSe(001)-c(2×2) surfaces[1] were prepared by subsequently heating of the same sample to 450°C.

The selenium cap does not change the properties of c(2×2) reconstructed (001) surfaces. All the UHV-transferred samples after annealing to 450°C showed a sharp c(2×2) LEED pattern and the photoemission spectra from different samples are nearly identical. Also the work function was the same for all of the c(2×2) samples[2].

---

[1] For intermediate annealing temperatures of 300 - 400°C we also always observed 2×1 LEED patterns, however, their qualities were much worse than 1×1 or c(2×2) in case of the samples we measured.

[2] For photoemission the distance between Fermi edge E_{Fermi} and valence band maximum E_{VBM} is important and $E_{Fermi} - E_{VBM}$ does not change from sample to sample on the c(2×2) reconstructed surface.

5.2 Bulk band structure

The bulk band structure was mapped on a ZnSe(001) surface along the Γ-X, Γ-K-X and Γ-L directions. The results are compared with *ab initio* calculations. Three different calculations were used for comparison and the details are collected in the Table 5.1.

Program	Pseudopotentials used	E_{cut}	Lattice constant used
code by A. Fleszar	Zn^{2+}, Se^{6+}	20 Ry	5.67 Å
fhi98md	Zn^{2+}, Se^{6+}	15 Ry	5.59 Å
fhi98md	Zn^{12+}, Se^{6+}	60 Ry	5.82 Å

Table 5.1: Parameters for the theoretical calculations on bulk ZnSe

BZ point	Coordinates	Type
Γ	$\frac{2\pi}{a}(0,0,0)$	bulk
X	$\frac{2\pi}{a}(0,0,1)$	bulk
K	$\frac{2\pi}{a}(1,1,0)$	bulk
L	$\frac{2\pi}{a}(-\frac{1}{2},\frac{1}{2},\frac{1}{2})$	bulk
$\bar{\Gamma}$	$\frac{2\pi}{a}(0,0)$	surface
$\bar{\text{J}}_{c(2\times2)}$	$\frac{2\pi}{a}(1,0)$	surface
$\bar{\text{J}}$	$\frac{2\pi}{a}(\frac{1}{2},\frac{1}{2})$	surface
$\bar{\text{J}}$'	$\frac{2\pi}{a}(\frac{1}{2},-\frac{1}{2})$	surface

Table 5.2: Coordinates of the high symmetry points indicated in Fig. 5.1.

As already shown in Sec. 2.1.3 the different *ab initio* results presented here give similar results. We will not investigate the deep *s*-like band (see Fig. 2.3) so here the term *valence band* is used for the upper part of valence band with energies from around −5 to 0 eV.

Fig. 5.1 shows the relation between bulk and surface Brillouin zones for a (001)

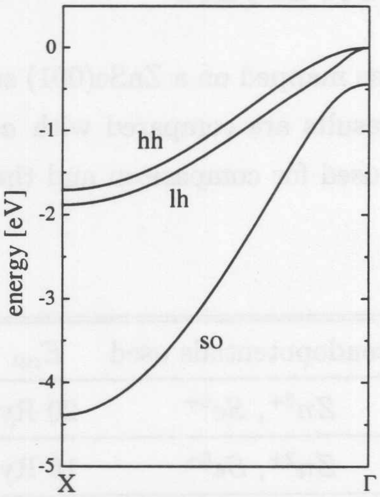

Figure 5.2: Band structure of bulk ZnSe along Γ-X. Bands evolving from the heavy-hole (hh), light-hole (lh) and split-off (so) are indicated. Solid lines show calculation from [81].

surface on the fcc lattice[3]. The coordinates of the indicated high symmetry points are given in Table 5.2. In Fig. 5.2 the nomenclature of the bands for bulk ZnSe is introduced.

Even taking into account the shallow Zn 3d states the antisymmetric gap of ZnSe (see Fig. 2.3) is significant. The charge densities for the bulk ZnSe presented in Fig. 5.3 show that the charge is transferred to the Se atoms, only for split-off band a significant portion of the charge is located near the Zn atoms.

5.2.1 Normal emission

The paper of Niles and Höchst [142] is a good starting point to the analysis of the normal emission spectra from the (001) surface of a II-VI semiconductor. They investigated (001) surface of CdTe using the same type of monochromator and the same photon energy range as in this work. It is clear that 5 - 40 eV energy range provided by the Seya-Namioka design is ideal for the measurements on (001) oriented

---

[3] Please note, that the notations like (001) or (110) originate from the simple cubic lattice cell. Also the lattice constant a_0 is the one from the cubic lattice cell notation. ZnSe has a face-centered cubic lattice (called zinc-blende because this is binary compound) with primitive vectors not equal to those of simple cubic lattice. However, for convenience primitive lattice vectors of the simple cubic lattice are always used and one should keep in mind, that in case of fcc e.g. $(0,0,1)$ and $(1,1,0)$ are not reciprocal lattice vectors and the shortest reciprocal lattice vector is $\mathbf{G} = (1,1,1)$ (we neglect here the factor $2\pi/a_0$). Another reciprocal lattice vector is $(2,0,0)$.

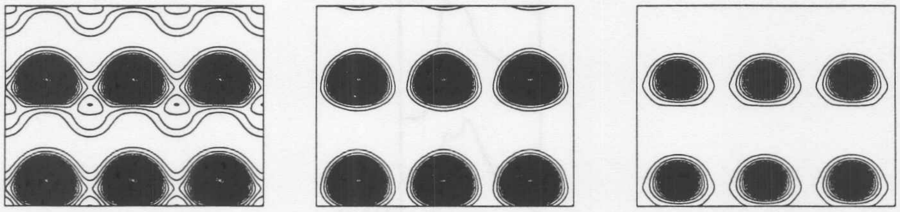

(a) Bulk total (b) Γ VBM (c) Γ *s*-like

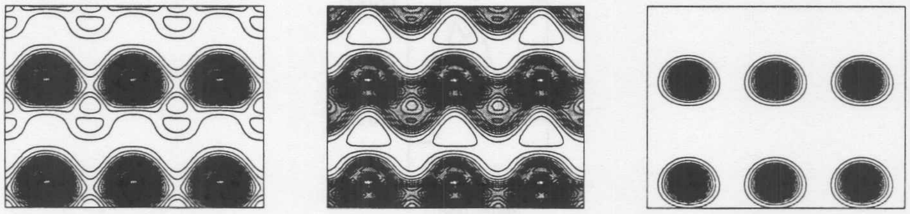

(d) X VBM (e) X split-off (f) X *s*-like

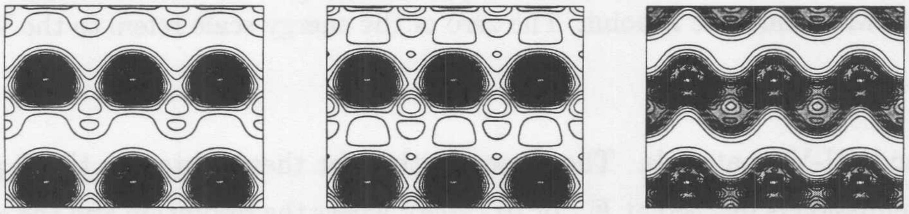

(g) K heavy-hole (h) K light-hole (i) K split-off

Figure 5.3: Contour plots for bulk zinc-blende ZnSe. Partial densities at different BZ critical points for different valence bands are presented. The plane contains *zig-zag* chains of Zn-Se atoms, the abscissa is along (110) and the ordinate along the (001) direction of the cubic cell (this plane is shaded in Fig. 5.1). Intensities of each figure are separately normalized, the darker shade of gray indicates a higher electron density.

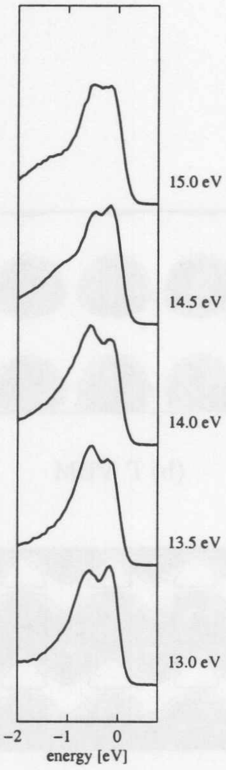

Figure 5.4: Normal emission valence band spectra from ZnSe(001)-(2×2) surface. The spectra were measured at photon energies for the transitions from the VBM around the Γ point. The zero of the energy scale refers to the VBM.

zinc-blende II-VI materials. The reason is that for these materials the Γ point at normal emission is reached at E_{ph} of 10 - 20 eV where the resolution and the counting rate is optimal. One should note, that for example on (110) surfaces of II-VI zinc-blende materials like ZnSe and ZnTe higher photon energies of 20 - 100 eV are preferred [143, 144] and at these photon energies a toroidal grating monochromator yields a higher photon flux.

In the reference [142] transitions from the heavy- and light-hole bands were observed. For ZnSe the splitting of these bands is significantly smaller and is not discernable in our photoemission spectra. The spin orbit splitting at the Γ point is observed and the experimental EDCs for this region are shown in Fig. 5.4. From fitting the features we found a value of 0.40 - 0.45 eV which is in very good agreement with the DFT theoretical value of 0.43 [81].

As shown in Fig. 5.1 normal emission angle-resolved photoemission experiments

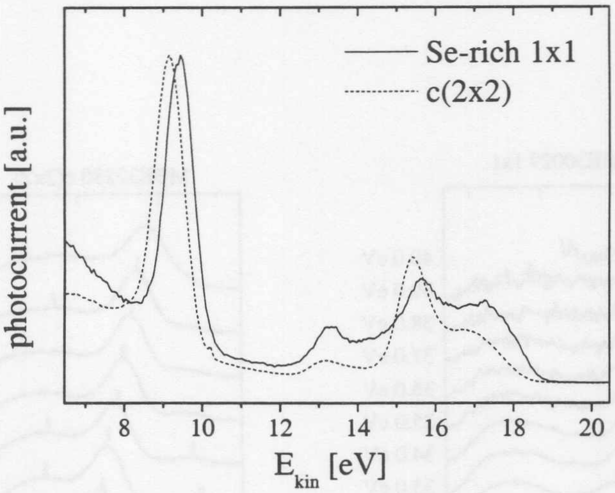

Figure 5.5: The comparison of the normal emission spectra of the 1×1 and c(2×2) reconstructions at $E_{ph} = 25$ eV.

on ZnSe(001) surfaces probes electronic states along the Γ-X (001) direction in Brillouin zone. The sets of normal emission spectra from two different surface reconstructions are presented in Fig. 5.6. The spectra were smoothed using simple running average and positions of the features were found using the inverted second derivative method. The inverted second derivative method is preferred when the spectra are measured with good counting rate because it is parameter-free. For photon energies from 35 to 40 eV the count rate is rather low when working with a Seya-Namioka monochromator. On the Se-rich 1×1 reconstruction these EDCs are not smoothed because for such noisy spectra smoothing may create artificial features. The work function of the Se-rich 1×1 surface is 0.25 eV smaller than of c(2×2) surface which is consistent with the results of Chen *et al.* [141]. The corresponding spectra are shown in Fig. 5.5.

The spectra in Fig. 5.6 are dominated by the transitions from the split-off band. As in the case of CdTe(001) the transitions from the heavy- and light-hole bands decrease in intensity at higher photon energies. Niles and Höchst [142] explained this effect as a consequence of selection rules. They conclude that for the (001) direction only the band with the strongest dispersion has non-zero transition probability if a free-electron-like final band is assumed. This argumentation should also hold for ZnSe(001) since it has exactly the same symmetry[4].

---

[4] Another simple argumentation why the intensity of the heavy- and light-hole bands drops away from the Γ point would be that the density of states is high only around Γ where the bands are

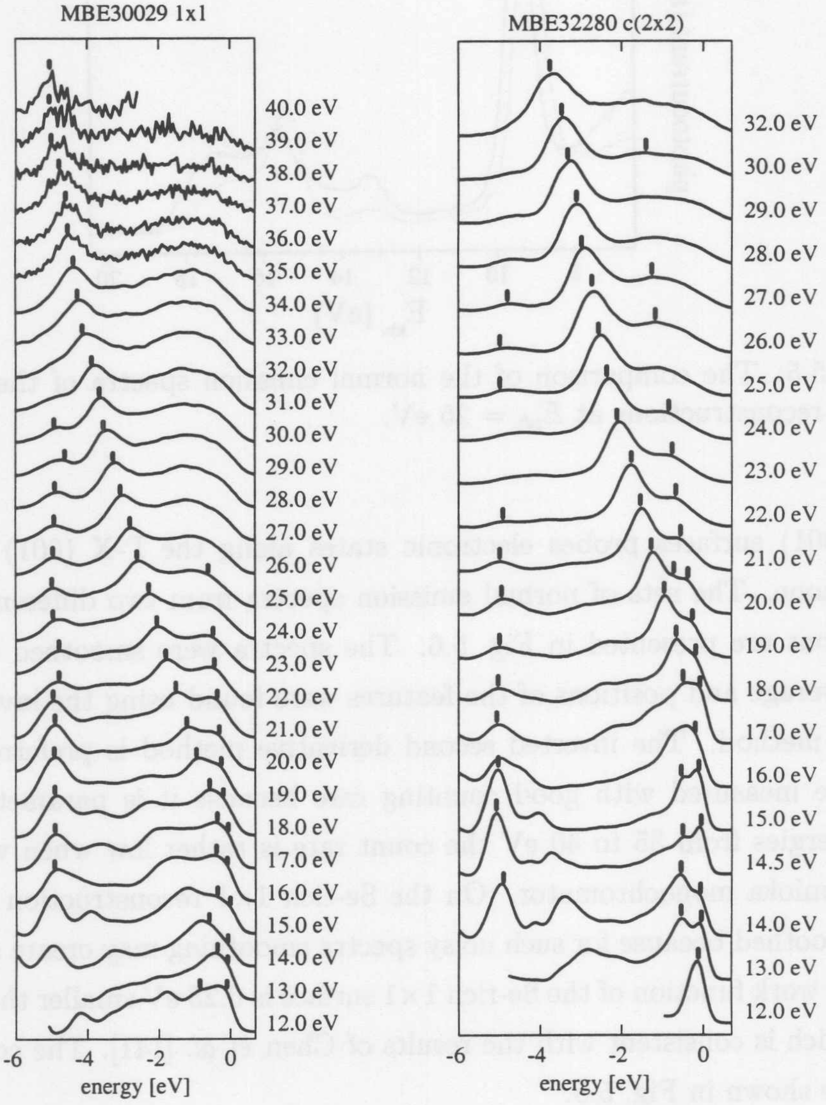

(a) Se-rich surface (b) c(2×2) reconstructed surface

Figure 5.6: Normal emission EDCs from the ZnSe(001) surface. Features arising from a primary-cone free-electron final state and the non-dispersive feature at the bottom of the valence band are indicated. The zero of the energy scale refers to the VBM.

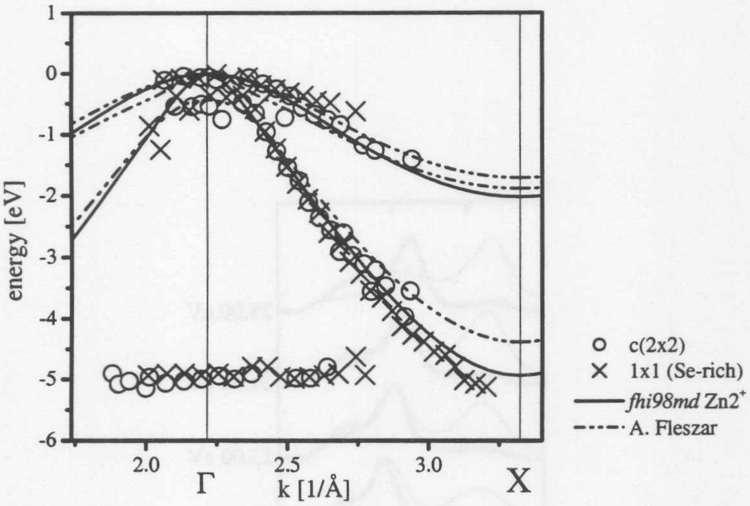

Figure 5.7: The band structure along Γ-X from the normal emission data presented in Fig. 5.6. For comparison the solid line shows the theoretical bands calculated using the *fhi98md* package and the dashed line shows the calculation of Andrzej Fleszar from [81].

Fig. 5.7 shows the band structure along Γ-X constructed from the features indicated in Fig. 5.6 with comparison to the theoretical calculations. The $k_\perp$ vectors are determined assuming a free-electron final state with $\vartheta = 0$

$$k_\perp = \sqrt{\frac{2m}{\hbar^2}(E_{kin} + V_0)} \tag{5.1}$$

where $V_0 = 11.2$ eV were found to reproduce the theoretical band dispersions the best. The $k_\perp$ vectors of the features are not reduced to the first Brillouin zone[5] ($G_\perp$ is not subtracted) in Fig. 5.7.

The agreement with theory is very good but the width of the valence band is best reproduced by the *fhi98md* calculation. As shown before, the calculation of A. Fleszar reproduces very exactly the experimental spin orbit splitting at the Γ point. There is an additional flat band at −5 eV energy. In reference [142] this was interpreted as a possible indirect transition from the high density of states at

---

flat. However, it does not explain why the split-off band intensity does not drop and as we will see in the next subsection heavy- and light-hole bands can be mapped by off-normal emission and their intensity does not drop away from Γ.

[5] The $k_\perp$ vectors of the theoretical calculations were scaled to match the high symmetry positions of the crystal with experimental lattice constant of $a = 5.67$ Å so that Γ points appear at $k_\perp = n \cdot 4\pi/a \approx n \cdot 2.216$ Å^{-1} where n are integers. Scaling of this type was used in all of the following figures.

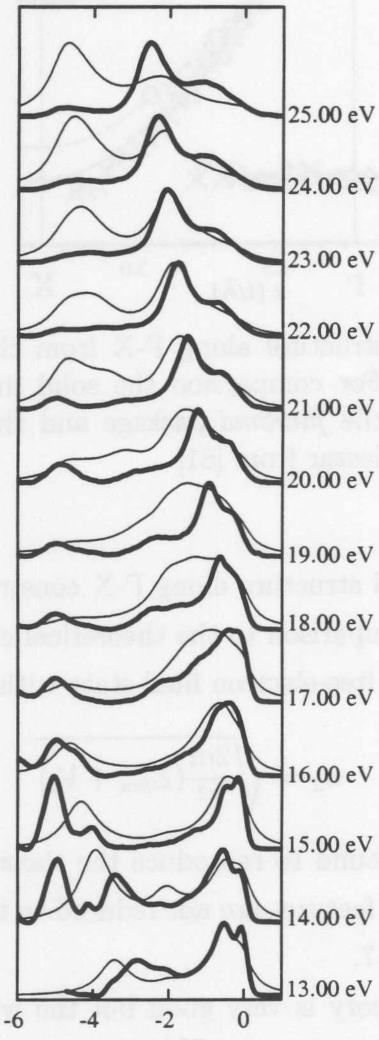

Figure 5.8: Comparison of the calculated (thin line) and experimental (thick line) normal emission spectra from ZnSe. The theoretical bulk spectra were calculated by A. Fleszar. Corresponding experimental normal emission spectra from the c(2×2) surface are shown that are presented in Fig. 5.6(b).

the bottom of the valence band. Later Olguín and Baquero [145, 146] showed that this band is surface induced and exists in II-VI zinc-blende semiconductors in general. They used tight-binding Hamiltonians and a surface Green-function matching method for the calculations and considered ideal non-reconstructed surfaces. For these reasons their results are a good starting point for the DFT-LDA calculations on the reconstructed ZnSe(001) surface presented in Sec. 5.3 of this thesis.

A comparison between the experimental and theoretically calculated spectra is shown in Fig. 5.8. Transitions from the initial to the final states were calculated by evaluating the following expression[6] [118]

$$\begin{aligned} I(E,\hbar\omega) \propto \; & \sqrt{E_{kin}}\, \textstyle\sum_{i,f} \lambda_f \int dk_\perp t_{\mathbf{k}f} \,|\, \langle \psi_{\mathbf{k}i} | \mathbf{A}\cdot\mathbf{p} | \psi_{\mathbf{k}f} \rangle \,|^2 \\ & \times \delta(E_f - E_i - h\nu)\; \delta(E - E_i), \end{aligned} \tag{5.2}$$

where $\psi_{\mathbf{k}i}$, E_i and $\psi_{\mathbf{k}f}$, E_f are the Kohn-Sham wavefunctions and energies of the bulk initial and final states. $I(E,\hbar\omega)$ is calculated as a function of the binding energy of the occupied states E and the incident photon energy $\hbar\omega$; $\mathbf{k} = (\mathbf{k}_{||} = 0, k_\perp)$ for normal emission, λ_f is the inelastic mean free path of final states E and E_{kin} is the kinetic energy of the detected photoelectrons. The quantity $t_{\mathbf{k}f}$ approximates the transmission coefficient across the surface barrier for a final state $\psi_{\mathbf{k}f}$. A more detailed description can be found in Ref. [118]. In this calculation the DFT-LDA band gap was corrected to its experimental value of 2.82 eV by arbitrarily shifting the final states. The surface was included only via the selection rules. Features were broadened using Gaussians to model the experimental spectra. The overall agreement between the theoretical spectra and the experimental data is quite good. Some peaks are slightly shifted, probably as a result of the arbitrary band-gap correction, however, this comparison allows non-free-electron final state transitions to be identified. It is apparent that all the experimental features are reproduced in the theoretical calculation only the surface-induced band at the bottom of the valence band is not present. We believe that some of the non free-electron final state features could also be quite well explained as secondary-cone transitions[7],

---

[6] The calculations that neglect 3d states in the Zn pseudopotential give results that are in good agreement with the experiment especially for the occupied valence bands. As mentioned in subsection 2.1.4 DFT-LDA calculations typically give wrong position of the 3d levels for zinc-blende binary semiconductor compounds. However, it should be noted that these 3d levels also influence the unoccupied band structure. This fact, although important will not be considered in this thesis.

[7] Good example of such interpretation for similar II-VI material ZnTe can be found in Ref. [144].

however, the comparison with theoretically calculated spectra includes these effects and therefore is preferred.

The overall conclusion is that the main features in the normal emission spectra from the ZnSe(001) surface could be well explained using the primary-cone free-electron final state model. On the other hand one should be aware of the limitations of this model. Comparison with the theoretically calculated spectra is probably the best way to analyze non free-electron final state transitions in detail.

The fact that the main features in the normal emission spectra originating from the split-off band dominate the normal emission EDCs and fit very well to a free-electron final state suggests that the ZnSe(001) surface may be ideal for more extensive normal emission studies within the simple model. In Ref. [120] it is suggested that when the set of spectra contain some well defined dispersive features, and when it is possible to identify the initial band related to these features one should create an *experimental* final band using the calculated initial bands. The present situation with ZnSe(001) is ideal - we have a dominating dispersive feature, the assignment of the initial band is unambiguous and the dispersion fits well to the calculated valence bands (in fact the discrepancies are smaller than the errors expected due to fitting). For this reason we decided to map the whole Brillouin zone by adjusting the angle and photon energy according to the primary-cone free-electron formulas

$$\begin{aligned} k_{\|} &= \sqrt{\frac{2m}{\hbar}E_{kin}}\sin\vartheta \\ k_{\perp} &= \sqrt{\frac{2m}{\hbar}(E_{kin}\cos^2\vartheta + V_0)}. \end{aligned} \tag{5.3}$$

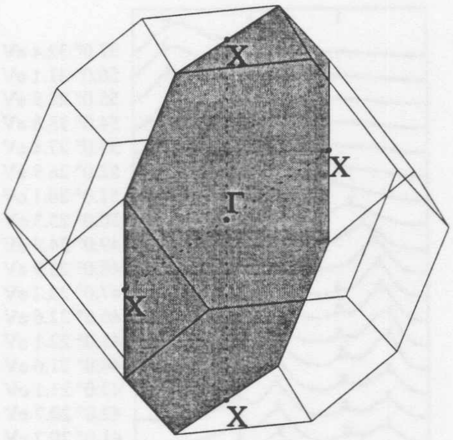

Figure 5.9: Cut through the Brillouin zone showing accessible bulk *k-points* when measuring the (001)-c(2×2) surface along the $\bar{\Gamma}$-$\bar{J}_{c(2\times2)}$ direction. It is often denoted as the ΓKWX plane.

5.2.2 Band structure along Γ-X from off-normal emission

From Fig. 5.1 one can see that the Γ-X direction is not only accessible in normal emission. The section of the BZ containing the Γ-X(001) and Γ-X(100) directions shown in Fig. 5.9 is accessible when performing off-normal scans along $\bar{\Gamma}$-$\bar{J}_{c(2\times2)}$ direction of the surface BZ. Assuming the primary-cone free-electron final state model allows one to scan the desired line in the Brillouin zone by properly choosing the photon energy E_{ph} and emission angle ϑ using the formulas of (5.3). In the following subsections we will show that in the case of the ZnSe(001) surface this procedure provides results that are in excellent agreement with theory.

The set of spectra along the Γ-X(100) off-normal direction measured on the ZnSe(001)-c(2×2) reconstructed surface is presented in Fig. 5.10. The spectra were smoothed with a Savitzki-Golay local polynomial algorithm and the features were located using inverted second derivative spectra. As it can be seen we have measured a large number of EDCs with a small angular step that allows a very detailed interpretation of the data. In contrast to the normal emission experiment, in this case heavy- and light-hole bands are clearly visible. The theoretical *k*-space locations[8] of the spectra are presented in Fig. 5.11. As can be seen, the photon energies and angles were selected such that the features around the VBM are closest to the Γ-X(100) line. For the spectra at small emission angles the $k_\perp$ displacement

---

[8] Similar interpretation can be found in Ref. [147].

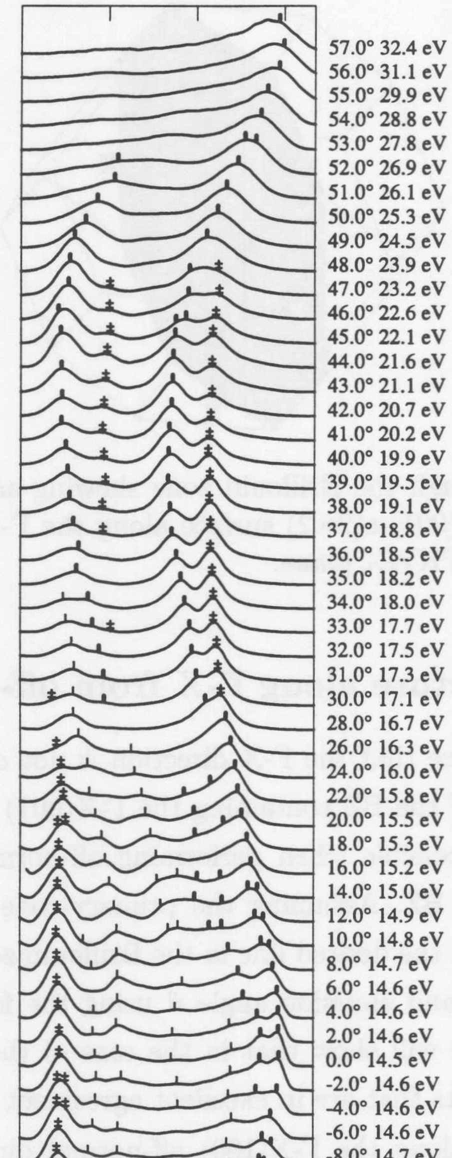

Figure 5.10: Set of spectra along Γ-X direction in the bulk Brillouin zone. Thicker tick symbols indicate bulk related free-electron final state features and ‡ symbols indicate surface-related features. Thinner tick symbols indicate features identified as a transitions to non free-electron final states.

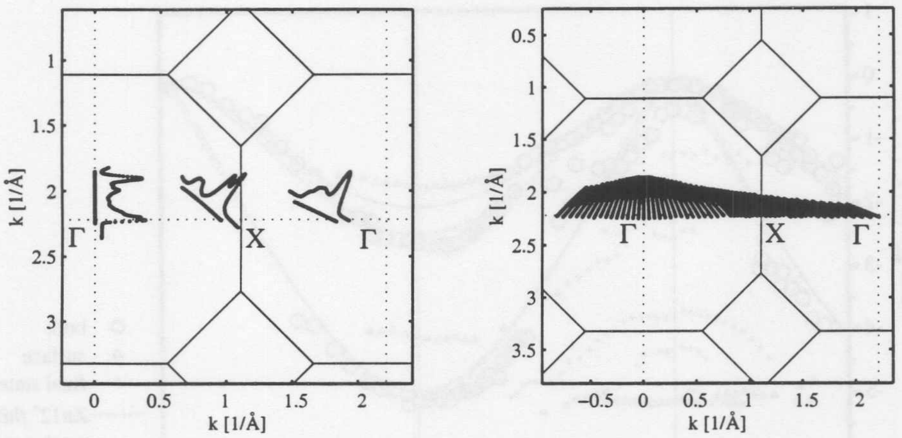

Figure 5.11: Positions of the features from the Γ-X spectra in the section of the Brillouin zone calculated assuming free-electron final states. The left picture shows selected spectra and their positions in BZ for: 0° - 14.5 eV, 26° - 16.3 eV and 52° - 26.9 eV. The right picture shows the corresponding positions for all of the spectra.

from the Γ-X(100) line is significant. On the other hand especially for spectra at higher angles this effect gets smaller and its influence is less important when the X point is passed. Another essential information from Fig. 5.11 is that the whole Γ-X-Γ(100) line can be mapped with the photon energies and angles accessible with our monochromator. Note that this is twice as much as in the normal emission experiment. Fig. 5.12 shows the band dispersions constructed from features indicated in Fig. 5.10 compared with the two theoretical calculations. The splitting of the heavy- and light-hole bands around the X point cannot be clearly decided from the calculation with the Zn^{2+} pseudopotential. From the comparison with the Zn^{12+} calculation we conclude that the lower of the split bands is a bulk heavy- and a light-hole band and the higher one is a surface-related state[9]. The width of the split-off band is in very good agreement with the Zn^{12+} calculation and reaches a minimum value of -5.1 eV (with accuracy of ± 0.1 eV) at the X point.

Fig. 5.13 presents the spectra from Fig. 5.10 in another way. The spectra are plotted on a gray-scale in the $E(k_{||})$ plane assuming of the free-electron final states. The darker shade of grey indicates a higher photocurrent. Such a graphical presentation of the data is useful to inspect the general trends in the band dispersions

---

[9] The analysis of the c(2×2) surface structure is presented in Sec. 5.3 and here we only discuss bulk features.

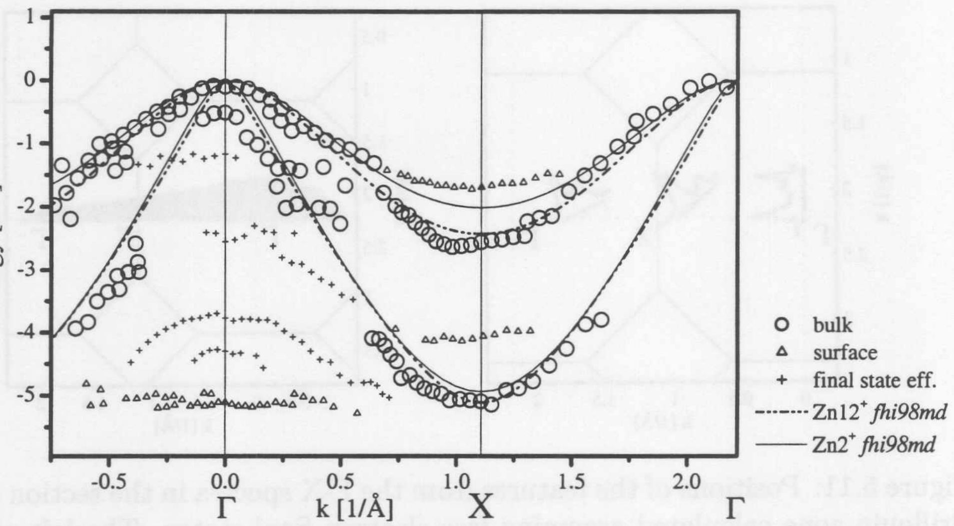

Figure 5.12: Band dispersions in the Γ-X Brillouin zone direction constructed from features indicated in Fig. 5.10. Open circles indicate features identified as a primary-cone free-electron final state transitions, triangles indicate surface states and plus symbols non-primary-cone transitions.

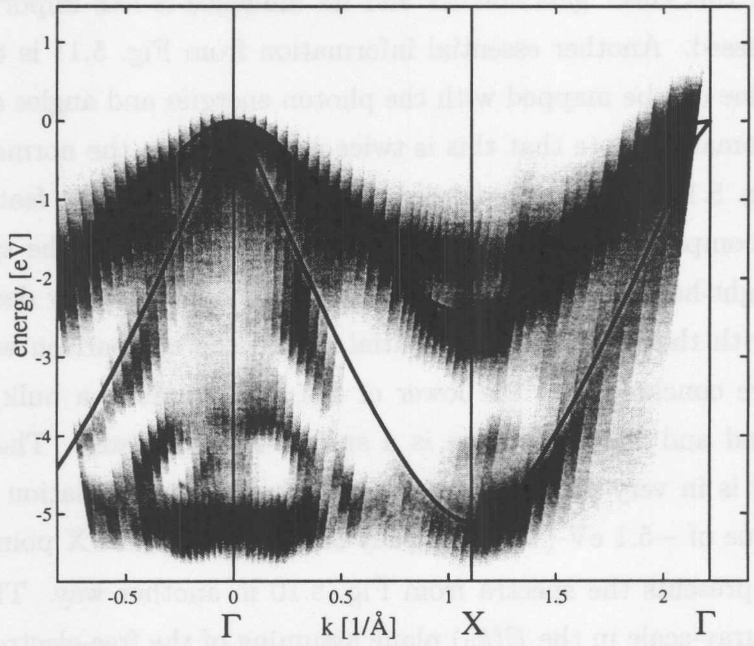

Figure 5.13: The structure plot of the EDCs along Γ-X Brillouin zone direction. The solid lines show the theoretical spectra calculated using *fhi98md* with the Zn^{12+} pseudopotential.

especially for the features with higher intensity. The overall impression of this structure plot is that the main long-range dispersions stay within the free-electron final state regime. The region at around $k_{||} = 0$ suffers from the fact that $k_\perp$ is not always close to the Γ-X line. The splitting of the light- and heavy-hole band at around X is one of the dominating features.

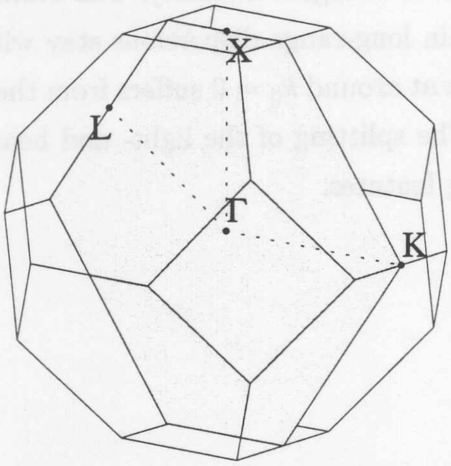

Figure 5.14: Section through the Brillouin zone showing accessible bulk k-points when scanning (001)-c(2×2) surface along the $\bar{\Gamma}$-$\bar{\text{J}}$ or $\bar{\Gamma}$-$\bar{\text{J}}'$ directions. It is often denoted the ΓKLUX plane.

5.2.3 Band structure along Γ-K-X

Assuming the free-electron primary-cone model one can map out the Γ-K-X high symmetry direction in BZ by scanning along the $\bar{\Gamma}$-$\bar{\text{J}}$ or $\bar{\Gamma}$-$\bar{\text{J}}'$ directions on c(2×2) surface with selected photon energies $\hbar\omega$ and angles ϑ (see Fig. 5.1). Fig. 5.14 shows the plane of accessible k-points in this case. We have performed detailed scans in this direction and the set of EDCs is presented in Fig. 5.15. Such dense scanning is time consuming with our experimental equipment, but allows reliable identification of the peak dispersions. The spectra were smoothed with the Savitzky-Golay local polynomial algorithm and the spectral features were identified using inverted second derivatives.

The positions of the spectra in the accessible Brillouin zone plane have been drawn in Fig. 5.16. In this case the higher $\hbar\omega$ and ϑ the closer the spectra lie to the desired Γ-K-X direction. At around $E_{ph} = 21.1$ eV and $\vartheta = 43°$ the crossing of the BZ boundary occurs not very close to the K point for some features.

The band structure constructed from the features indicated in Fig. 5.15 is presented in Fig. 5.17. The comparison to the theoretical calculation confirms that a large number of features are correctly interpreted with free-electron final states. The band dispersions are smooth and clear especially for the case of the light- and heavy-holes bands which in the case of Γ-K-X direction show a distinct splitting.

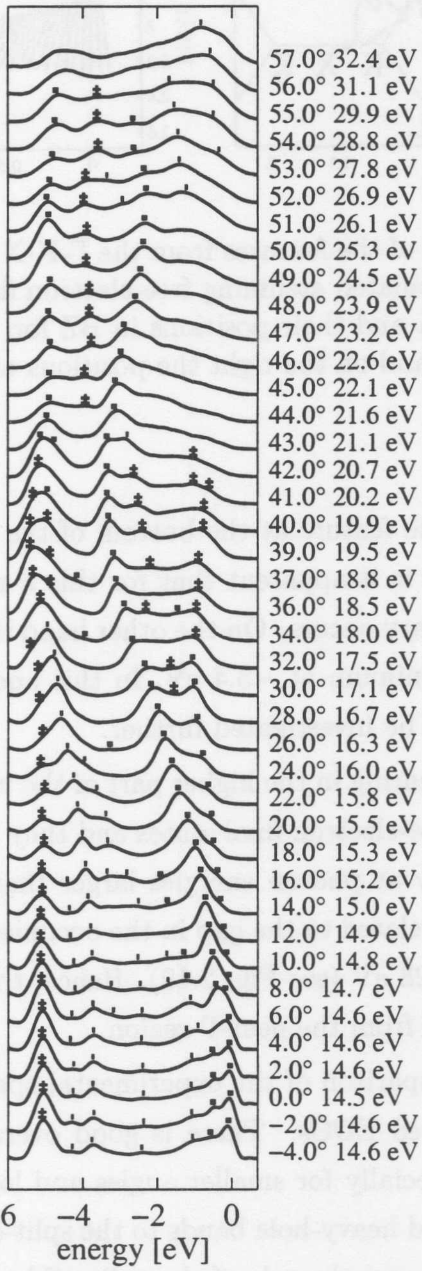

Figure 5.15: Set of spectra along the Γ-K-X direction in the bulk Brillouin zone. Thicker tick symbols indicate bulk related free-electron final state features and ‡ symbols indicate surface-related features. Thinner tick symbols indicate features identified as transitions to non free-electron final states and unassigned features.

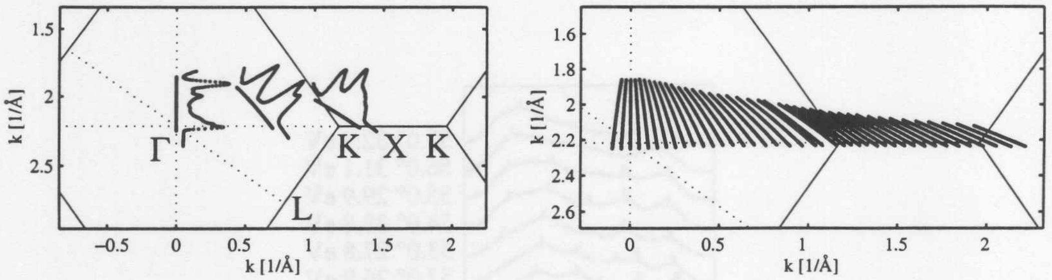

Figure 5.16: Positions of the features from the Γ-K-X spectra in the section of the Brillouin zone calculated assuming free-electron final states. Figure at left shows selected spectra and their positions in BZ for: 0° - 14.5 eV, 26° - 16.3 eV and 43° - 21.1 eV and on the right the positions of all the series of spectra are shown.

There is a problematic feature at the bottom of the valence band for k around 0.8 Å^{-1}. From Fig. 5.16 it is apparent that for this k-range the above mentioned crossing of the BZ boundary occurs. On the other hand the feature lies much deeper than expected with a minimum at -5.4 eV. In this and following subsections the origin of this feature will be investigated further.

The two features appearing in the higher part of the valence band for the highest k-vectors do not fit to free-electron final states and they are not likely to be surface states. They appear only at photon energies larger than 25 eV and it is intuitive that their appearance is related to the gap in the occupied states that appear at the Γ point between 18 and 28 eV (see Fig. 2.12). Hence, they could be interpreted as secondary-cone emissions from the near-Γ region.

Fig. 5.18 shows a comparison of the experimental spectra (as in Fig. 5.15) with the theoretically calculated EDCs. There is good overall agreement between experiment and theory especially for smaller angles and lower energies. The relative intensities of the light- and heavy-hole bands to the split-off band are also indicated. The calculation overestimates the role of the split-off band (probably due to selection rules) so the intensities from this band were reduced by the factor of 2, and the resulting theoretical EDC was calculated using $P(E) = P_{l-\ and\ h.-holes} + \frac{1}{2}P_{split-off}$. Four aspects deserve further comment:

1. The non dispersive feature at angles 26° - 46° at an energy of -1 eV is reproduced in the theoretical calculation and therefore cannot be a surface state.

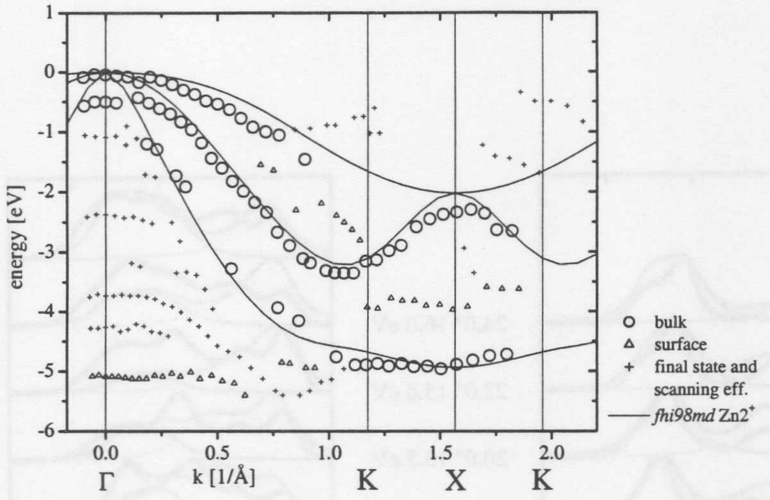

Figure 5.17: The band dispersions in Γ-K-X Brillouin zone direction constructed from the spectral features indicated in Fig. 5.15 in comparison to the theoretical bands calculated with the *fhi98md* code using Zn^{2+} pseudopotential.

2. The above mentioned feature at the bottom of the valence band for angles 34 - 42° is reproduced in the theoretical calculation, however, it appears shifted by more than 0.5 eV with respect to the the experimental peak.

3. Features at the largest angles for energies around -1 and -2 eV are reproduced e.g. in the last spectrum at 54° - 28.8 eV.

4. The dispersion of the feature at around -4 eV for large angles is not given by the calculation so we conclude that it is a surface resonance.

A structure plot created using all the spectra from Fig. 5.15 is presented in Fig. 5.19. It is apparent that for the primary cone only the light-hole band shows significant intensity. The other dominating features are the dispersion at the bottom of the band at 0.5 - 1 $\mathrm{\AA}^{-1}$ and the secondary-cone emissions appearing in figure between X and the second K point.

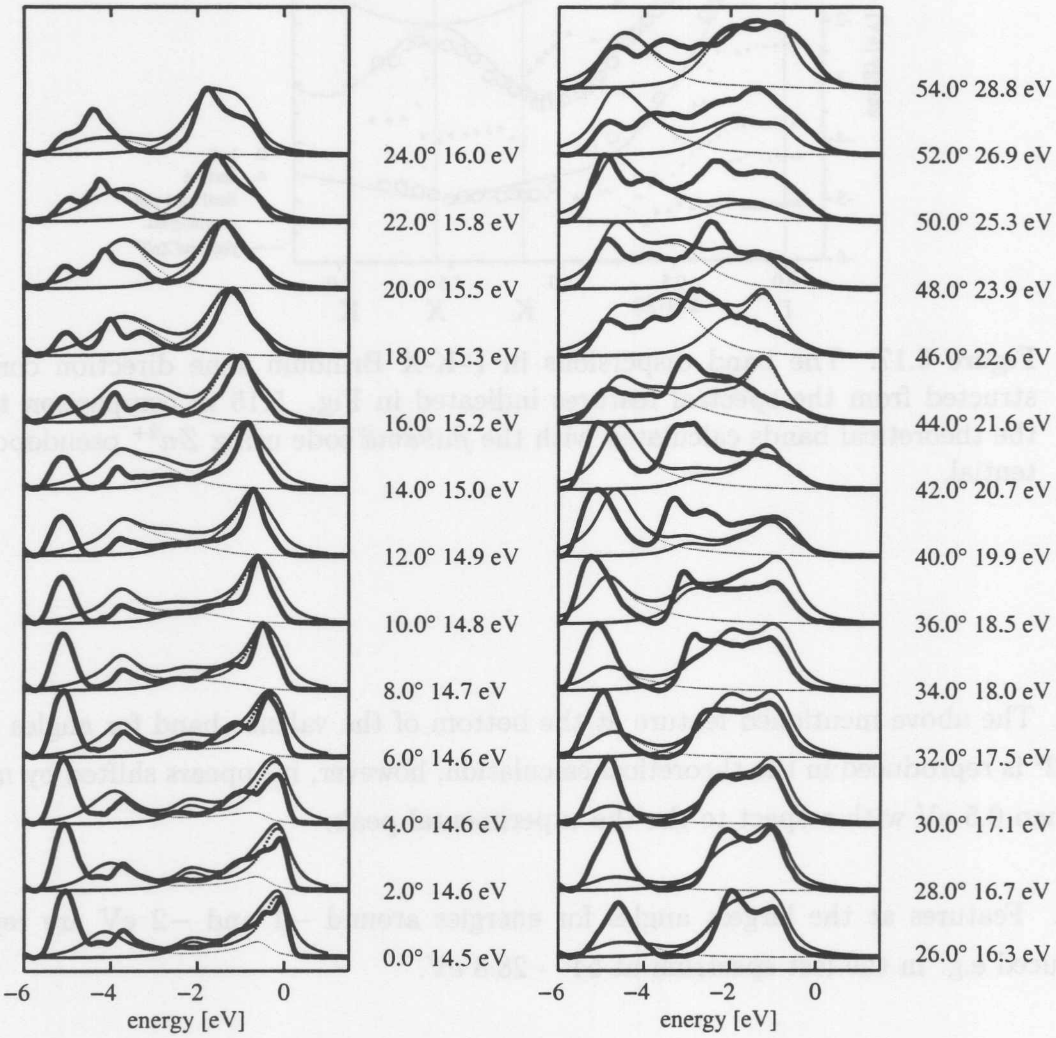

Figure 5.18: Comparison of the measured and theoretical EDCs for off-normal emission along Γ-K-X direction. Thick lines show measured and thin lines theoretical spectra. Smaller dots show theoretical emissions from the split-off and larger dots emissions from the light- and heavy-hole bands (the theoretical spectra by A. Fleszar).

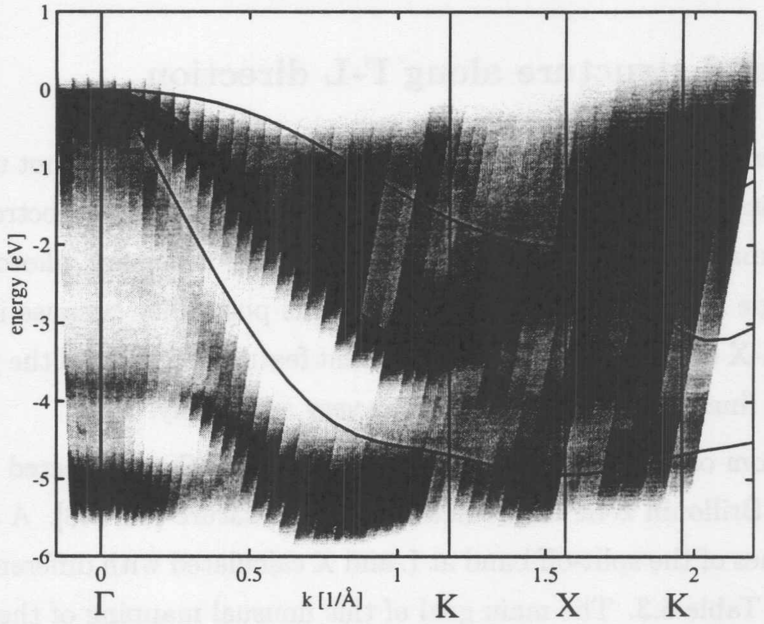

Figure 5.19: Structure plot of the spectra along the Γ-K-X direction in BZ created assuming the primary-cone free-electron model. The photocurrent intensity is presented on a gray-scale. The darker color indicate higher intensity. Thin solid lines indicate theoretical bands calculated using *fhi98md* with the Zn^{2+} pseudopotential.

point	Chadi-Cohen [70]	Chelikowsky-Cohen [148]	Bernard-Zunger [74]	*fhi98md* Zn^{2+}	experiment
L	−4.7	−5.08	−5.21	−5.16	−5.18±0.1
X	−4.8	−4.96	−4.82	−4.94	−5.10±0.1

Table 5.3: Eigenvalues of the split-off band for ZnSe at L and X relative to the valence band maximum.

5.2.4 Band structure along Γ-L direction

The Γ-L direction on the (001) surface of zinc-blende materials is not usually studied by photoemission. However, assuming the primary-cone free-electron model it is possible to map every desired BZ direction if the necessary photon energy and emission angle are accessible. We exploited this possibility because in the data for Γ-X and Γ-K-X directions there were apparent features that fitted the photoemission free-electron final state model predictions very accurately.

The bottom of the split-off band for zinc-blende ZnSe is expected to be at the L point of the Brillouin zone as predicted in the literature [74, 148]. A comparison of the eigenvalues of the split-off band at L and X calculated with different methods are presented in Table 5.3. The main goal of this unusual mapping of the Γ-L direction was to map the bottom of the split-off band at L within the context of the results in the Γ-K-X direction.

The Γ-L direction is accessible at the same emission plane as Γ-K-X direction as can be seen in Fig. 5.14. The spectra collected at specially selected photon energies and angles are presented in Fig. 5.20. The overall impression is that the spectra are rather structureless with the prominent feature close to the VBM for all EDCs. We would like to point out that there is an apparent difference between the present set and the set for the Γ-K-X direction. This proves that even though the same emission plane is used different k-points are mapped.

The positions of the spectra in the the Brillouin zone are presented in Fig. 5.21. At the accessible photon energies it was possible to map-out the whole Γ-L line. The line is quite accurately mapped and no additional effects that could originate within the free-electron model are expected.

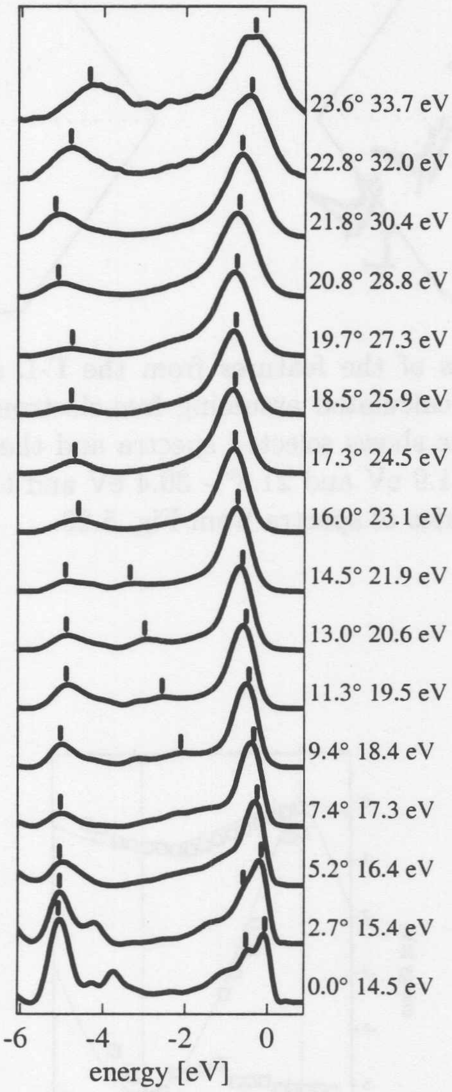

Figure 5.20: Set of EDC along Γ-L direction in Brillouin zone. Photon energies $\hbar\omega$ and emission angles were selected after analyzing normal emission data. Only features that were identified as being bulk-related and the flat band at the bottom of the valence band are indicated.

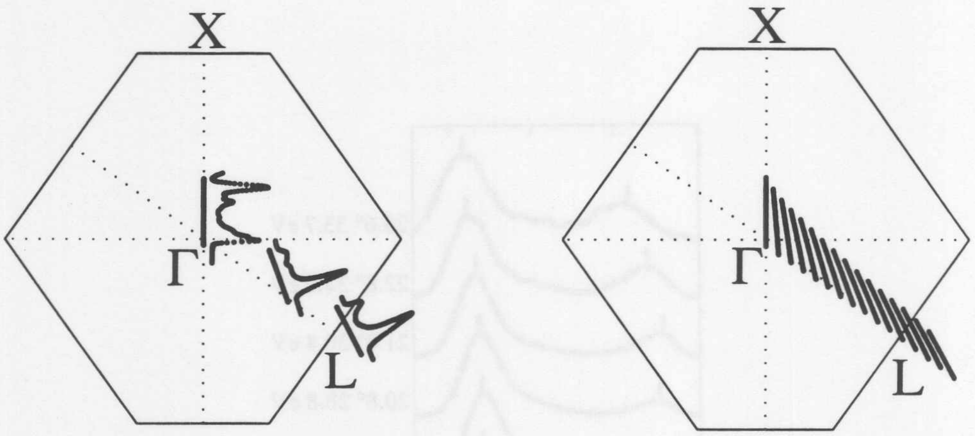

Figure 5.21: Positions of the features from the Γ-L spectra in the section of the Brillouin zone calculated assuming free-electron final states (primary cone). The left picture shows selected spectra and their positions in BZ for: 0° - 14.5 eV, 14.5° - 21.9 eV and 21.8° - 30.4 eV and the right picture shows the positions of the series of spectra from Fig. 5.20.

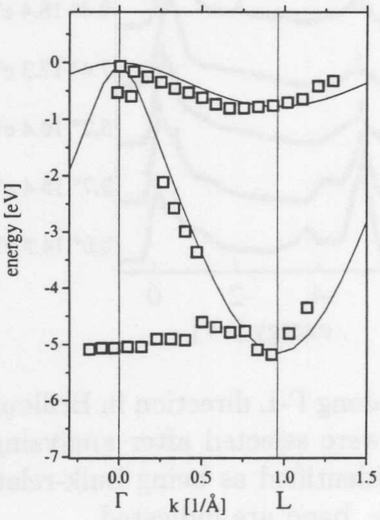

Figure 5.22: The band structure along Γ-L constructed from the features indicated in Fig. 5.20. The solid lines show theoretical bands calculated using the *fhi98md* package using the Zn^{2+} pseudopotential.

The resulting band structure is presented in Fig. 5.22. The positions of the *k*-points (as shown in Fig. 5.21) were projected on the Γ-L line. The overall agreement with the theoretical band is very good and demonstrates that the idea of this measurement was correct. Especially the mapping of the light- and heavy-hole bands is very convincing, however, again no splitting of these bands can be observed. The bottom of the split-off band at L is slightly deeper than that measured at X - the numbers are presented in Table 5.3. It is around 0.2 eV above the deep feature measured at Γ-K-X direction. This may indicate that either the L point is not mapped accurately (i.e. the free-electron approximation fails) or that the feature from Γ-K-X measurement is not bulk-related. On the other hand the differences of 0.2 eV could be considered as fitting inaccuracies. We address this problem in the next section where we consider the surface structure of ZnSe(001)-c(2×2).

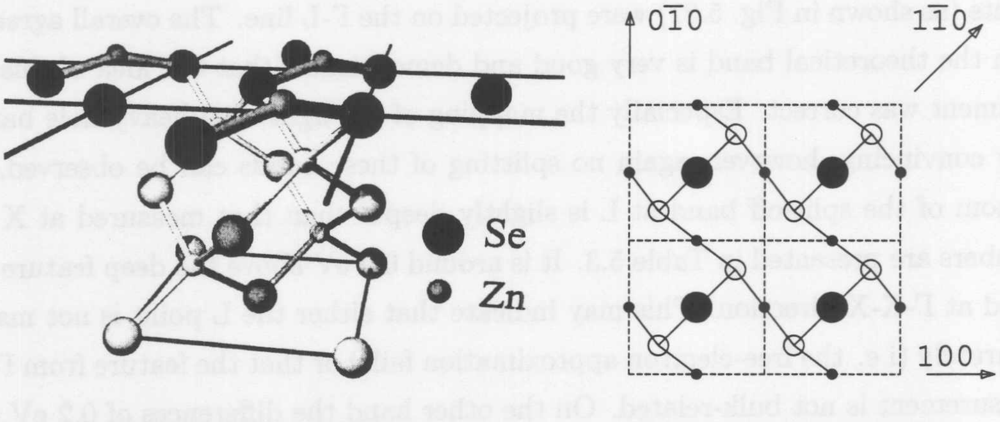

(a) Schematic 3D view of the surface. (b) Top view on the surface.

Figure 5.23: Schematic view of the Zn-terminated ZnSe(001)-c(2×2) reconstructed surface and the main symmetry directions.

5.3 ZnSe(001)-c(2×2) surface geometry and electronic structure

The (001) surfaces of zinc-blende II-VI semiconductors are typically grown on GaAs(001) oriented substrate. The first models for the ZnSe(001)-c(2×2) surface were published in early 90's and the Zn-vacancy structure proposed by Farrell *et al.* [149] is qualitatively valid and was confirmed in all later theoretical and experimental studies.

5.3.1 Relaxation of the surface

Tables 5.4 and 5.5 show the theoretical and experimental positions of the atoms at the ZnSe(001)-c(2×2) surface. In this reconstruction the top layer Zn atoms are nearly co-planar with the second layer selenium and the bonds between top and second layer atoms are shorter than in the bulk. There are slight differences between the different calculations and experimental results in the literature. Hence it was decided to perform a theoretical investigation of the surface relaxation in order to optimize the geometry for the band structure calculations. The surface atoms were allowed to relax until the forces on each atom were smaller than 0.01 eV/Å. This is quite a stringent criterium compared to other calculations. We also tested the

	position [a_0]			energy [eV]	force [eV/Å]
	x	y	z		
	Garcia & Northrup [89]			−0.0146	0.2
surface Zn	0.0000	0.0000	−0.2120		
second layer Se	−0.0028	−0.0028	0.0060		
	Park & Chadi [87, 150]			−1.2342	*n.a.*
surface Zn	0.0000	0.0000	−0.2257		
second layer Se	−0.0287	−0.0287	0.0035		
third layer Zn	0.0000	0.0000	−0.0018		
	Stefan Gundel [88]			−1.2470	0.02
surface Zn	0.0000	0.0000	−0.2011		
second layer Se	−0.0305	−0.0305	−0.0014		
third layer Zn	0.0000	0.0000	−0.0077		
	this work			−1.2787	0.01
surface Zn	0.0000	0.0000	−0.1988		
second layer Se	−0.0339	−0.0339	0.0130		
third layer Zn	0.0000	0.0000	−0.0035		

Table 5.4: Atomic coordinated on the ZnSe(001)-c(2×2) surface. The positions are relative to ideal bulk positions. The values are in lattice constant a_0 units. The coordinate system of the cubic fcc lattice cell is used. The surface energy values with respect to the unrelaxed surface are given. The force value indicates the relaxation criterium - it is a maximum force allowed for each atom.

	position		
	x	y	z
	Ohtake *et al.* [150]		
surface Zn	0.0000	0.0000	−0.1640
second layer Se	−0.0624	−0.0624	0.0829
third layer Zn	0.0000	0.0000	−0.0494
	Weigand *et al.* [151]		
surface Zn	0.0000	0.0000	−0.1870
second layer Se	−0.0285	−0.0285	0.0230
third layer Zn	0.0000	0.0000	0.0060
fourth layer Se	−0.0025	0.0025	0.0040
fifth layer Zn	0.0000	0.0000	0.0010
sixth layer Se	−0.0010	−0.0010	0.0000

Table 5.5: Atomic coordinates of the ZnSe(001)-c(2×2) surface. The positions are relative to ideal bulk positions. The values are in lattice constant a_0 units. The coordinate system of the cubic fcc lattice cell is used.

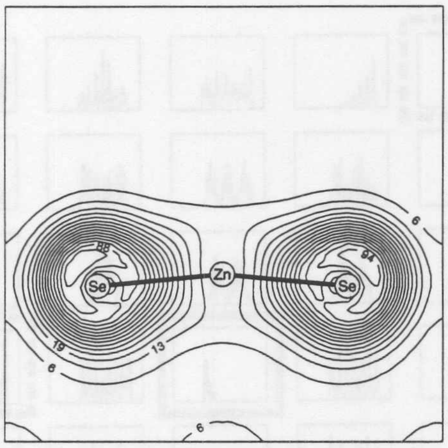

Figure 5.24: Total valence band charge density contour for ZnSe(001)-c(2×2) surface. Maximal charge was normalized to 100. Units are relative to the maximum.

atomic coordinates obtained by other authors in the *fhi98md* code, however, the best total energy for the system was obtained with the relaxation performed in this work[10].

It should be noted that the total energy does not change within the numerical accuracy for a change of the atomic positions of $0.001 \times a_0$. The present results are very close to these of Park & Chadi [87] and Gundel [88]. The result of Garcia & Northrup [89] only took the two uppermost layers into account and the total energy is worse than the others. This indicates that at least 3 uppermost layers should be relaxed because the gain in total energy can be as large as 1 eV per super-cell. Relaxation of more layers is possible, however, it is difficult to obtain good convergence within a reasonable time. The accurate high-resolution x-ray diffraction (HRXRD) experimental results of Weigand *et al.* [151] show that on real surfaces five or six atomic layers relax. We also tried to perform theoretical optimization of 5 uppermost layers which results in some additional total-energy gain and minimization of the forces to less than 0.01 eV/Å[11]. The surface band structure

---

[10] In the table 5.4 differences in total-energy between the different atomics positions are indicated. These are values obtained by inserting the atomic positions in the *fhi98md* code, and they do not mean that the previously published values are not accurate - they were calculated with the different parameters using different pseudopotentials, different code etc. The small differences in energies indicate good overall agreement between the different results and relative independence on the pseudopotential and DFT-LDA code employed.

[11] There was no definitive convergence of the atomic positions within couple of weeks of the

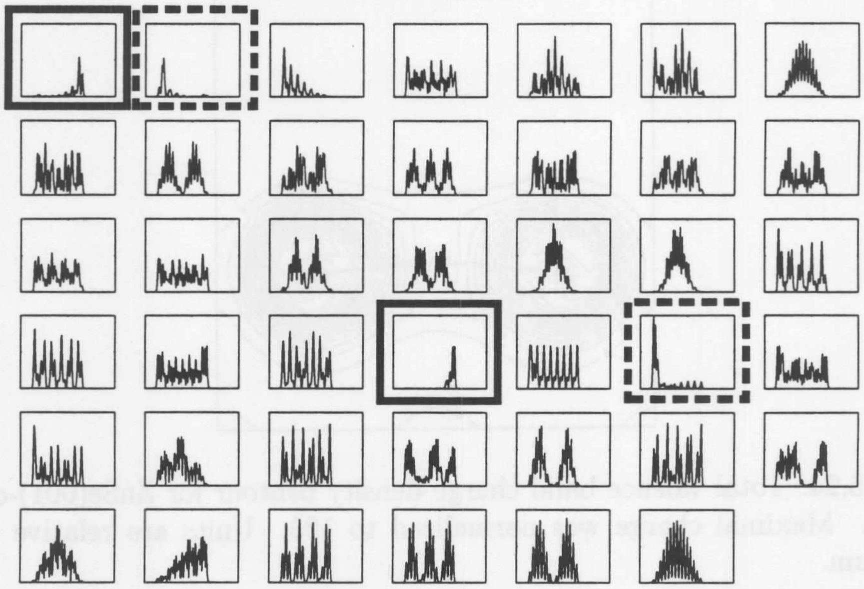

Figure 5.25: Charge densities along the z-axis of a 31-layer slab used for the surface band structure calculation. The abscissa is along the z-axis of the slab, each subfigure is individually normalized. Electronic states from 80 to 120 are shown (state 120 is the last occupied). The charge densities are k-resolved and the densities at half way between $\bar{\Gamma}$ and $\bar{\mathrm{J}}, \bar{\mathrm{J}}'$ are shown. The solid frames indicate surface states along $\bar{\Gamma}$-$\bar{\mathrm{J}}'$ and the dashed frames along $\bar{\Gamma}$-$\bar{\mathrm{J}}$.

calculation with only three relaxed atomic layers provides adequate localization of the surface features and is therefore satisfactory for most purposes. We have in fact performed the surface band structure calculations with both 3 and 5 layers relaxed and the states on the 3-layers-relaxed surface were easier to identify. Moreover, both structures were compliant with an accuracy better than 0.1 eV. Also the results of calculations using the experimental positions from [151] or slabs passivated with partially charged hydrogen atoms on one side were similar.

---

program run on the state-of-the-art 1 GHz Intel-based server. In the future we plan to perform such run on Cray T3E with the parallel architecture to have the direct comparison to the result of [151].

5.3.2 Theoretical ZnSe-c(2×2) surface electronic structure - an adsorbate-like system

The electronic structure of the ZnSe-c(2×2) surface was calculated using *fhi98md* with Zn^{2+} pseudopotential. A slab of 31 atomic layers (15 Se and 16 Zn layers) was used terminated on both sides with the Zn-c(2×2) vacancy structure. The slabs were separated by the vacuum equivalent to 7 lattice constants to avoid any interaction between the surfaces. We define the z-axis [001] as the one perpendicular to the surface of the slab as indicated in Fig. 5.1. The relaxation of 3 layers on both sides as given in Table 5.4 was applied. The super-cell of the slab contained 30 Zn and 30 Se atoms, thus there were 240 electrons in the super-cell. Since the *fhi98md* code does not include spin effects such a super-cell provided 120 occupied electronic states. The surface states were identified by inspection of the charge densities integrated along the z-axis of the slab. Typical charge densities are shown in Fig. 5.25. For the (001) surface of the zinc-blende materials the $\bar{\Gamma}$-$\bar{\mathrm{J}}$ and $\bar{\Gamma}$-$\bar{\mathrm{J}}'$ directions are not equivalent so the surface structure along both lines is different. The presence of the c(2×2) reconstruction on both sides of the slab allows the states belonged to $\bar{\Gamma}$-$\bar{\mathrm{J}}$ and $\bar{\Gamma}$-$\bar{\mathrm{J}}'$ directions to be identified simultaneously saving the computational time. States appear asymmetrically on different sides of the slab when inspecting the k-points along e.g. [110] direction. When inspecting k-points along [100] $\bar{\Gamma}$-$\bar{\mathrm{J}}_{c(2\times2)}$ direction the states appear symmetrically on both sides of the slab.

Figure 5.26 shows the calculated surface electronic band structure. The shapes of the bands are similar to those of CdTe(001)-c(2×2) published in Ref. [71]. We have used slightly different method to identify the surface bands and more bands were found. However, the key band for the reconstruction is the one at -4 eV at the Γ point. It is the only one for which dispersion is very different in the $\bar{\Gamma}$-$\bar{\mathrm{J}}$ and $\bar{\Gamma}$-$\bar{\mathrm{J}}'$ directions and therefore it is expected that the properties of the wave function for this band will have the same symmetry as the c(2×2) reconstruction[12].

We start the detailed analysis of the surface charge densities with the relatively flat surface resonance that appears at -1.5 eV at the Γ point. It becomes a *true* surface state in the $\bar{\Gamma}$-$\bar{\mathrm{J}}_{c(2\times2)}$ direction where the projected and surface band structures have different periodicities. In Fig. 5.27 the k-resolved charge densities at Γ

---

[12] We have shown in the previous sections that the different DFT-calculated electronic structures may differ (e.g. in valence band width) by 0.1 eV or more, depending on the pseudopotentials used, lattice constant etc. Therefore the energy values of the surface bands from Fig. 5.26 may have an uncertainty of this magnitude.

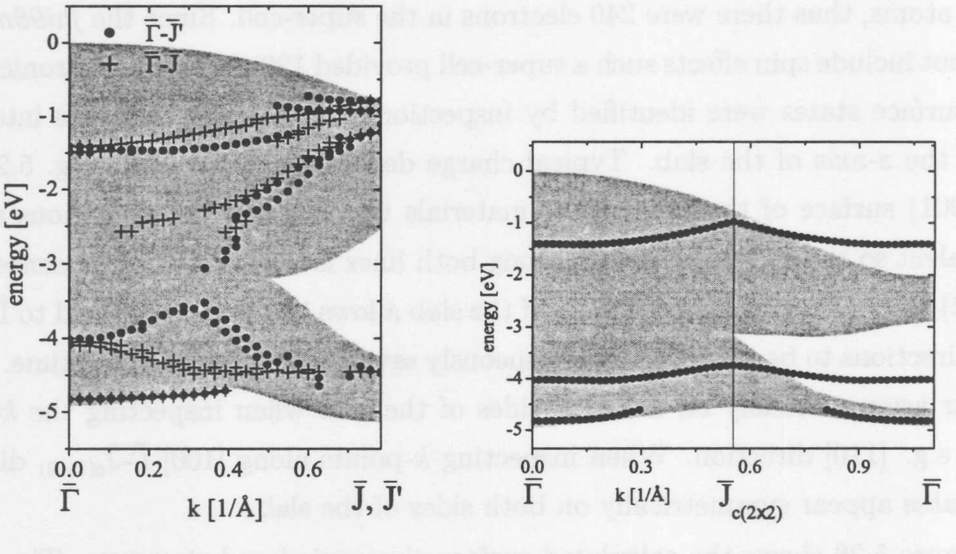

Figure 5.26: The calculated surface electronic band structures of the ZnSe(001)-c(2×2) surface. The definitions of the surface directions are given in Fig.5.1. Shaded areas show the projected bulk band structure.

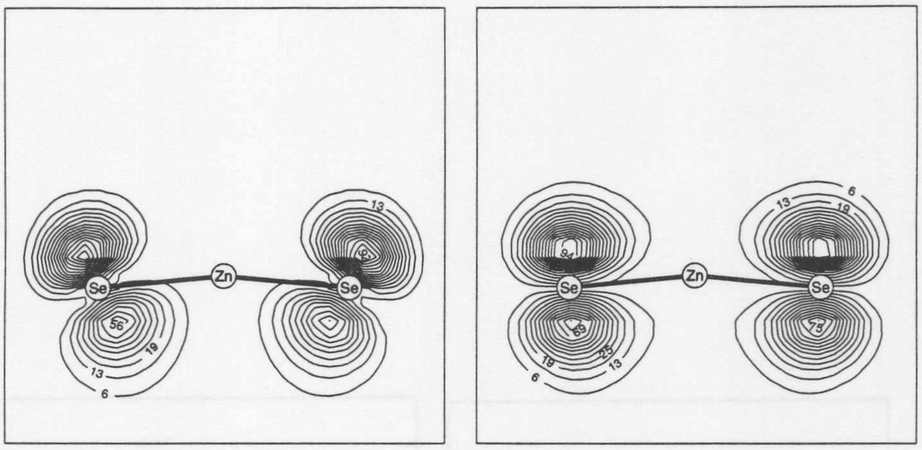

(a) $\bar{\Gamma}$

(b) Middle of the $\bar{\Gamma}$-$\bar{\mathrm{J}}'$

Figure 5.27: Comparison of contour plots of the charge densities for the surface resonance that appears at -1.5 eV at Γ point. Each plot is individually normalized to the maximum value of 100.

and half way between $\bar{\Gamma}$ and $\bar{\mathrm{J}}'$ are presented. It is apparent that this state is formed from the π-like bonding of the Se 4p orbitals. The symmetry of the π-like bond is consistent with the fact that the dispersion of this state is similar in [110] and [1$\bar{1}$0] directions, however, at $\bar{\Gamma}$ the symmetry is slightly affected probably by the fact that the Se-Zn-Se angle is not exactly 180° and by inter-layer interactions.

The situation with the resonance at -4 eV at Γ is slightly more complicated but this state can be interpreted using molecular terminology. A comparison of the DFT contour-plots at Γ for this feature is presented in Fig. 5.28. The Fig. 5.28(b) shows a contour-plot for a simple molecule with 180° bond angle. One can describe this result using a linear combination of the 4s and 4p states of Zn and Se. It is necessary to promote one electron from the Zn 4s to the 4p state to obtain two hybridized sp orbitals that can bond to the 4p orbitals of Se. The comparison between the different calculations is very good showing that this surface-feature is electronically separated from the deeper bulk layers.

Fig. 5.29 shows the charge densities for the additional features indicated on the surface band structure plots. The contour-plots are very similar and indicate the inter-chain interactions between the c(2×2) Se-Zn-Se chains. The p-character of the bonds is apparent and, in this geometry they form an interesting mix of σ and π-like

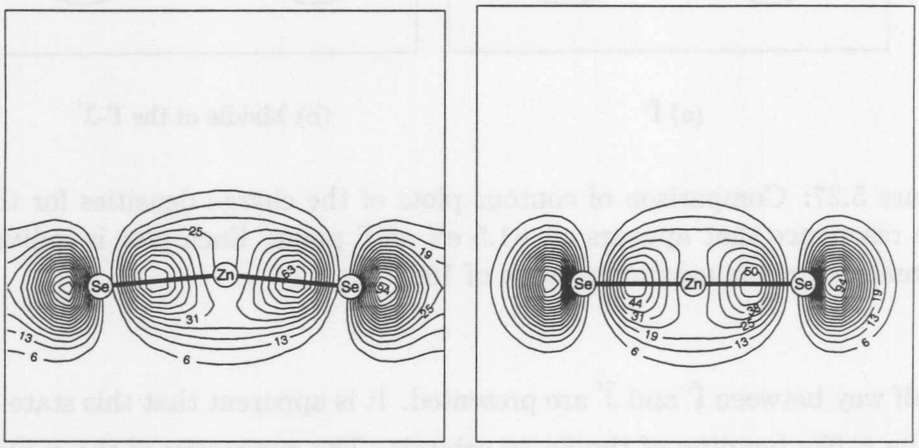

(a) surface of the slab (b) separated molecule

Figure 5.28: Comparison of contour plots of the charge densities:(a) contour plot of the k-resolved charge density of surface resonance at -4 eV at the Γ point. The contour plane is normal to the surface and contains surface Zn and subsurface Se atoms (b) contour for the same electronic level for the isolated Se-Zn-Se molecule. The distance Se-Zn was taken as $0.25\sqrt{2}a_0$, where theoretical $a_0 = 5.588$ Å was used. The square of the wave function is plotted and each plot is individually normalized to a maximum value of 100.

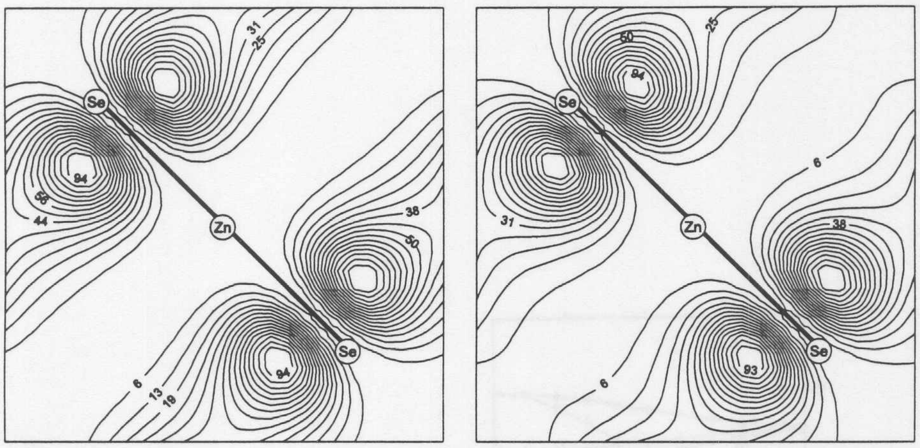

(a) -5 eV at Γ

(b) -2.5 eV half-way $\bar{\Gamma}$-$\bar{\mathrm{J}}'$

Figure 5.29: The charge density plots for the additional surface features. The section is in the surface plane containing the two second-layer Se atoms. The Zn c(2×2) atom is very close to this surface and therefore is also indicated. Each plot is normalized to the maximum value of 100.

bonds. The charge densities are similar but the wave functions must be different since one of the features is flat and the second highly dispersive.

The contour-plots indicate that the electronic structure of the ZnSe(001)-c(2×2) surface has a molecule-like, chain-like character, without significant bonding to the deeper layers. The surface features in the charge density are easily identified as Se p-like bonds which sometimes interact with Zn sp hybrids. The obvious question to ask is what happens when there is no bulk, but just the two last layers of Zn and Se with the c(2×2) structure. The calculations for such an *artificial* structure were performed and the result is shown in Fig. 5.30.

The similarity of the lower bands to the surface structure calculated for the complete slab is striking. The dispersion is the same and there are no additional bands in the neighborhood. The upper part contains some bands very similar to the ones calculated with the complete slab, but they are not so well separated since there are several bands in this region. To check how much the structure is affected by long-range interactions an additional calculation was performed with the same geometrical structure but strained in the $(1\bar{1}0)$ direction such that the chain-to-chain distance was twice as large as in the c(2×2) case. It was found that the

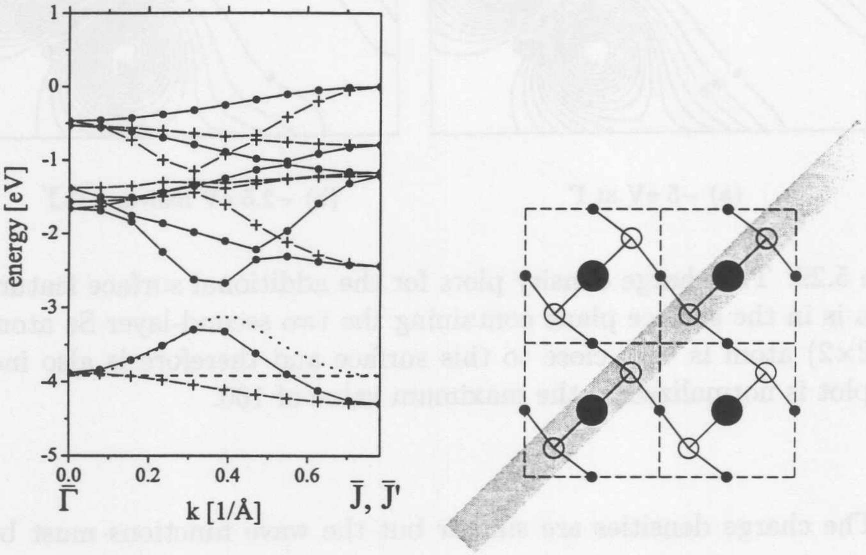

Figure 5.30: The band structure of the *artificial* atomic structure containing one layer of Se with a second c(2×2) reconstructed layer of Zn (• $\bar{\Gamma}$-$\bar{J}'$, + $\bar{\Gamma}$-$\bar{J}$). The atomic positions are the same as for the slab geometry but with the rest of the atoms removed. Additionally the calculations were performed for the Se-Zn-Se chains separated in the (1$\bar{1}$0) direction by twice as much as in the c(2×2) structure and the results for the lower band are indicated with dotted and dashed lines. The bands were shifted so that the zero on the energy scale indicates the top of the last occupied band. The shaded area on the right picture indicates what we call a Se-Zn-Se c(2×2)-*chain*.

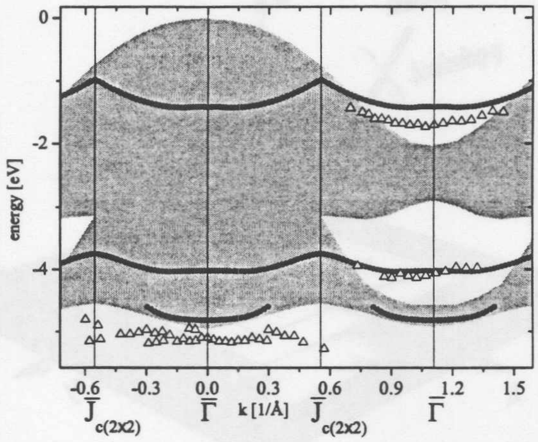

Figure 5.31: The experimental surface electronic structure along $\bar{\Gamma}$-$\bar{\mathrm{J}}_{c(2\times2)}$ direction (△ experimental features, • theoretical bands). The features from Fig. 5.12 are shown but only these identified as surface-related. Shaded areas represent the bulk band structure projected onto (001) surface.

interaction between the adjacent chains disappears (the band along $(1\bar{1}0)$ indicated by the dashed line is flat).

5.3.3 Experimental ZnSe-c(2×2) surface electronic structure - comparison with theory

True surface states are expected in the Γ-$\mathrm{J}_{c(2\times2)}$ direction. Typically *true* surface states are easier to identify than resonances. The results for this direction have already been presented in Figs. 5.10 and 5.12. Here we redraw them in Fig. 5.31 together with the theoretical bands and the projected bulk band structure for the $\bar{\Gamma}$-$\bar{\mathrm{J}}_{c(2\times2)}$ direction. It is not clear whether the experimental features at the bottom of the valence band should be considered as a surface states or resonances, however, they are shown because they could be related to the lowest feature in the calculated band structure. The two remaining features can be identified unambiguously, however, the uppermost feature lies (at the second Γ) around 0.5 eV below the theoretical predictions. A similar shift, but in the opposite direction, was observed on CdTe in the same direction [71]. The dispersion of the experimental feature is very apparent as can be seen in Fig. 5.10 and at this point the theoretical calculation failed to reproduce the value of the eigenstate precisely which is probably due to the

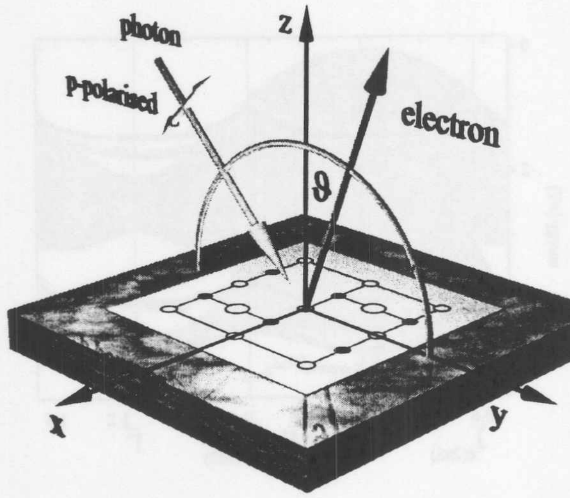

Figure 5.32: The geometry of the angle-resolved photoemission experiment used for surface band structure measurements. Schematic sample orientation for measurement along $\bar{\Gamma}$-$\bar{\mathrm{J}}'$ is shown. The polarization of the incident light is indicated - in this geometry the light is p-polarized [97].

limitation of the LDA approximation[13]. Nevertheless the overall agrement between the experiment and theory for the two upper bands is very good.

The observation of (2×1) reconstruction on ZnSe(001) by LEED indicates that no differently oriented domains are present on the surface. Hence, such situation is expected also for c(2×2) reconstruction. Also from the geometry of zinc-blende crystals it is apparent that only one orientation of the c(2×2)-*chains* is allowed even in the presence of the steps on the surface.

To obtain the experimental band structure for $\bar{\Gamma}$-$\bar{\mathrm{J}}'$ and $\bar{\Gamma}$-$\bar{\mathrm{J}}$ directions we performed additional angle-resolved scans at photon energies $E_{ph} = 25$ and 21.22 eV[14]. The geometry of the angle-resolved experiment is shown in Fig. 5.32. The spectra for $E_{ph} = 21.22$ eV are shown in Fig. 5.33. Several features are apparent, however, in this thesis we especially pay attention to the ones that could be assigned to the theoretical surface bands at -4 and -1.5 eV at Γ. The features that arise from bulk

---

[13] In Ref. [71] Gundel *et al.* show that the many body *GW* approach corrects the energy of this band so it should lie deeper - and agree better with the experiment. Note that comparison of our results to those on CdTe is reasonable since the two systems are very similar.

[14] Actually more scans at different $\hbar\omega$ were performed for the $\bar{\Gamma}$-$\bar{\mathrm{J}}'$, $\bar{\Gamma}$-$\bar{\mathrm{J}}$ and $\bar{\Gamma}$-$\bar{\mathrm{J}}_{c(2\times2)}$ directions. All the results are consistent with the ones shown being most representative. Especially $E_{ph} =$ 21.22 eV was chosen to allow our experiments to be repeated with a HeI resonance line when no synchrotron light is available.

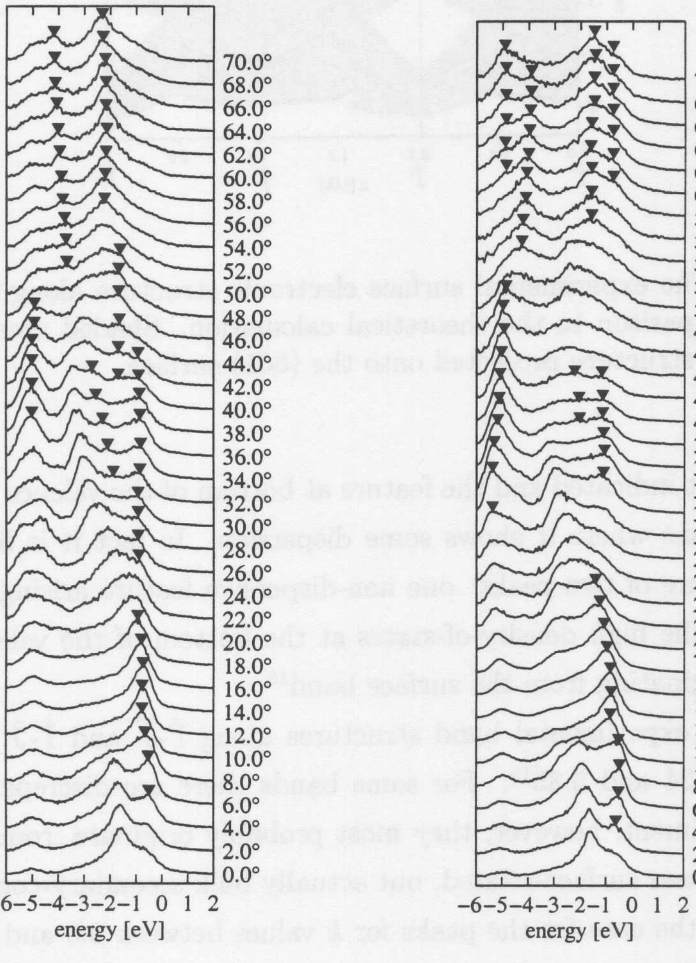

(a) $\bar{\Gamma}$-$\bar{J}'$ (b) $\bar{\Gamma}$-$\bar{J}$

Figure 5.33: The experimental EDCs for the $\bar{\Gamma}$-$\bar{J}$ and $\bar{\Gamma}$-$\bar{J}'$ directions at constant photon energy $E_{ph} = 21.22$ eV using synchrotron radiation. Features identified as possible surface related transitions are indicated.

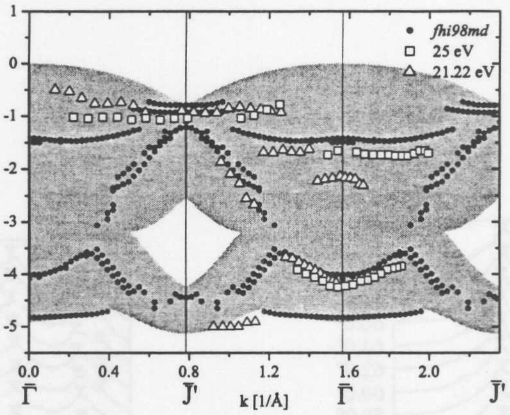

Figure 5.34: The experimental surface electronic structure along the $\bar{\Gamma}$-$\bar{\mathrm{J}}'$ direction in comparison to the theoretical calculation. Shaded areas represent the bulk band structure projected onto the (001) surface.

transitions are not indicated and the feature at bottom of the valence band is partly indicated in regions where it shows some dispersion. In fact it is likely that this feature is a mixture of two peaks: one non-dispersive feature arising from indirect transitions from the high density-of-states at the bottom of the valence band and the other one originating from the surface band[15].

The resulting experimental band structures along $\bar{\Gamma}$-$\bar{\mathrm{J}}'$ and $\bar{\Gamma}$-$\bar{\mathrm{J}}$ directions are shown in Figs. 5.34 and 5.35[16]. For some bands there are discrepancies between theory and experiment, however, they most probably originate from the fact that some features are not surface-related, but actually bulk secondary-cone peaks. This is most probably the case for the peaks for k values between 0.0 and 0.4 $\mathrm{\AA}^{-1}$. The rather dominant feature at large angles around -2.2 eV in the $\bar{\Gamma}$-$\bar{\mathrm{J}}'$ direction is more difficult to explain, however, it may be simply a primary-cone transition, or a mixture of several features. Nevertheless the most important message from the two band structures is that the spectral features are found with good accuracy and in particular the one at -4 eV at Γ is reproduced precisely. Agreement for the higher band is a bit worse, and as in the case of the $\bar{\Gamma}$-$\bar{\mathrm{J}}_{c(2\times2)}$ direction, the theoretical calculation places the band slightly too high.

The deep lying band at $\bar{\mathrm{J}}$ in Fig. 5.35 that was already considered in Subsections

---

[15] The overlap of these features in the spectra makes the assignment difficult.

[16] A similar, although experimental only study was performed by Xue *et al.* [152].

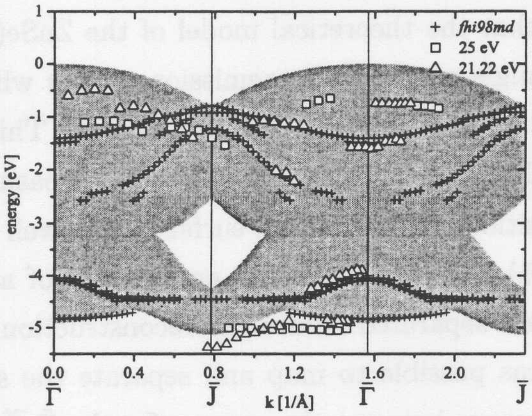

Figure 5.35: The experimental surface electronic structure along the $\bar{\Gamma}$-$\bar{J}$ direction in comparison to the theoretical calculation. Shaded areas represent the bulk band structure projected onto the (001) surface.

5.2.3 and 5.2.4 is most probably related to the surface resonance at the bottom of the valence band. Since such resonance is not predicted by our calculations it may originate from the areas on the sample where the surface Zn coverage is not exactly 50%.

5.4 Conclusions

This work indicates that the theoretical model of the ZnSe(001)-c(2×2) surface is consistent with the angle-resolved photoemission results with some surface bands reproduced to an accuracy of tenths of an electronvolt. This model is also consistent with the latest high-resolution x-ray diffraction measurements [151] and the calculated atomic positions of the relaxed surface agree well with the experimental values. The ZnSe(001)-c(2×2) structure is an example of a system where surface and bulk properties are separated. Since the reconstruction is stable and exhibits long-range order it was possible to map and separate the surface and bulk band structures. The differences between the spectra for the $\bar{\Gamma}$-$\bar{J}'$ and $\bar{\Gamma}$-$\bar{J}$ directions on the ZnSe(001) surface has been demonstrated and this is a new, previously unpublished result.

Chapter 6

Conclusions and Outlook

For both studied materials, gallium nitride and zinc selenide, distinct photoemission features originating from the electronic states located in the surface region were observed.

The angle-resolved photoemission results on GaN revealed the differences between the electronic structures of (0001) and $(000\bar{1})$ surfaces. In case of thin film sample surface features were observed that are not predicted by the present theoretical calculations. The situation for the ZnSe(001)-c(2×2) surface is the opposite - here striking agreement between the experiments and state-of-the-art theory has been achieved.

Regarding GaN the conclusion of this thesis is that there is still a need for additional theoretical calculations. We conclude that in case of $(000\bar{1})$ single crystal samples the surface contains domains with different reconstructions. The (0001) surfaces of thin films have metallic character and the (1×1) LEED patterns observed on these samples may result from the double overlayer termination in a discommensuration-fluid phase proposed by Northrup *et al.* [135].

The most important results of this thesis are these related to ZnSe. This is a good example of a combined theoretical and experimental investigations where excellent agreement has been achieved. The theoretical surface band structure of ZnSe(001)-c(2×2) reconstructed surface has not been previously published so it may serve as a reference for those who would like to verify the presented results e.g. at higher photon energies. The straightforward continuation of the theoretical part would be to calculate the ZnSe(001)-(2×1) surface structure and such a calculation is planned.

The fact that the surface electronic features of the ZnSe(001)-c(2×2) reconstructed surface are located directly in the two uppermost layers and do not interact with the deeper bulk layers is a particulary interesting result. For one of the features the corresponding charge density is very similar to a single Se-Zn-Se molecule. Similar charge densities were found in CdTe [71].

On the experimental side it was shown that the free-electron final state model works relatively well in case of bulk primary-cone transitions. To identify other features comparison to theoretically calculated EDCs is very useful and in the case of the results on ZnSe the dispersions of unassigned bulk features were resolved. The differences observed for the $\bar{\Gamma}$-$\bar{J}$ and $\bar{\Gamma}$-$\bar{J}'$ directions of the c(2×2) reconstructed surface are new and have not been reported for any of the II-IV (001) surfaces.

The primary cone free-electron final state model allows also to map the bulk Γ-L direction on the ZnSe(001) surface. The agreement between the measured and theoretical bulk band structure in this direction is very good. Hence, all the important high-symmetry lines (i.e. Γ-X, Γ-K-X and Γ-L) of the Brillouin zone were mapped using the (001) surface orientation.

In the future close interaction between the theory and experiment will be needed to unravel the complexities of the electronic structure of reduced dimensional and localized atomic systems.

References

[1] S. Nakamura, T. Mukai, and M. Senoh, Appl. Phys. Lett. **64**, 1687 (1994).

[2] I. Grzegory, J. Jun, M. Boćkowski, S. Krukowski, M. Wróblewski, B. Łucznik, and S. Porowski, J. Phys. Chem. Solids **56**, 639 (1995).

[3] Y. Fan, J. Han, L. He, J. Saraie, R. L. Gunshor, M. Hagerott, H. Jeon, V. Nurmikko, G. C. Hua, and N. Otsuka, Appl. Phys. Lett. **61**, 3160 (1992).

[4] R. M. Park, M. B. Troffer, C. M. Rouleau, J. M. DePuydt, and M. A. Haase, Appl. Phys. Lett. **57**, 2127 (1990).

[5] A. Waag, T. Litz, F. Fisher, H.-J. Lugauer, T. Baron, K. Schüll, U. Zehnder, T. Gerhardt, U. Lunz, M. Keim, G. Reuscher, and G. Landwehr, J. Cryst. Growth. **184/185**, 1 (1998).

[6] G. V. Hansson and R. I. G. Uhrberg, Surf. Sci. Rep. **9**, 197 (1988).

[7] J. R. Reitz, Solid. St. Phys. **1**, 1 (1955).

[8] J. M. Ziman, Solid. St. Phys. **26**, 1 (1971).

[9] J. O. Dimmock, Solid St. Phys. **26**, 103 (1971).

[10] M. C. Payne, M. P. Teter, D. C. Allan, T. A. Arias, and J. D. Joannopoulos, Rev. Mod. Phys. **64**, 1045 (1992).

[11] D. R. Hartree, Proc. Camb. Phil. Soc. **24**, 89 (1928).

[12] J. C. Slater, Phys. Rev. **35**, 210 (1930).

[13] V. Fock, Z. Physik **61**, 126 (1930).

[14] J. C. Slater, Phys. Rev. **34**, 1293 (1929).

[15] W. Heiler and F. London, Z. Physik **44**, 455 (1927).

[16] F. Hund, Z. Physik **51**, 759 (1928).

[17] R. S. Mulliken, Phys. Rev. **32**, 186 (1928).

[18] F. Bloch, Z. Physik **52**, 555 (1928).

[19] E. Wigner and F. Seitz, Phys. Rev. **43**, 804 (1933).

[20] E. Wigner and F. Seitz, Phys. Rev. **46**, 509 (1934).

[21] J. C. Slater, Phys. Rev. **45**, 794 (1934).

[22] J. Bardeen, J. Chem. Phys. **6**, 367 (1938).

[23] C. Herring, Phys. Rev. **57**, 1169 (1940).

[24] C. Herring and G. A. Hill, Phys. Rev. **58**, 132 (1940).

[25] J. C. Slater, Phys. Rev. **92**, 603 (1953).

[26] J. Korringa, Physica **13**, 392 (1947).

[27] W. Kohn and N. Rostoker, Phys. Rev. **94**, 1111 (1954).

[28] W. Koch and M. C. Holthausen, *A Chemist's Guide to Density Functional Theory* (Wiley-VCH, Weinheim, 2000).

[29] R. G. Parr and W. Yang, *Density Functional Theory of Atoms and Molecules* (Oxford Univerity Press, New York, 1989).

[30] H. Eschrig, *The Fundamentals of Density Functional Theory* (Teubner, Stuttgart Leipzig, 1996).

[31] R. M. Dreizler and E. K. U. Gross, *Density Functional Theory - An Approach to the Quantum Many-Body Problem* (Springer, Berlin, 1995).

[32] R. O. Jones and O. Gunnarsson, Rev. Mod. Phys. **61**, 689 (1989).

[33] L. H. Thomas, Proc. Camb. Phil. Soc. **23**, 542 (1927).

[34] E. Fermi, Rend. Accad. Lincei **6**, 602 (1927).

[35] P. Hohenbeg and W. Kohn, Phys. Rev. **136**, B864 (1964).

[36] M. Levy, Proc. Natl. Acad. Sci. USA **76**, 6062 (1979).

[37] M. Levy, Phys. Rev. A **26**, 1200 (1982).

[38] W. Kohn and L. J. Sham, Phys. Rev. **140**, A1133 (1965).

[39] O. Gunnarson and B. I. Lundqvist, Phys. Rev. B **13**, 4274 (1976).

[40] J. Harris, Phys. Rev. A **29**, 1648 (1984).

[41] J. Harris and R. O. Jones, J.Phys. F **4**, 1170 (1974).

[42] D. C. Langreth and J. P. Perdew, Phys. Rev. B **15**, 2884 (1977).

[43] A. D. Becke, Phys. Rev. A **38**, 3098 (1988).

[44] D. M. Ceperley and B. J. Alder, Phys. Rev. Lett. **45**, 566 (1980).

[45] S. J. Vosko, L. Wilk, and N. Nusair, Can. J. Phys. **58**, 1200 (1980).

[46] J. P. Perdew and Y. Wang, Phys. Rev. B **45**, 13244 (1992).

[47] J. P. Perdew and A. Zunger, Phys. Rev. B **23**, 5048 (1981).

[48] A. D. Becke, J. Chem. Phys. **84**, 4524 (1986).

[49] J. P. Perdew and Y. Wang, Phys. Rev. B **33**, 8800 (1986).

[50] J.P. Perdew, K. Burke, and M. Ernzerhof, Phys. Rev. Lett. **77**, 3865 (1996).

[51] G. J. Laming, V. Termath, and N. C. Handy, J. Chem. Phys. **99**, 8765 (1993).

[52] J. R. Chelikowsky, J. Phys. D **33**, R33 (2000).

[53] N. Troullier and J. L. Martins, Phys. Rev. B **43**, 1993 (1991).

[54] H. Hellman, J. Chem. Phys. **3**, 61 (1935).

[55] J. C. Philips and L. Kleinman, Phys. Rev. **116**, 287 (1959).

[56] F. Bassani and V. Celli, Nuovo Cimento **11**, 805 (1959).

[57] F. Bassani and G. P. Parravicini, *Electronic States and Optical Transitions in Solids* (Pergamon Press, New York, 1975).

[58] D. R. Hamann, Phys. Rev. B **40**, 2980 (1989).

[59] G. B. Bachelet, D. R. Hamann, and M. Schlüter, Phys. Rev. B **26**, 4199 (1982).

[60] D. R. Hamann, M. Schlüter, and C. Chiang, Phys. Rev. Lett. **43**, 1494 (1979).

[61] H. S. Greenside and M. Schlüter, Phys. Rev. B **28**, 535 (1983).

[62] A. M. Rappe, K. M. Rabe, E. Kaxiras, and J. D. Joannopoulos, Phys. Rev. B **41**, 1227 (1990).

[63] D. Vanderbilt, Phys. Rev. B **41**, 7892 (1990).

[64] G. Kerker, J. Phys. C **13**, L189 (1980).

[65] M. Fuchs and M. Scheffler, Comp. Phys. Comm. **119**, 67 (1999).

[66] L. Kleinmann and D. M. Bylander, Phys. Rev. Lett. **48**, 1425 (1982).

[67] M. Bockstedte, A. Kley, J. Neugebauer, and M. Scheffler, Comp. Phys. Commun. **107**, 187 (1997).

[68] C. Lee, W. Yang, and R. G. Parr, Phys. Rev. B **37**, 785 (1988).

[69] F.-H. Wang, P. Krüger, and J. Pollman, Phys. Rev. B **64**, 035305 (2001).

[70] D. J. Chadi and M. L. Cohen, Phys. Stat. Sol. (b) **68**, 405 (1975).

[71] S. Gundel, A. Fleszar, W. Fashinger, and W. Hanke, Phys. Rev. B **59**, 15261 (1999).

[72] T. Strasser, C. Solterbeck, F. Starrost, and W. Schattke, Phys. Rev. B **60**, 11557 (1999).

[73] C. S. Wang and B. M. Klein, Phys. Rev. B **24**, 3393 (1981).

[74] J. E. Bernard and A. Zunger, Phys. Rev. B **36**, 3199 (1987).

[75] S. B. Zhang, S.-H. Wei, and A. Zunger, Phys. Rev. B **52**, 13975 (1995).

[76] D. Vogel, P. Krüger, and J. Pollman, Phys. Rev. B **55**, 12836 (1997).

[77] S. Gundel, Ph.D. thesis, Würzburg (2001).

[78] M. L. Cohen and J. R. Chelikowsky, *Electronic Structure and Optical Properties of Semiconductors* (Springer-Verlag, New York Berlin Heidelberg, 1996).

[79] R. Hoffman, J.Chem. Phys. **39**, 1397 (1963).

[80] M. Suzuki, T. Uenoyama, and A. Yanase, Phys. Rev. B **52**, 8132 (1995).

[81] H. Dröge, M. Nagelstrasser, J. Nürnberger, W. Fashinger, A. Fleszar, and H.-P. Steinrück, Surf. Sci. **454-456**, 477 (2000).

[82] I. Tamm, Phys. Z. Soviet Union **1**, 733 (1932).

[83] W. Shockley, Phys. Rev. **56**, 317 (1939).

[84] H. Lüth, *Surfaces and Interfaces of Solids* (Springer-Verlag, Berlin Heidelberg, 1993).

[85] S. Nagel, A. Baldereschi, and K. Maschke, J. Phys. C **12**, 1625 (1979).

[86] M. O. D. Camara, A. Mauger, and I. Devos, Phys. Rev. B **65**, 125206 (2002).

[87] C. H. Park and D. J. Chadi, Phys. Rev. B **49**, 16467 (1994).

[88] S. Gundel, Diplomarbeit, Universität Würzburg (1997).

[89] A. Garcia and J. E. Northrup, J. Vac. Sci. Technol. B **12**, 2678 (1994).

[90] F. J. Himpsel, Advances in Physics **32**, 1 (1983).

[91] G. D. Mahan, Phys. Rev. B **2**, 4334 (1970).

[92] W. L. Schaich and N. W. Ashcroft, Phys. Rev. B **3**, 2452 (1971).

[93] P. J. Feibelman and D. E. Eastman, Phys. Rev. B **10**, 4932 (1974).

[94] W. Schattke, Prog. Surf. Sci. **54**, 211 (1997).

[95] N. V. Smith and W. E. Spicer, Phys. Rev. Lett. **23**, 769 (1969).

[96] *Photoemission in Solids*, edited by M. Cardona and L. Ley (Springer-Verlag, Berlin Heidelberg, 1978).

[97] S. Hüfner, *Photoelectron Spectroscopy* (Springer-Verlag, Berlin Heidelberg, 1995).

[98] P. Yu and M. Cardona, *Fundamentals of Semiconductors* (Springer-Verlag, Berlin Heidelberg, 1996).

[99] C. N. Berglund and W. E. Spicer, Phys. Rev. **136**, A1030 (1964).

[100] C. N. Berglund and W. E. Spicer, Phys. Rev. **136**, A1044 (1964).

[101] K.-U. Gawlik, Ph.D. Thesis, Kiel University, Germany *(in German)* (1996).

[102] K. Roßnagel, Ph.D. Thesis, Kiel University, Germany (2001).

[103] J. Henk, W. Schattke, H.-P. Barnscheidt, C. Janowitz, R. Manzke, and M. Skibowski, Phys. Rev. B **39**, 13286 (1989).

[104] J. Henk, W. Schattke, H. Carstensen, R. Manzke, and M. Skibowski, Phys. Rev. B **47**, 2251 (1993).

[105] J. M. Nicholls, G. V. Hansson, U. O. Karlsson, P. E. S. Persson, R. I. G. Uhrberg, R. Engelhardt, S. A. Flodström, and E.-E. Koch, Phys. Rev. Lett. **36**, 376 (1976).

[106] B. S. Itshkawitz, I.-W. Lyo, and E. W. Plummer, Phys. Rev. B **41**, 8075 (1990).

[107] R. D. Bringans, R. I. G. Uhrberg, and R. Z. Bachrach, Phys. Rev. B **34**, 2373 (1986).

[108] T.-C. Chiang, R. Ludeke, M. Aono, G. Landgren, F. J. Himpsel, and D. E. Eastman, Phys. Rev. B **27**, 4770 (1983).

[109] J. F. van der Veen, F. J. Himpsel, and D. E. Eastman, Phys. Rev. B **22**, 4226 (1980).

[110] J. Anderson and G. J. Lapeyre, Phys. Rev. Lett. **36**, 376 (1976).

[111] Y. Q. Cai, R. C. G. Leckey, J. D. Riley, A. P. J. Stampfl, and L. Ley, Phys. Rev. B **53**, 4729 (1996).

[112] J. F. van der Veen, F. J. Himpsel, and D. E. Eastman, Sol. St. Comm. **34**, 33 (1980).

[113] P. Thiry, D. Chandesris, L. Lecante, C. Guillot, P. Pinchaux, and Y. Pétroff, Phys. Rev. Lett. **43**, 82 (1979).

[114] T.-C. Chiang, J. A. Knapp, M. Aono, and D. E. Eastman, Phys. Rev. B **21**, 3513 (1980).

[115] V. N. Strocov and H. I. Starnberg, Phys. Rev. B **52**, 8759 (1995).

[116] V. N. Strocov, H. I. Starnberg, P. O. Nilsson, , and L. J. Holleboom, J. Phys.: Condens. Matter **8**, 7549 (1996).

[117] V. N. Strocov, H. I. Starnberg, P. O. Nilsson, H. E. Brauer, and L. J. Holleboom, Phys. Rev. Lett. **79**, 467 (1997).

[118] M. N. er, H. Dröge, H.-P. Steinrück, F. Fischer, T. Litz, A. Waag, G. Landwehr, A. Fleszar, and W. Hanke, Phys. Rev. B **58**, 10394 (1998).

[119] *Electronic Materials*, edited by J. R. Chelikowsky and A. Franciosi (Springer-Verlag, Berlin Heidelberg, 1991).

[120] R. I. G. Uhrberg, G. V. Hansson, U. O. Carlsson, J. M. Nicholls, P. E. S. Persson, S. A. Flodström, R. Engelhardt, and E.-E. Koch, Phys. Rev. Lett. **52**, 2265 (1984).

[121] M. Morgenstern, J. Wiebe, A. Wachowiak, M. Getzlaff, J. Klijn, L. Plucinski, R. L. Johnson, and R. Wiesendanger, Phys. Rev. B **65**, 155325 (2002).

[122] R. L. Johnson and J. Reichardt, Nucl. Instr. Meth. **208**, 791 (1983).

[123] C. A. Feldmann, R. Engelhardt, T. Permien, E.-E. Koch, and V. Saile, Nucl. Instr. and Meth. **208**, 785 (1983).

[124] H.-J. Kim, Ph.D. Thesis, Hambirg University, Germany (1996).

[125] A. R. Smith, R. M. Feenstra, D. W. Greve, J. Neugebauer, and J. E. Northrup, Phys. Rev. Lett. **79**, 3934 (1997).

[126] L. Plucinski, T. Strasser, B. J. Kowalski, K. Rossnagel, T. Böttcher, S. Einfeldt, D. Hommel, I. Grzegory, S. Porowski, B. A. Orlowski, W. Schattke, and R. L. Johnson, Surf. Sci. **507-510**, 223 (2002).

[127] A. R. Smith, R. M. Feenstra, D. W. Greeve, M. S. Shin, M. Skowronski, J. Neugebauer, and J. E. Northrup, J. Vac. Sci. Technol. B **16(4)**, 2242 (1998).

[128] B. J. Kowalski, L. Plucinski, K. Kopalko, R. J. Iwanowski, B. A. Orlowski, R. L. Johnson, I. Grzegory, and S. Porowski, Surf. Sci. **482-485**, 740 (2001).

[129] S. Figge, T. Böttcher, S. Einfeldt, and D. Hommel, J. of Crystal Growth **221**, 262 (2000).

[130] S. S. Dhesi, C. B. Stagarescu, and K. E. Smith, Phys. Rev. B **56**, 10271 (1997).

[131] Y.-C. Chao, C. B. Stragarescu, J. E. Downes, P. Ryan, and K. E. Smith, Phys. Rev. B **59**, R15586 (1999).

[132] P. Ryan, Y.-C. Chao, J. Downes, C. McGuinnes, K. E. Smith, A. V. Sampath, and T. D. Moustakas, Surf. Sci. **467**, L827 (2000).

[133] T. Valla, P. D. Johnson, S. S. Dhesi, K. E. Smith, D. Douppalapudi, T. D. Moustakas, and E. L. Shirley, Phys. Rev. B **59**, 5003 (1999).

[134] T. Strasser, C. Solterbeck, W. Schattke, I. Bartos, M. Cukr, and P. Jiricek, Phys. Rev. B **63**, 085309 (2001).

[135] J. E. Northrup, J. Neugebauer, R. M. Feenstra, and A. R. Smith, Phys. Rev. B **61**, 9932 (2000).

[136] T. Maruyama, Y. Miyajima, S. H. Cho, K. Akimoto, and H. Kato, Physica B **262**, 240 (1999).

[137] F.-H. Wang, P. Krüger, and J. Pollman, Surf. Sci. **499**, 193 (2002).

[138] B. J. Kowalski, R. J. Iwanowski, J. Sadowski, J. Kanski, I. Grzegory, and S. Porowski, Surf. Sci. **507-510**, 186 (2002).

[139] B. J. Kowalski, , private communication.

[140] W. Weigand, C. Kumpf, M. Sokolowski, A. Bader, C. Schumacher, A. Möginger, W. Faschinger, L. W. Molenkamp, and E. Umbach, Phys. Stat. Sol. (b) **229**, 117 (2002).

[141] W. Chen, A. Kahn, P. Soukiassian, P. S. Magnat, J. Gaines, C. Ponzoni, and D. Olego, Phys. Rev. B **49**, 10790 (1994).

[142] D. W. Niles and H. Höchst, Phys. Rev. B **43**, 1492 (1991).

[143] H. Qu, J. Kanski, P. O. Nilsson, and U. O. Karlsson, Phys. Rev. B **44**, 1762 (1991).

[144] H. Qu, J. Kanski, P. O. Nilsson, and U. O. Karlsson, Phys. Rev. B **43**, 9843 (1991).

[145] D. Olguín and R. Baquero, Phys. Rev. B **50**, 1980 (1994).

[146] D. Olguín and R. Baquero, Phys. Rev. B **51**, 16891 (1995).

[147] H. Qu, P. O. Nilsson, J. Kanski, and L. Ilver, Phys. Rev. B **39**, 3576 (1989).

[148] J. R. Chelikowsky and M. L. Cohen, Phys. Rev. B **14**, 556 (1976).

[149] H. H. Farrell, M. C. Tamargo, S. M. Shibli, and Y. Chang, J. Vac. Sci. Technol. B **8**, 884 (1990).

[150] A. Ohtake, T. Hanada, T. Yasuda, K. Arai, and T. Yao, Phys. Rev. B **60**, 8326 (1999).

[151] W. Weigand, C. Kumpf, A. Müller, O. Bunk, T. Schallenberg, W. Faschinger, L. Molenkamp, R. L. Johnson, and E. Umbach, to be published .

[152] J. Y. Xue, A. P. J. Stampfl, D. Wolfframm, D. A. Evans, M. Hollering, L. Ley, J. D. Riley, and R. C. G. Leckey, Surf. Sci. **401**, L401 (1998).

List of abbreviations

ARPES	angle-resolved photoelectron spectroscopy
BZ	Brillouin zone
DESY	Deutsches Elektronen-Synchrotron
DFT	density functional theory
DFT-LDA	density functional theory with the local density approximation
EDC	energy distribution curve
HASYLAB	Hamburger Synchrotronstralungslabor
HRXRD	high-resolution x-ray diffraction
LEED	low-energy electron diffraction
LDA	local density approximation
PC	personal computer
STM	scanning tunneling microscope
UPS	ultraviolet photoelectron spectroscopy
UHV	ultra-high vacuum
VB	valence band
VBM	valence band maximum
VUV	vacuum ultraviolet
XPS	x-ray photoelectron spectroscopy

Acknowledgements

I would like to thank my supervisor Prof. Robert L. Johnson for his continuous support on the course of the thesis. His extraordinary knowledge about the experimental physics was the most important impulse for me in performing all further investigations.

The fruitful cooperation with Bogdan J. Kowalski from the Institute of Physics in Warsaw was essential for the part of the thesis dedicated to the gallium nitride. I would like to thank him for help and discussions.

I would like to thank Andrzej Fleszar from Würzburg University for introducing me to the density functional theory. Without his help I would never be able to perform calculations presented here.

I would like to thank Christian Kumpf, Wolfgang Weigand and Prof. E. Umbach from the Würzburg University for their support concerning part of this thesis dedicated to the zinc selenide.

Kai Roßnagel from the Kiel University helped me a lot to understand the photoemission process. I would like to thank him for patience in answering to my questions. Thomas Strasser from the Kiel University helped me with understanding the photoemission spectra of gallium nitride.

Jacek Krzywiński from the Institute of Physics in Warsaw brought me to DESY and that started it all. I would like to thank him for supervising my Master's Thesis and giving me the chance to continue my stay at HASYLAB.

Special thanks to Hanno Kretschmann and Prof. G. Huber for supporting me at the Graduiertenkolleg 'Spektroskopie an lokalisierten atomaren Systemen - Felder und lokalisierte Atome - Atome und lokalisierte Felder'.

Jacques Ghijsen and Prof. Bronisław A. Orłowski supported me with their experience in experimental physics.

I would like to thank the whole staff of HASYLAB for their assistance. I am especially indebted to Peter Gürtler.

Additionally I wish to thank Frederic Mirabella, Stefan Gundel (for psuedopotentials), Joachim Wagner, Tim Böttcher, Reinhard Kosuch, Oliver Bunk and all the others that contributed to my work but were unintentionally forgotten.

Thanks to Paweł Korecki and Damian Surdyn (for their friendship) and to my brother.

Finally I wish to give special thanks to my wife Anna and to my parents for their continuous support and encouragement.

This work was supported by the Graduiertenkolleg 'Spektroskopie an lokalisierten atomaren Systemen - Felder und lokalisierte Atome - Atome und lokalisierte Felder' and Bundesministerium für Bildung und Forschung (BMBF project no. 05 KS1 GUC/3).